

IUSS
Scuola Universitaria Superiore Pavia

Politecnico
di Torino

Notional studies for the next generation of space-borne atmospheric radars

A Thesis Submitted in Partial Fulfilment of the Requirements for the Degree of Doctor of Philosophy in

Sustainable Development and Climate Change

Doctoral Programme of National Interest


PhD SDC
SUSTAINABLE DEVELOPMENT
AND CLIMATE CHANGE

In the Curriculum
EARTH SYSTEM AND ENVIRONMENT

by

Filippo Emilio Scarsi

Supervisor: Prof. Alessandro Battaglia

May, 2026

ABSTRACT

Space-borne atmospheric radars play a critical role in advancing our understanding of the Earth's atmosphere and its response to the warming climate by providing global and high-resolution observations of cloud and precipitation systems. Differently from ground-based and airborne systems, space-borne radars offer continuous global coverage and access to remote areas such as oceans and polar regions. Their measurements help to constrain uncertainties in radiative forcing, atmospheric dynamics and microphysics, and enhancing weather forecast capabilities including extreme weather events.

The next generation of space-borne radars is designed to address key gaps in global observations of atmospheric systems and dynamics. Upcoming missions include the NASA INCUS (INvestigation of Convective UpdraftS) and ESA WIVERN (WInd VElocity Radar Nephoscope). INCUS employs a distributed small-satellite constellation of three Ka-band radars operating in synergy to measure temporal changes in radar reflectivity over 30, 90, and 120 seconds intervals, enabling the retrieval of vertical convective mass flux. WIVERN, on the other hand, utilizes a conically scanning W-band Doppler radar with a wide swath, allowing for the observation of three-dimensional distribution of both hydrometeor mass and in-cloud winds across spatial scales from 1 to 1000 km. The simulation of Level-1 products, such as radar reflectivity and Doppler velocity, is a crucial step in mission development and in the design of retrieval algorithms that transform radar measurements into geophysical products, a process that is inherently complex and usually under-constrained. Furthermore, there are some issues specific to space-borne radar observations that further complicate the retrieval and increase the uncertainty in the modeling of the measurements: satellite Doppler-fading, non-uniform beam filling (NUBF), precise knowledge of the pointing, large footprint size, aliasing, and sparse sampling.

The thesis aims at assessing some of the performances, analyzing some of the issues, and trying to reduce some of the uncertainty associated to them. Specifically, in relation to WIVERN, two issues will be discussed: the characterization and correction of the mispointing errors in the Doppler velocity, and the performance on the sampling of atmospheric phenomena with a specific focus on the polar snowfall, which is a useful product for the estimation of the ice sheet mass balance in the Polar regions. For INCUS, the impact of the footprint size, specifically three-dimensional multiple-scattering effects will be addressed. The latter will be discussed also for an EarthCARE-like W-band radar, with results potentially transferable to WIVERN.

Table of Contents

List of Figures

List of Tables

LIST OF ABBREVIATIONS

AMV Atmospheric Motion Vector

AOCS Attitude and Orbit Control Subsystem

AOS Atmosphere Observing System

ARC Active Radar Calibrator

ASI Italian Space Agency

ASTER Advanced Spaceborne Thermal Emission and Reflection Radiometer

BRDF Bidirectional Reflectance Distribution Function

CFAD Contour Frequency Altitude Display

CNESR Centre national d'études spatiales

CPR Cloud Profiling Radar

CSA Canadian Space Agency

DEM Digital Elevation Model

DJF December-January-February

DPR Dual-frequency Precipitation Radar

ECMWF European Centre for Medium-range Weather Forecasts

ERA5 ECMWF Reanalysis v5

ESA European Space Agency

GMI GPM Microwave Imager

GNSS Global Navigation Satellite System

GOS Global Observing System

GPM Global Precipitation Measuring mission

HLoS Horizontal Line of Sight

ICON Icosahedral Nonhydrostatic model

INCUS INvestigation of Convective Updrafts

IPCC Intergovernmental Panel on Climate Change

IWC Ice Water Content

JJA June-July-August

JPL Jet Propulsion Laboratory

LDR Linear Depolarization Ratio

LEO Low Earth Orbit

LiDAR Light Detection and Ranging system

LoS Line of sight

LTAN Local Time of Ascending Node

MCS Mesoscale Convective System

MS Multiple Scattering

MSD Mean Squared Distance

NRMSE Normalised Root Mean Square Error

NUBF Non Uniform Beam Filling

NWP Numerical Weather Prediction

PDPP Polarization Diversity Pulse Pair

PNR Peak-to-Noise Ratio

PSD Particle Size Distribution

PTR Point Target Response

RAMS Regional Atmospheric Modelling System

RC RainCube

RMSE Root Mean Squared Error

RTE Radiative Transfer Equation

SAR Synthethic Aperture Radar

SCR Signal to Clutter Ratio

SNR Signal to Noise Ratio

SS Single Scattering

SWC Snow Water Content

TC Tropical Cyclone

TDTS Time-Dependend Two-Streams

TOA Top Of the Atmosphere

TRMM Tropical Rainfall Measuring Mission

WIVERN Wind Velocity Radar Nephoscope

Chapter 1

Introduction

1 INTRODUCTION

1.1 IMPORTANCE OF UNDERSTANDING CLOUD AND PRECIPITATION PROCESSES

Earth's climate system is governed by the balance between incoming solar radiation and outgoing terrestrial radiation, which defines the global energy budget and constrains large-scale atmospheric circulation and the hydrological cycle. As the planet warms, the hydrological cycle is expected to intensify, resulting in higher atmospheric moisture content, more frequent and intense precipitation extremes, and shifts in the characteristics and spatial organization of precipitating systems (Intergovernmental Panel on Climate Change (IPCC), 2021; Hakuba et al., 2024; Loeb et al., 2024; Deman and Boé, 2025). Improving our understanding of the water cycle, and of the storms that produce most of the world's precipitation, is therefore essential to predict future changes in weather and climate.

Storms come in a wide range of types, defined by how they form, where they occur, and the scale of their extent. For instance, in tropical regions, convective instability is the primary driver of storm development. This instability leads to the formation of individual convective cells, which can merge and evolve into more complex and extensive systems such as Tropical Cyclones (TCs), squall lines, or Mesoscale Convective Systems (MCSs). While convection within individual cells is mainly vertical, the larger structures that emerge from organized convection generate mesoscale horizontal circulations that play a key role in shaping the surrounding atmosphere. Vertical wind shear is also a critical factor, influencing how these convective storms form, evolve, and persist. Storm generated clouds are shaped by storm dynamics and often extend well beyond the immediate regions of active precipitation. These clouds are critical components of the climate system, playing a major role in regulating Earth's energy balance. However, how they respond to a warming climate remains one of the most significant uncertainties in climate projections, as consistently emphasized by Intergovernmental Panel on Climate Change (IPCC) reports. Some clouds, such as high-altitude ice clouds and anvil clouds, develop by storms and are directly affected by storm dynamics. In contrast, shallow cumulus and stratocumulus clouds are generated thanks to the descending branch of large-scale atmospheric circulation, which opposes the upward motion that occurs within storm systems (Vogel, 2011). Clouds and precipitation systems are therefore linked to planetary-scale overturning circulations (Trenberth and Stepaniak, 2003; Hwang and Frierson, 2011; Lionello and et al., 2024; Trenberth, 1991).

Diabatic heating associated with phase changes of water and radiative processes releases or absorbs energy that drives air motion. This process plays a central role in tropical and extra-tropical storm dynamics, as well as in the interaction between storms and larger-scale atmospheric circulations (Wernli and Gray, 2024). However, the repre-

sentation of microphysical processes remains a major source of dynamical uncertainty in weather and climate models, as different microphysics schemes lead to significant variability in cloud structure, precipitation, and feedback responses (Morrison et al., 2020; Seiki et al., 2022; Lamb et al., 2026).

Anvil clouds are cirrus clouds that are formed by deep convective storms in the tropics, where rising air parcels in the convective tower lose their buoyancy and spread out horizontally into the surrounding environment. Their vertical and horizontal extent affect Earth's energy budget through the amount of longwave radiation that they let escape into space (Wall et al., 2018; Sokol et al., 2020). Horizontal extent is observed through geostationary satellite measurements, which unfortunately provide information only on specific and few locations, and therefore, are not representative of the global anvil cloud behavior. Also, these observations do not provide much insight on the vertical extent of anvils, as infrared and visible light cannot penetrate clouds (Gasparini et al., 2019). Significant uncertainty remains also regarding the vertical extent of anvil clouds and how they may evolve in a warming climate (e.g. how it affects the anvil's albedo). A central challenge in assessing this feedback lies in determining whether these clouds will become optically thicker, i.e. reflecting more incoming shortwave radiation and exerting a cooling feedback, or thinner, allowing greater absorption of outgoing long-wave radiation and contributing to warming (Zeng et al., 2024). These outcomes are closely tied to the underlying microphysical and dynamical processes that control the formation, maintenance, and dissipation of anvil clouds. Observational studies have so far reported conflicting results (McKim et al., 2024; Kubar and Waliser, 2019). To reduce this uncertainty, comprehensive and systematic observations are needed, particularly measurements of anvil detrainment height, cloud mass and thickness, and the associated air motions. Such data, collected across a broad spectrum of convective environments, are essential for advancing our understanding of anvil cloud feedback in a changing climate.

In mid-latitudes, snowfall is the primary mechanism for precipitation formation (Mülmenstädt et al., 2015), while in high-latitude and mountainous regions, it is often the dominant form of precipitation reaching the surface (Field and Heymsfield, 2015). Snowfall plays a critical role in the climate system: it contributes to increasing the mass to glaciers and ice sheets, making it vital to cryospheric environments (Souverijns et al., 2018a; Davison et al., 2023; Bailey and Hubbard, 2025), and influences sea ice persistence by insulating it from the atmosphere (Perovich et al., 2017). On land, snow alters surface albedo, reducing planet's warming (Hall, 2004). It also affects ecosystems (Slatyer et al., 2022), transportation (Strong et al., 2010), recreation (Steiger et al., 2019), and freshwater availability for hydropower (Wasti et al., 2022). Accurate measurements of snowfall, particularly in Greenland and Antarctica, are essential, as uncertainty in their precipitation patterns drives much of the ambiguity in sea level rise projections. Although snowfall and extreme events are projected to increase in a warming climate (Quante et al., 2021), large uncertainties remain (Lopez-Cantu et al., 2020; Fiddes et al., 2022) due to limited understanding of the microphysical processes involved in snow formation (Morrison et al., 2012; Griesche et al., 2021). In situ snowfall measurements are highly uncertain due to measurement challenges and strong spatial variability, and are scarce in remote polar regions (Souverijns et al., 2018b; Li et al., 2021). Ground-based radars are mostly limited to populated areas, making space-borne observations essential for global snowfall monitoring. Passive microwave sensors offer broad coverage but struggle to separate snowfall signals from surface effects and supercooled liquid water (Kidd et al., 2021; Battaglia et al., 2020). In contrast, radar instruments like those on CloudSat and EarthCARE provide valuable

vertical profiles of snowfall and better surface discrimination, despite uncertainties in converting radar data to snowfall rates (Stephens et al., 2018; Milani and Kidd, 2023). CloudSat data have been validated against ground observations, enabling snowfall climatologies and studies in data-sparse regions such as Antarctica and Greenland (Mroz et al., 2021; Bennartz et al., 2019; Kulie et al., 2020). However, its 16-day revisit and kilometer-scale footprint limit spatial sampling and introduce noise even in long-term averages.

Key scientific challenges in understanding storm structure involve improving atmospheric models and accurately representing the diversity of storm types across the different Earth climates.

Despite decades of research, our understanding of storm structure and the physical mechanisms behind their evolution, and accurately quantifying the anvil cloud area feedback, remains challenging due to the limited recorded observation. Although climate models can offer longer-term perspectives, they rely on parametrization of the processes involved in cloud formation, making their estimates also uncertain given biases associated with the representation of convection. Furthermore, many of the regional effects of global warming came as a surprise (Shaw et al., 2024; Shaw and Stevens, 2025; Simpson et al., 2025), suggesting that the ability to anticipate future changes in regional precipitation patterns or extremes remains limited. Simply measuring precipitation amounts or cloud radiative properties is not, on its own, sufficient to predict future changes. A physical understanding of the underlying processes is essential. The aspects of climate change, in which the highest confidence exists, are those supported by robust physical explanations. Therefore, improving our understanding of storms, clouds, and precipitation is strongly linked to enhancing our ability to assess and project their climatic impacts. Furthermore, a deep understanding of storm processes is essential for improving forecasts and anticipating the behavior of high-impact weather events (Rodwell et al., 2013). This knowledge also carries our ability to assess the role of storms in the climate system and to predict how storm characteristics might evolve in a warming climate.

1.2 STATUS OF THE GLOBAL OBSERVING SYSTEM

In-cloud winds, water content profiles, vertical mass flux are key to understanding cloud and storm processes and the coupling between water, heat, and atmospheric circulation, yet they remain one of the major gaps in the Global Observing System (GOS).

Satellite missions like Tropical Rainfall Measuring Mission (TRMM) and GPM have offered global observations of vertical diabatic heating profiles (Tao et al., 2016), but they do not provide data on the associated atmospheric circulations. This gap limits a comprehensive understanding of the coupling between water, heat, and circulation across different storm types and spatial scales.

Currently, detailed observations of storm dynamics, such as in-cloud winds, vertical condensate motions, or internal circulation, are mainly available from targeted field campaigns, which are invaluable but limited in space and time. Satellite missions provide broader coverage but primarily measure precipitation and hydrometeor distributions, lacking the capability to capture convective mass flux or the full three-dimensional wind field inside storms, both crucial for understanding development, intensification, and motion.

Although current GOS instruments provide insightful observations of our planet and atmosphere, some of the keys scientific questions, such as:

- Understand what is the role of internal storm dynamics, including winds and mass fluxes, in governing the development, intensification, and propagation of different storm types.

- Understand how the mesoscale circulations influence the development of larger scale dynamics.

- Explore the relationship between convective mass flux and the size and thickness of anvil clouds in tropical storms, focusing on the key mechanisms that govern their formation and lifespan.

- Explore how better quantification of polar snowfall processes can decrease uncertainties in snowfall accumulation and surface mass balance, while improving the modeling of snow-related processes in climate and weather prediction systems.

remain unexplored. Next generation space-borne atmospheric radars aims at providing new observations of the atmosphere and weather systems by adopting new strategies and new types of instruments for filling some of the gaps in our knowledge of our atmospheric and climate system.

This section reviews the GOS for atmospheric and weather observation, highlighting its significant under-representation as a crucial observational component.

1.2.1 Wind observing system

Radiosondes: Launched from fixed ground stations, radiosondes deliver highly accurate vertical profiles of temperature, humidity, and winds, reaching the lower stratosphere. However, global coverage is sparse, especially over oceans and in the tropics, and launches typically occur just twice per day.

Operational Networks of Ground-based Radars: Operational ground-based radars provide high temporal resolution observations, often updated every few minutes. However, they are mainly land-based and have limited vertical resolution. They typically operate in the S, C and X -bands. Non-precipitating clouds are typically not detected. Hydrometeors are treated as tracer for winds, and the Doppler shift produced by them is used to infer wind velocity.

Airborne Systems: Commercial aircraft collect large volumes of horizontal wind data, especially during take-off and landing near airports. Outside these zones, data are limited to cruising altitudes along flight paths. Aircraft generally avoid storms for safety reasons. Airborne radar campaigns offer valuable Doppler and reflectivity data, but they can observe only a limited number of storms and cannot fly directly above storm cores.

Geostationary satellites: Because of their altitude, they typically carry instruments working in the infrared of visible part of the spectrum for keeping spatial not too coarse. They provide useful observation of temporal evolution of systems. However, they can only see the cloud tops and cannot penetrate inside the systems.

Atmospheric Motion Vectors (AMVs): AMVs are derived by tracking cloud or moisture features in visible and infrared satellite imagery. They offer near, global coverage with high temporal frequency. However, the retrieved wind represents a single vertical level, the estimated altitude of the tracked feature, which introduces considerable uncertainty in height assignment (Salonen et al., 2015).

Satellite Active and Passive Microwave Observations: They provide ocean surface wind vectors with dense global coverage. Scatterometers are complemented by synthetic aperture radar Synthethic Aperture Radars (SARs) and passive microwave radiometry. GNSS reflectometry, explored by missions like NASA's CYclone Global Navigation Satellite System (GNSS) (CYGNSS) and European Space Agency (ESA)'s HydroGNSS, is a promising technique. However, none of these systems can provide vertical wind and mass fluxes profiles.

Light Detection and Ranging systems (LiDARs) with Doppler capabilities: active sensors that work by emitting laser pulses. Due to their larger operating frequency, they suffer more attenuation than radars, and they cannot penetrate thick clouds, but can sense smaller particles. Therefore, they are employed to observe thin clouds, aerosols and gases, and are used to measure clear sky winds. They can be ground-based, airborne or space-borne. They are frequently used in synergy with radars as the two measurements are complementary. ESA's Aeolus mission (2018–2023) (Reitebuch, 2012) was the first to provide near-global profiles of Horizontal Line of Sight (HLoS) winds from space, using an off-nadir Doppler wind LiDAR. Aeolus had one of the highest positive impacts on weather forecasts of any single satellite instrument (Rennie et al., 2021). Building on its success, ESA and EUMETSAT are developing Aeolus-2, planned to be launched in 2034. However, like its predecessor, Aeolus-2 will only observe clear skies, optically thin clouds, and the tops of optically thick clouds, due to the fixed off-nadir LiDAR geometry.

1.2.2 Cloud and Precipitation observing system

Atmospheric radars are widely used to observe clouds and precipitation systems, while lidar is particularly effective for detecting thin clouds. Doppler-capable atmospheric radars measure the radial velocity of hydrometeors (e.g., raindrops, cloud droplets, snowflakes, and hailstones). These particles are treated as tracers of airflow, allowing the radial component of the wind velocity to be inferred from their motion. They can be deployed on ground-based, airborne, or space-borne platforms. Passive microwave sensors can also be employed to retrieve thermodynamical and microphysical properties of atmospheric systems by measuring the radiation that is naturally emitted and scattered by the atmosphere and the surface.

Space-borne radars constitute a critical component of the GOS, providing near-global observations of precipitation and cloud systems. Their ability to penetrate clouds and precipitation and resolve internal vertical structure and dynamics has revolutionized our understanding of cloud and storm processes (e.g., CloudSat Cloud Profiling Radar (CPR); GPM Dual-frequency Precipitation Radar (DPR); EarthCARE CPR) and enabled synergistic datasets that improve characterization of cloud microphysics and hydrometeor vertical profiles across the globe. Some of past and currently operating missions employing these instruments are described in this subsection.

Operating in the Ka and Ku -bands, precipitation radars provide good coverage of vertical profile of radar observables and hydrometeor water content. They are less sensitive to small particles than cloud radars, but their signal can penetrate more in depth in optically thick media. Some of the current and past missions that employ these instruments are (Battaglia et al., 2020):

- **TRMM:** Launched in November 1997 as a collaboration between NASA and the Japan Aerospace Exploration Agency (JAXA), the TRMM carried the first spaceborne weather radar (Okamoto, 2003). TRMM operated successfully until 2015 and carried the Precipitation Radar (PR), passive microwave sensors, and visible, infrared, and lightning sensors (Simpson et al., 1996; Kummerow et al., 1998). The PR delivered the first three-dimensional views of weather systems in remote regions, covering a 220 km cross-track swath. Over its 17-year mission, TRMM produced a near-continuous dataset of precipitation observations across tropical and subtropical regions, extending between ±37° latitude. Its primary goal was to provide high-resolution precipitation data to support climate research. Although the PR operated at a single frequency (13.8 GHz), lacked Doppler and dual-polarimetric capabilities, and had a sensitivity threshold of about 17 dBZ, it offered valuable global observations of vertical diabatic heating profiles (Tao et al., 2016). However, its inability to observe the associated atmospheric circulations limits our ability to fully understand how water, heat, and circulation interact across different storm types and spatial scales.

- **GPM:** NASA/JAXA's GPM (Skofronick-Jackson et al., 2017) is the successor to TRMM . It includes the GPM Microwave Imager (GMI), which adds five frequencies to TRMM's radiometer, and the DPR, operating in Ku (13.6 GHz) and Ka (35.5 GHz) bands. With a minimum detection threshold of 14 dBZ (Toyoshima et al., 2015), GPM provides improved precipitation estimates and insights into microphysics thanks to its multi-frequency capabilities. The extended coverage to ±65° latitude enables observations of extra-tropical systems and snowfall. Still, GPM shares the same limitations as TRMM: lack of Doppler or wind retrievals and limited sensitivity to light precipitation.

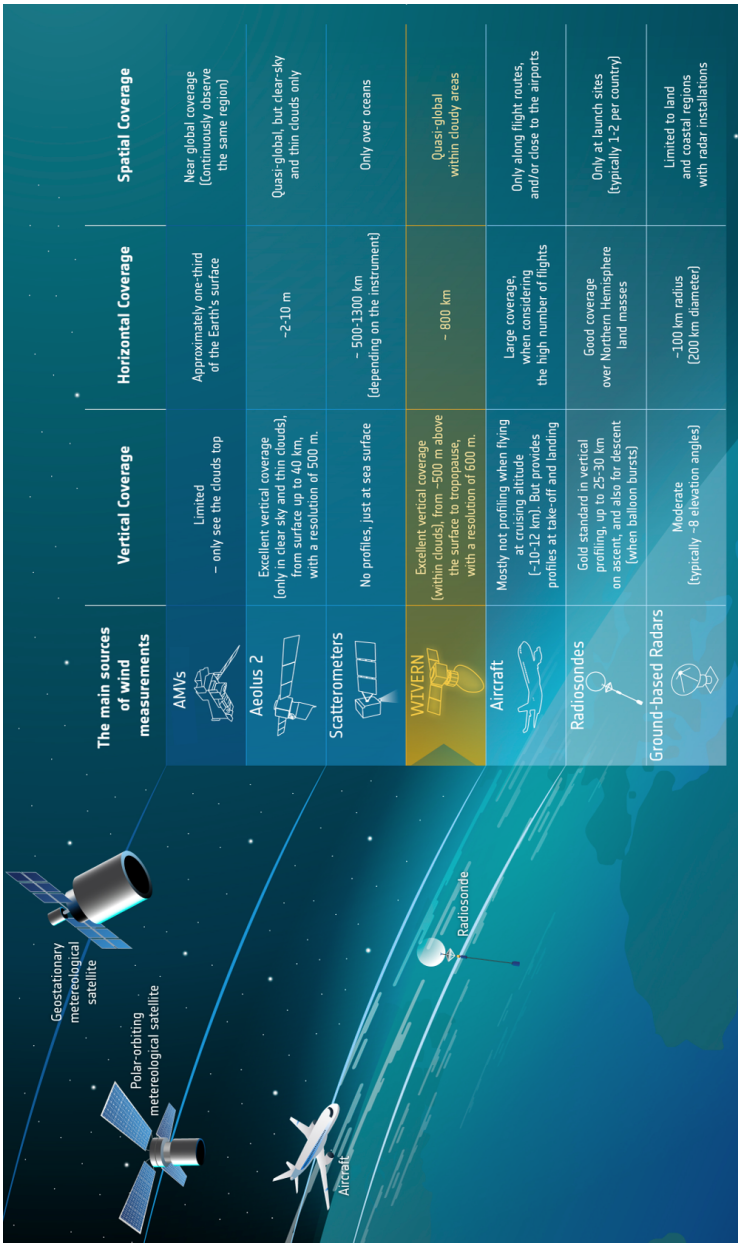

Fig. 1.2.1: *A summary of the status of the global wind observing system. Extracted from European Space Agency (ESA) (2025).*

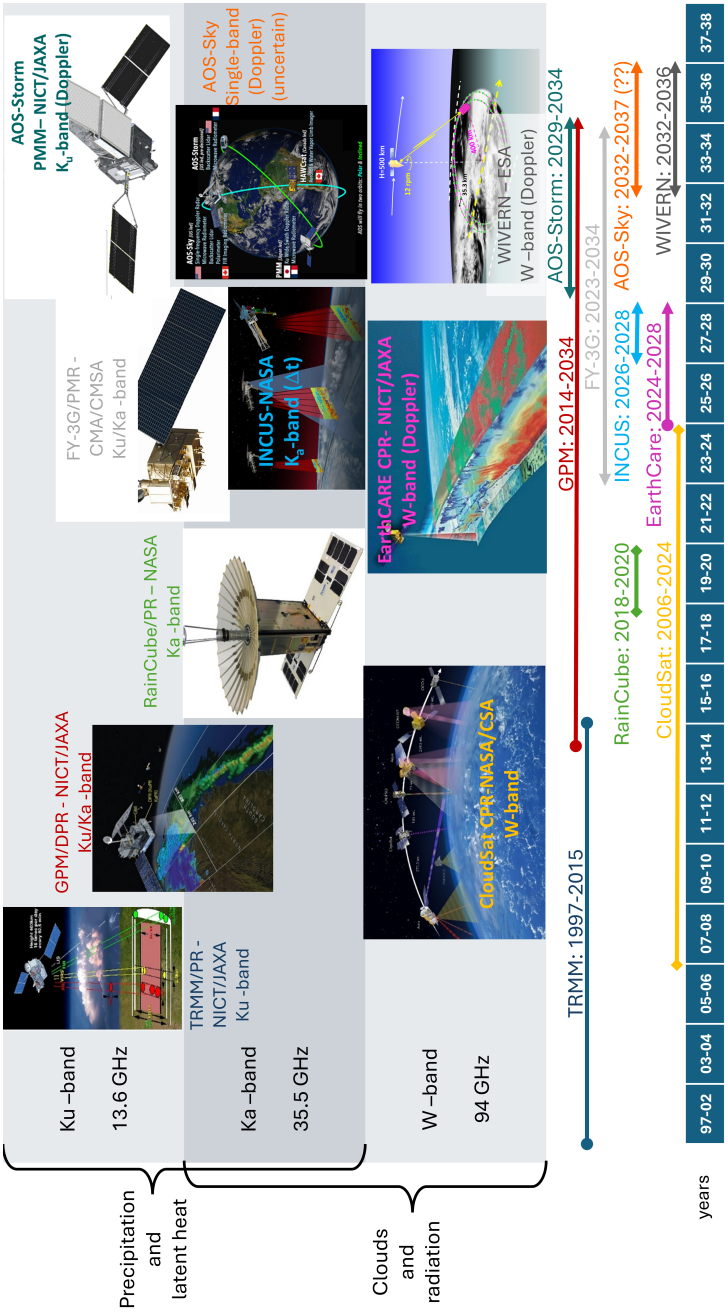

Fig. 1.2.2: *Mission timelines for past, present and future atmospheric radar missions with the relevance of their radar operating bands to the detection of clouds and precipitation (extracted from Battaglia et al. (2020) and modified).*

- **RainCube:** RainCube (RC) has been developed at NASA's Jet Propulsion Laboratory (JPL) with the aim of being able to launch constellations of precipitation radars to observe temporal evolution of convective systems (Peral et al., 2018,

2019). In fact, it is a very small Ka-band radar compatible with 6U CubeSats. The small size translates in small costs, opening the possibilities of launching constellations of them. However the small size means also lower power output, which translates in slightly worse sensitivity than traditional Ka-band radars.

W-band radars are more sensitive to small particles than Ka and Ku -band radars are, but have poorer penetration capabilities. A comparison of how three different frequencies (Ku-, Ka-, and W-band) see the same convective system from space is shown in Fig. 1.2.3 (Chase et al., 2025). Some of the current operating and past missions that employ these instruments are (Battaglia et al., 2020):

- **CloudSat:** Launched in 2006 (and dismissed in 2024) by NASA and the Canadian Space Agency, CloudSat carried the first satellite-based W-band (94 GHz) CPR (Tanelli et al., 2008) as part of NASA's A-Train constellation (Stephens et al., 2008). While originally designed to improve estimates of radiative heating by mapping cloud boundaries, CloudSat also detects a range of precipitation types, from drizzle and snow to moderate rain. It has provided valuable data on Earth's energy budget and water cycle. Since 2018, CloudSat has operated alongside CALIPSO in the C-Train configuration.
- **EarthCARE:** Launched in 2024, ESA's EarthCARE mission (Wehr et al., 2023; Kollias et al., 2023; European Space Agency (ESA), 2024) features a 94 GHz Doppler CPR with high sensitivity and sub-kilometre resolution. However, observations are confined to a narrow vertical curtain under the satellite's path (less than 1 km wide). While it can occasionally capture vertical velocities within convective updrafts, the data are insufficient to fully resolve mesoscale storm circulations or quantify intense vertical motions. EarthCARE also lacks the ability to measure horizontal winds.

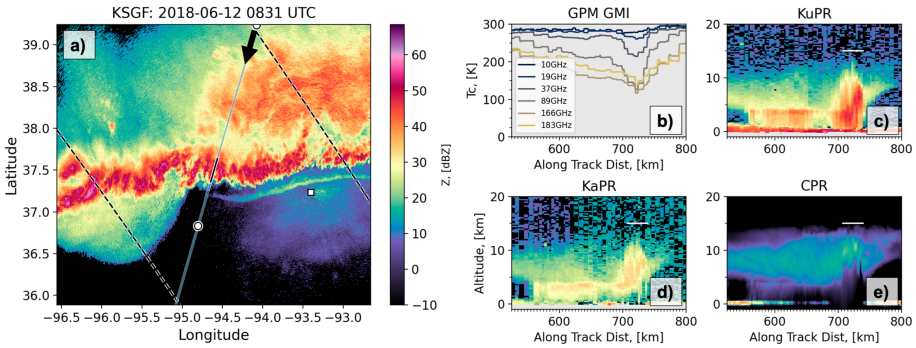

Fig. 1.2.3: *A coincidence between GPM and CloudSat observations for a convective event exemplifying the view of convection from the three space-borne wavelengths: Ku- (panel c), Ka- (panel d), and W-band (panel e). Figure extracted from Chase et al. (2025).*

1.3 THE NEXT GENERATION OF SPACE-BORNE ATMOSPHERIC RADAR MISSIONS

GOS observations of atmospheric systems and winds are still sparse and unevenly distributed, especially in convective and cloudy regions, therefore it is of primary importance to fill the observational gaps.

The next generation of space-borne radars aims at filling some of these gaps to improve our understanding of atmosphere dynamics and Earth's climate, with specific focus on measuring convective mass fluxes and in-cloud winds.

Atmospheric Observing System (Atmosphere Observing System (AOS))

NASA's AOS program will comprise multiple synergistic missions designed to investigate the formation of intense precipitation and clouds, as well as the role of aerosol interactions in these processes. Different types of aerosols influence cloud and precipitation formation in distinct ways. This is achieved by using a combination of sensors on spacecraft, aircraft, balloons and ground stations. AOS will continually observe aerosols, precipitation, clouds and the air-motion within clouds. The architecture consists in several satellites distributed in two different orbit. The following satellites will be on the 55° inclined orbit:

- **AOS-Storm**: U.S. led mission in partnership with Centre national d'études spatiales (CNESR), which will provide the multichannel (89, 183, 325 GHz) radiometers.
- **PMM**: Japan led mission carrying Ku-band wide-swath Doppler radar, and the CNES multichannel radiometers.

The following satellites will be on the polar sun-synchronous orbit with a Local Time of Ascending Node (LTAN) of 01:30 :

- **AOS-Sky**: U.S. led mission in partnership with Canadian Space Agency (CSA). The satellite will have passive capabilities carrying a microwave radiometer, a polarimeter and an imaging radiometer.
- **LUCE**: Itay led mission that will carry an Italian Space Agency (ASI) built 8-channel LiDAR for aerosol and ocean measurements.
- **AOS-Cloud**: NASA led cloud radar profiling mission still in definition phase.

WIVERN (WInd VElocity Radar Nephoscope)

WIVERN is the ESA's Earth Explorer 11 mission (launch planned to be in 2034) (Illingworth et al., 2018, 2020; Tridon et al., 2023; Battaglia et al., 2022, 2025, 2026; European Space Agency (ESA), 2025), selected with the aim of providing new insights in horizontal and vertical in-cloud winds structures. These observations will enhance short and medium-range weather forecasts and increase lead times for high-impact events such as tropical cyclones by assimilating global Doppler data, radar reflectivity profiles, and kilometer-scale 94 GHz brightness temperatures into Numerical Weather Prediction (NWP) models. Among other things WIVERN observations are expected to provide important insights in convective anvil clouds and polar snowfall. The first is essential for understanding cloud–radiation feedback, while the latter is crucial for high-latitude water budgets and the coupling between the atmosphere and the cryosphere.

The satellite will operate in sun-synchronous orbit and will carry a 94 GHz a fast rotating conically scanning Doppler radar with polarization capabilities. The instrument can also work in radiometer mode, helping in observing e.g. the presence of supercooled liquid droplets (instrument and orbital specs are listed in Tab 1.3.1).

A key advantage of this radar concept over its W-band, nadir-pointing predecessors (e.g. NASA's CloudSat and ESA's EarthCARE CPRs) is its wide swath width ($\approx$

800 km), which allows for significantly improved sampling of the vertical structure of clouds and precipitation, as well as their mesoscale and synoptic-scale organization. The improved sampling capabilities will reduce climatological regional uncertainty in precipitation, winds, and cloud retrievals to levels below natural variability on much shorter timescales. The large incidence angle will improve the precipitation detection near the oceanic surfaces thanks to the weaker surface clutter.

In contrast, it is expected that the radar will suffer from increased attenuation due to the slant path, MS effects in the presence of heavy rain and large amounts of ice contents, and a reduction of WIVERN radar sensitivity compared to W-band non-scanning radars that will worsen its cloud detection capabilities.

Table 1.3.1: *Specifics of the WIVERN radar. The configuration here adopted is the one currently under Phase-A study for the ESA Earth Explorer 11 program.*

Mean satellite altitude, H_{SC}	500 km
Mean satellite velocity at ground, v_{SC}	7600 m s^{-1}
Orbit inclination, i	97.42°
Orbit local time of the ascending node, LTAN	06:00
Orbit repeat cycle	5 days
Off-nadir pointing angle, θ_{o-n}	38°
Incidence angle, θ_i	41.6°
Swath width at ground	800 km
RF output frequency	94.05 GHz
Radiometer channel	94.05 GHz
Transmitted power, P_t	2 kW
Pulse duration, τ_p	3.3 μs
Antenna beamwidth, θ_{3dB}	1200 μrad
Circular antenna diameter	3 m
Antenna rotation rate, Ω_a	12 rpm
Footprint speed	500 km s^{-1}
Transmit polarization	H or V
Cross-polar isolation	<-25 dB
Single pulse sensitivity	-15 dBZ
H-V Pair Repetition Frequency	4 kHz
Range sampling distance (rate)	100 m (1.5 MHz)
Number of H-V Pairs per 1 km integration length	8

INCUS (INvestigation of Convective UpdraftS)

INCUS (van den Heever et al., 2022) (launched expected in 2026), is an upcoming NASA mission designed to investigate how tropical convective systems forms and evolve, how they affect the vertical transport of condensed water mass, and how they affect the anvil clouds formation. The mission adopts a distributed satellite approach where three RainCube-like miniaturized Ka-band radar will be carried by three SmallSats flying in close formation in a tropical orbit and working in synergy to measure the time evolution of storms and radar reflectivity within $\Delta t = 30$, 90 and 120 seconds time frame. A time differentiating approach, in synergy with machine learning based algorithm, is used to derive profiles of vertical velocity and vertical mass flux from

pairs of radar reflectivity profiles sampled at two different times.
The satellite in the middle will also carry a TEMPEST-D -like multi-frequency radiometer (Radhakrishnan et al., 2023) with the aim of characterizing the anvil clouds generated by the storms. The mission follows the heritage of RainCube, where the radars have been made larger to improve some performance, such as the single-pulse sensitivity. The antenna size is 1.6 m, resulting in a 3 km radar footprint.

1.4 SCIENTIFIC SCOPE AND STRUCTURE OF THE THESIS

Understanding clouds, precipitation systems, and storm dynamics is essential to improve weather prediction, climate projections, and our representation of atmospheric water and energy cycles. Despite significant advances in satellite observations, key uncertainties remain in the vertical and horizontal structure, dynamics, and microphysical properties of precipitating systems, particularly at the global scale.

Space-borne radars provide a unique capability to probe the internal structure and dynamics of clouds and precipitation systems, complementing passive observations. However, current radar missions are limited in their ability to capture key dynamical quantities such as vertical motion, three-dimensional structure, and rapidly evolving convective processes. Next-generation radar missions, such as WIVERN and INCUS, are specifically designed to address these limitations through new measurement concepts and observing strategies.

Space-borne radar measurements are affected by several technical and physical challenges, particularly in the case of Doppler radars, which have only recently become operational in space (with EarthCARE representing the first such mission, launched in May 2024), and at higher operating frequencies, where attenuation, multiple scattering, and microphysical sensitivities become more pronounced.

1.4.1 Dissertation objective

This thesis focuses on a set of key scientific and technical challenges and issues associated with next-generation space-borne atmospheric radar observations. It pays particular attention to the WIVERN and INCUS missions, which are used as case studies to analyze instrument concepts, retrieval approaches and observational challenges.
The thesis is then structured as follows:

- An overview of key radar quantities and a description of critical aspects of space-borne radars is presented in Chapter 2.
- An in-depth analysis of the characterization and correction of mispointing errors in the Doppler velocity measured by the WIVERN is described in Chapter 3.
- An assessment of the performance of the sampling of precipitations using a WIVERN-like conically scanning system, with a specific focus on the polar snowfall, is discussed in Chapter 4.
- The forward modelling of three-dimensional MS effects in reflectivity profiles are described in Chapter 5 with a focus on INCUS and EarthCARE. Time-Dependend Two-Streams (TDTS) approximation is also compared to the full three-dimensional computations to assess its applicability in convective systems, known to have a strong spatial variability.
- Summary and conclusions are discussed in Chapter 6.

REFERENCES

Bailey, H. and Hubbard, A.: Snow Mass Recharge of the Greenland Ice Sheet Fueled by Intense Atmospheric River, Geophysical Research Letters, 52, e2024GL110 121, https://doi.org/10/g9hjmb, 2025.

Battaglia, A., Kollias, P., Dhillon, R., Roy, R., Tanelli, S., Lamer, K., Grecu, M., Lebsock, M., Watters, D., Mroz, K., Heymsfield, G., Li, L., and Furukawa, K.: Spaceborne Cloud and Precipitation Radars: Status, Challenges, and Ways Forward, Reviews of Geophysics, 58, e2019RG000 686, https://doi.org/10.1029/2019RG000686, e2019RG000686 10.1029/2019RG000686, 2020.

Battaglia, A., Martire, P., Caubet, E., Phalippou, L., Stesina, F., Kollias, P., and Illingworth, A.: Observation error analysis for the WInd VElocity Radar Nephoscope W-band Doppler conically scanning spaceborne radar via end-to-end simulations, Atmospheric Measurement Techniques, 15, 3011–3030, https://doi.org/10.5194/amt-15-3011-2022, 2022.

Battaglia, A., Rizik, A., Sikaneta, I., and Tridon, F.: I and Qs Simulation and Processing Envisaged for Spaceborne Polarization Diversity Doppler Radars, IEEE Transactions on Geoscience and Remote Sensing, 63, 1–14, https://doi.org/10.1109/TGRS.2025.3529672, 2025.

Battaglia, A., Manconi, F., Recupero, M., Cambiotti, C., Coppola, M., Parodi, A., Tridon, F., Mantovani, S., Kollias, P., Nolan, D. S., Kleinherenbrink, M., and Pourshamsi, M.: Peering Inside Tropical Cyclones With the WIVERN Space-Borne Doppler Radar, Earth and Space Science, 13, e2025EA004 680, https://doi.org/https://doi.org/10.1029/2025EA004680, e2025EA004680 2025EA004680, 2026.

Bennartz, R., Fell, F., Pettersen, C., Shupe, M. D., and Schuettemeyer, D.: Spatial and temporal variability of snowfall over Greenland from CloudSat observations, Atmospheric Chemistry and Physics, 19, 8101–8121, https://doi.org/10.5194/acp-19-8101-2019, 2019.

Chase, R. J., Dolan, B., Rasmussen, K. L., Schulte, R. M., Stephens, G., Turk, F. J., and van den Heever, S. C.: A Multifrequency Spaceborne Radar Perspective of Deep Convection, Journal of Applied Meteorology and Climatology, 64, 133 – 145, https://doi.org/10.1175/JAMC-D-24-0109.1, 2025.

Davison, B. J., Hogg, A. E., Rigby, R., Veldhuijsen, S., van Wessem, J. M., van den Broeke, M. R., Holland, P. R., Selley, H. L., and Dutrieux, P.: Sea Level Rise from West Antarctic Mass Loss Significantly Modified by Large Snowfall Anomalies, Nature Communications, 14, 1479, https://doi.org/10/grx8rc, 2023.

Deman, J. and Boé, J.: Future changes in runoff over western and central Europe: disentangling the hydrological behavior of CMIP6 models, Earth System Dynamics, 16, 1409–1426, https://doi.org/10.5194/esd-16-1409-2025, 2025.

European Space Agency (ESA): EarthCARE Cloud Profiling Radar instrument overview, https://www.esa.int/Applications/Observing_the_Earth/FutureEO/EarthCARE/EarthCARE_s_cloud_profiling_radar, 2024.

European Space Agency (ESA): Report for Mission Selection: Earth Explorer 11 Candidate Mission WIVERN, Tech. Rep. ESA-EOPSM-WIVE-RP-4798, European Space Agency, Noordwijk, The Netherlands, https://doi.org/10.5281/zenodo.15607041, 2025.

Fiddes, S. L., Protat, A., Mallet, M. D., Alexander, S. P., and Woodhouse, M. T.: Southern Ocean Cloud and Shortwave Radiation Biases in a Nudged Climate Model Simulation: Does the Model Ever Get It Right?, Atmospheric Chemistry and Physics, 22, 14 603–14 630, https://doi.org/10/g9fh28, 2022.

Field, P. R. and Heymsfield, A. J.: Importance of snow to global precipitation, Geophysical Research Letters, 42, 9512–9520, https://doi.org/10.1002/2015GL065497, 2015.

Gasparini, B., Wang, C., and L'Ecuyer, T. S.: What Drives the Life Cycle of Tropical Anvil Clouds?, Journal of Advances in Modeling Earth Systems, 11, 4039–4060, https://doi.org/10.1029/2019MS001736, 2019.

Griesche, H. J., Ohneiser, K., Seifert, P., Radenz, M., Engelmann, R., and Ansmann, A.: Contrasting ice formation in Arctic clouds: surface-coupled vs. surface-decoupled clouds, Atmospheric Chemistry and Physics, 21, 10 357–10 374, https://doi.org/10.5194/acp-21-10357-2021, 2021.

Hakuba, M. Z., Fourest, S., Boyer, T., and et al.: Trends and Variability in Earth's Energy Imbalance and Ocean Heat Uptake Since 2005, Surveys in Geophysics, 45, 1721–1756, https://doi.org/10.1007/s10712-024-09849-5, 2024.

Hall, A.: The Role of Surface Albedo Feedback in Climate, Journal of Climate, 17, 1550 – 1568, https://doi.org/10.1175/1520-0442(2004)017<1550:TROSAF>2.0.CO;2, 2004.

Hwang, Y.-T. and Frierson, D. M. W.: Increasing atmospheric poleward energy transport with warming in climate models, Journal of Climate, 24, 5931–5948, https://doi.org/10.1175/2011JCLI4172.1, 2011.

Illingworth, A., Battaglia, A., and Delanoe, J.: WIVERN: An ESA Earth Explorer Concept to Map Global in-Cloud Winds, Precipitation and Cloud Properties, in: 2020 IEEE Radar Conference (RadarConf20), pp. 1–6, https://doi.org/10.1109/RadarConf2043947.2020.9266286, 2020.

Illingworth, A. J., Battaglia, A., Bradford, J., Forsythe, M., Joe, P., Kollias, P., Lean, K., Lori, M., Mahfouf, J.-F., Melo, S., Midthassel, R., Munro, Y., Nicol, J., Potthast, R., Rennie, M., Stein, T. H. M., Tanelli, S., Tridon, F., Walden, C. J., and Wolde, M.: WIVERN: A New Satellite Concept to Provide Global In-Cloud Winds, Precipitation, and Cloud Properties, Bulletin of the American Meteorological Society, 99, 1669 – 1687, https://doi.org/10.1175/BAMS-D-16-0047.1, 2018.

Intergovernmental Panel on Climate Change (IPCC): Climate Change 2021: The Physical Science Basis, URL https://www.ipcc.ch/report/ar6/wg1/, accessed: 2025-03-09, 2021.

Kidd, C., Huffman, G., Maggioni, V., Chambon, P., and Oki, R.: The global satellite precipitation constellation current status and future requirements, Bulletin of the American Meteorological Society, 102, https://doi.org/10.1175/BAMS-D-20-0299.1, 2021.

Kollias, P., Puidgomènech Treserras, B., Battaglia, A., Borque, P. C., and Tatarevic, A.: Processing reflectivity and Doppler velocity from EarthCARE's cloud-profiling radar: the C-FMR, C-CD and C-APC products, Atmospheric Measurement Techniques, 16, 1901–1914, https://doi.org/10.5194/amt-16-1901-2023, 2023.

Kubar, T. L. and Waliser, D. E.: Cloud albedo variability and feedbacks in satellite observations and climate models, Journal of Geophysical Research: Atmospheres, 124, 8776–8790, https://doi.org/10.1029/2019JD030321, 2019.

Kulie, M. S., Milani, L., Wood, N. B., and L'Ecuyer, T. S.: Global Snowfall Detection and Measurement, pp. 699–716, Springer International Publishing, Cham, https://doi.org/10.1007/978-3-030-35798-6_12, 2020.

Kummerow, C., Barnes, W., Kozu, T., Shiue, J., and Simpson, J.: The Tropical Rainfall Measuring Mission (TRMM) Sensor Package, Journal of Atmospheric and Oceanic Technology, 15, 809–817, https://doi.org/10.1175/1520-0426(1998)015<0809:TTRMMT>2.0.CO;2, 1998.

Lamb, K. D., Singer, C. E., Loftus, K., Morrison, H., Powell, M., Ko, J., Buch, J., Hu, A. Z., van Lier-Walqui, M., and Gentine, P.: Perspectives on systematic cloud microphysics scheme development with machine learning, Journal of Advances in Modeling Earth Systems, 18, e2025MS005 341, https://doi.org/10.1029/2025MS005341, 2026.

Li, H., Möhler, O., Petäjä, T., and Moisseev, D.: Two-year statistics of columnar-ice production in stratiform clouds over Hyytiälä, Finland: environmental conditions and the relevance to secondary ice production, Atmos. Chem. Phys., 21, 14 671–14 686, https://doi.org/10.5194/acp-21-14671-2021, 2021.

Lionello, P. and et al.: The Hadley circulation in a changing climate, Annals of the New York Academy of Sciences, 1514, 25–45, https://doi.org/10.1111/nyas.15114, 2024.

Loeb, N. G., Ham, S.-H., Allan, R. P., and et al.: Observational Assessment of Changes in Earth's Energy Imbalance Since 2000, Surveys in Geophysics, 45, 1757–1783, https://doi.org/10.1007/s10712-024-09838-8, 2024.

Lopez-Cantu, T., Prein, A. F., and Samaras, C.: Uncertainties in Future U.S. Extreme Precipitation From Downscaled Climate Projections, Geophysical Research Letters, 47, e2019GL086 797, https://doi.org/10.1029/2019GL086797, e2019GL086797 10.1029/2019GL086797, 2020.

McKim, B., Bony, S., and Dufresne, J.-L.: Weak anvil cloud area feedback suggested by physical and observational constraints, Nature Geoscience, 17, 392–397, https://doi.org/10.1038/s41561-024-01414-4, 2024.

Milani, L. and Kidd, C.: The State of Precipitation Measurements at Mid-to-High Latitudes, Atmosphere, 14, https://doi.org/10.3390/atmos14111677, 2023.

Morrison, H., de Boer, G., Feingold, G., Harrington, J., Shupe, M. D., and Sulia, K.: Resilience of persistent Arctic mixed-phase clouds, Nature Geoscience, 5, 11–17, https://doi.org/doi.org/10.1038/ngeo1332, 2012.

Morrison, H., van Lier-Walqui, M., Fridlind, A. M., Grabowski, W. W., Harrington, J. Y., Hoose, C., Korolev, A., Kumjian, M. R., Milbrandt, J. A., Pawlowska, H., Posselt, D. J., Prat, O. P., Reimel, K. J., Shima, S.-I., van Diedenhoven, B., and Xue, L.: Confronting the Challenge of Modeling Cloud and Precipitation Microphysics, Journal of Advances in Modeling Earth Systems, 12, e2019MS001 689, https://doi.org/https://doi.org/10.1029/2019MS001689, e2019MS001689 2019MS001689, 2020.

Mroz, K., Montopoli, M., Battaglia, A., Panegrossi, G., Kirstetter, P., and Baldini, L.: Cross Validation of Active and Passive Microwave Snowfall Products over the Continental United States, Journal of Hydrometeorology, 22, 1297 – 1315, https://doi.org/10.1175/JHM-D-20-0222.1, 2021.

Mülmenstädt, J., Sourdeval, O., Delanoë, J., and Quaas, J.: Frequency of occurrence of rain from liquid-, mixed-, and ice-phase clouds derived from A-Train satellite retrievals, Geophysical Research Letters, 42, 6502–6509, https://doi.org/10.1002/2015GL064604, 2015.

Okamoto, K.: A Short History of the TRMM Precipitation Radar, pp. 187–195, American Meteorological Society, Boston, MA, https://doi.org/10.1007/978-1-878220-63-9_16, 2003.

Peral, E., Statham, S., Im, E., Tanelli, S., Imken, T., Price, D., Sauder, J., Chahat, N., and Williams, A.: The Radar-in-a-Cubesat (RAINCUBE) and Measurement Results, in: IGARSS 2018 - 2018 IEEE International Geoscience and Remote Sensing Symposium, pp. 6297–6300, https://doi.org/10.1109/IGARSS.2018.8519194, 2018.

Peral, E., Tanelli, S., Statham, S., Joshi, S., Im, E., Imken, T., Price, D., Sauder, J., Chahat, N., and Williams, A.: Raincube – A New Paradigm to Observe Weather Processes, in: IGARSS 2019 - 2019 IEEE International Geoscience and Remote Sensing Symposium, pp. 4978–4981, https://doi.org/10.1109/IGARSS.2019.8898687, 2019.

Perovich, D., Polashenski, C., Arntsen, A., and Stwertka, C.: Anatomy of a late spring snowfall on sea ice, Geophysical Research Letters, 44, 2802–2809, https://doi.org/10.1002/2016GL071470, 2017.

Quante, L., Willner, S. N., Middelanis, R., and Levermann, A.: Regions of intensification of extreme snowfall under future warming, Scientific Reports, 11, https://doi.org/doi.org/10.1038/s41598-021-95979-4, 2021.

Radhakrishnan, C., Chandrasekar, V., Reising, S. C., Berg, W., and Brown, S. T.: TEMPEST-D and GPM-GMI Observations Over Precipitating Systems: A Cross-Validation Study, IEEE Journal of Selected Topics in Applied Earth Observations and Remote Sensing, 16, 7422–7432, https://doi.org/10.1109/JSTARS.2023.3302025, 2023.

Reitebuch, O.: The Spaceborne Wind Lidar Mission ADM-Aeolus, pp. 815–827, Springer Berlin Heidelberg, Berlin, Heidelberg, https://doi.org/10.1007/978-3-642-30183-4_49, 2012.

Rennie, M. P., Isaksen, L., Weiler, F., de Kloe, J., Kanitz, T., and Reitebuch, O.: The impact of Aeolus wind retrievals on ECMWF global weather forecasts, Quarterly Journal of the Royal Meteorological Society, 147, 3555–3586, https://doi.org/10.1002/qj.4142, 2021.

Rodwell, M. J., Magnusson, L., Bauer, P., Bechtold, P., Bonavita, M., Cardinali, C., Diamantakis, M., Earnshaw, P., Garcia-Mendez, A., Isaksen, L., Källén, E., Klocke, D., Lopez, P., McNally, T., Persson, A., Prates, F., and Wedi, N.: Characteristics of Occasional Poor Medium-Range Weather Forecasts for Europe, Bulletin of the American Meteorological Society, 94, 1393 – 1405, https://doi.org/10.1175/BAMS-D-12-00099.1, 2013.

Salonen, K., Cotton, J., Bormann, N., and Forsythe, M.: Characterizing AMV height-assignment error by comparing best-fit pressure statistics from the met office and ECMWF data assimilation systems, Journal of Applied Meteorology and Climatology, 54, https://doi.org/10.1175/JAMCD-14-0025.1, 2015.

Seiki, T., Roh, W., and Satoh, M.: Cloud Microphysics in Global Cloud Resolving Models, Atmosphere-Ocean, 60, 477–505, https://doi.org/10.1080/07055900.2022.2075310, 2022.

Shaw, T. A. and Stevens, B.: The other climate crisis, Nature, 639, 877–887, https://doi.org/10.1038/s41586-025-08680-1, 2025.

Shaw, T. A., Arias, P. A., Collins, M., Coumou, D., Diedhiou, A., Garfinkel, C. I., Jain, S., Roxy, M. K., Kretschmer, M., Leung, L. R., Narsey, S., Martius, O., Seager, R., Shepherd, T. G., Sörensson, A. A., Stephenson, T., Taylor, M., and Wang, L.: Regional climate change: consensus, discrepancies, and ways forward, Frontiers in Climate, 6, https://doi.org/10.3389/fclim.2024.1391634, 2024.

Simpson, I. R., Shaw, T. A., Ceppi, P., Clement, A. C., Fischer, E., Grise, K. M., Pendergrass, A. G., Screen, J. A., Wills, R. C. J., Woollings, T., Blackport, R., Kang, J. M., and Po-Chedley, S.: Confronting Earth System Model trends with observations, Science Advances, 11, eadt8035, https://doi.org/10.1126/sciadv.adt8035, 2025.

Simpson, J., Kummerow, C., Tao, W. K., and Adler, R. F.: On the Tropical Rainfall Measuring Mission (TRMM), Meteorology and Atmospheric Physics, 60, 19–36, https://doi.org/10.1007/BF01029783, 1996.

Skofronick-Jackson, G., Petersen, W. A., Berg, W., Kidd, C., Stocker, E. F., Kirschbaum, D. B., Kakar, R., Braun, S. A., Huffman, G. J., Iguchi, T., Kirstetter, P. E., Kummerow, C., Meneghini, R., Oki, R., Olson, W. S., Takayabu, Y. N., Furukawa, K., and Wilheit, T.: The Global Precipitation Measurement (GPM) Mission for Science and Society, Bulletin of the American Meteorological Society, 98, 1679 – 1695, https://doi.org/10.1175/BAMS-D-15-00306.1, 2017.

Slatyer, R. A., Umbers, K. D. L., and Arnold, P. A.: Ecological responses to variation in seasonal snow cover, Conservation Biology, 36, e13 727, https://doi.org/10.1111/cobi.13727, 2022.

Sokol, A., L'Ecuyer, T. S., and Nesbitt, S. W.: Tropical Anvil Clouds: Radiative Driving Toward a Preferred Structure at High Altitudes, Journal of Geophysical Research: Atmospheres, 125, e2020JD033 107, https://doi.org/10.1029/2020JD033107, 2020.

Souverijns, N., Gossart, A., Gorodetskaya, I. V., Lhermitte, S., Mangold, A., Laffineur, Q., Delcloo, A., and van Lipzig, N. P. M.: How does the ice sheet

surface mass balance relate to snowfall? Insights from a ground-based precipitation radar in East Antarctica, The Cryosphere, 12, 1987–2003, https://doi.org/10.5194/tc-12-1987-2018, 2018a.

Souverijns, N., Gossart, A., Lhermitte, S., Gorodetskaya, I. V., Grazioli, J., Berne, A., Duran-Alarcon, C., Boudevillain, B., Genthon, C., Scarchilli, C., and van Lipzig, N. P. M.: Evaluation of the CloudSat surface snowfall product over Antarctica using ground-based precipitation radars, The Cryosphere, 12, 3775–3789, https://doi.org/10.5194/tc-12-3775-2018, 2018b.

Steiger, R., Scott, D., Abegg, B., Pons, M., and Aall, C.: A critical review of climate change risk for ski tourism, Current Issues in Tourism, 22, 1343–1379, https://doi.org/10.1080/13683500.2017.1410110, 2019.

Stephens, G., Winker, D., Pelon, J., Trepte, C., Vane, D., Yuhas, C., L'Ecuyer, T., and Lebsock, M.: CloudSat and CALIPSO within the A-Train: Ten Years of Actively Observing the Earth System, Bulletin of the American Meteorological Society, 99, 569 – 581, https://doi.org/10.1175/BAMS-D-16-0324.1, 2018.

Stephens, G. L., Vane, D. G., Tanelli, S., Im, E., Durden, S., Rokey, M., Reinke, D., Partain, P., Mace, G. G., Austin, R., L'Ecuyer, T., Haynes, J., Lebsock, M., Suzuki, K., Waliser, D., Wu, D., Kay, J., Gettelman, A., Wang, Z., and Marchand, R.: CloudSat mission: Performance and early science after the first year of operation, Journal of Geophysical Research: Atmospheres, 113, https://doi.org/10.1029/2008JD009982, 2008.

Strong, C. K., Ye, Z., and Shi, X.: Safety Effects of Winter Weather: The State of Knowledge and Remaining Challenges, Transport Reviews, 30, 677–699, https://doi.org/10.1080/01441640903414470, 2010.

Tanelli, S., Durden, S. L., Im, E., Pak, K. S., Reinke, D. G., Partain, P., Haynes, J. M., and Marchand, R. T.: CloudSat's Cloud Profiling Radar After Two Years in Orbit: Performance, Calibration, and Processing, IEEE Transactions on Geoscience and Remote Sensing, 46, 3560–3573, https://doi.org/10.1109/TGRS.2008.2002030, 2008.

Tao, W.-K., Takayabu, Y. N., Lang, S., Shige, S., Olson, W. S., Hou, A., Skofronick-Jackson, G., et al.: TRMM Latent Heating Retrieval: Applications and Comparisons with Field Campaigns and Large-Scale Analyses, Meteorological Monographs, 56, 2.1 – 2.34, https://doi.org/10.1175/AMSMONOGRAPHS-D-15-0013.1, 2016.

Toyoshima, K., Masunaga, H., and Furuzawa, F. A.: Early Evaluation of Ku- and Ka-Band Sensitivities for the Global Precipitation Measurement (GPM) Dual-Frequency Precipitation Radar (DPR), SOLA, 11, 14–17, https://doi.org/10.2151/sola.2015-004, 2015.

Trenberth, K. E.: Concepts of energy and moisture fluxes in the atmosphere, Bulletin of the American Meteorological Society, 72, 884–894, https://doi.org/10.1175/1520-0477(1991)072<0884:COEAMF>2.0.CO;2, 1991.

Trenberth, K. E. and Stepaniak, D. P.: Seamless poleward atmospheric energy transports and their components, Journal of Climate, 16, 3706–3723, https://doi.org/10.1175/1520-0442(2003)016<3706:SPAETA>2.0.CO;2, 2003.

Tridon, F., Battaglia, A., Rizik, A., Scarsi, F. E., and Illingworth, A.: Filling the Gap of Wind Observations Inside Tropical Cyclones, Earth and Space Science, 10, e2023EA003 099, https://doi.org/https://doi.org/10.1029/2023EA003099, e2023EA003099 2023EA003099, 2023.

van den Heever, S., Haddad, Z., Tanelli, S., Stephens, G., Posselt, D., Kim, Y., Brown, S., Braun, S., Grant, L., Kollias, P., et al.: The INCUS Mission, EGU General Assembly Conference Abstracts, pp. EGU22–9021, 2022.

Vogel, M.: Storm and Cloud Dynamics, 2nd edn., by W.R. Cotton, G.H. Bryan and S.C. van den Heever, Contemporary Physics, 52, 610–611, https://doi.org/10.1080/00107514.2011.591941, 2011.

Wall, C. J., L'Ecuyer, T. S., and Stephens, G. L.: The lifecycle of anvil clouds and the top-of-atmosphere radiation balance over the tropical West Pacific, Journal of Climate, 31, 10 133–10 151, https://doi.org/10.1175/JCLI-D-18-0154.1, 2018.

Wasti, A., Ray, P., Wi, S., Folch, C., Ubierna, M., and Karki, P.: Climate change and the hydropower sector: A global review, WIREs Climate Change, 13, e757, https://doi.org/10.1002/wcc.757, 2022.

Wehr, T., Kubota, T., Tzeremes, G., Wallace, K., Nakatsuka, H., Ohno, Y., Koopman, R., Rusli, S., Kikuchi, M., Eisinger, M., Tanaka, T., Taga, M., Deghaye, P., Tomita, E., and Bernaerts, D.: The EarthCARE mission – science and system overview, Atmospheric Measurement Techniques, 16, 3581–3608, https://doi.org/10.5194/amt-16-3581-2023, 2023.

Wernli, H. and Gray, S. L.: Recent advances in understanding extratropical cyclone dynamics and predictability, Quarterly Journal of the Royal Meteorological Society, in press, 2024.

Zeng, X., Wu, P., and L'Ecuyer, T. S.: Weak anvil cloud area feedback suggested by physical and observational constraints, Geophysical Research Letters, 51, e2023GL103 219, https://doi.org/10.1029/2023GL103219, 2024.

Chapter 2

Overview of key and critical aspects in space-borne radars remote sensing

2 OVERVIEW OF KEY AND CRITICAL ASPECTS IN SPACE-BORNE RADARS REMOTE SENSING

Radars (RAdio Detection And Ranging) are instruments that emits a strong signal at radio or microwave frequencies and captures the echoes that occur if the signal is reflected from objects known as targets or scatterers (Doviak and Zrnić, 1993; Bringi and Chandrasekar, 2001; Fabry, 2015). Power, time, frequency and phase of the received signal, are used to infer properties of the scatterer medium, such as the range, the water content, the characteristic size of the hydrometeor particles and their velocity. The steps describing how a pulsed radar works can be summarized as follow:

1. the radar transmitter generates a strong microwave signal, in a form of a pulse of a given duration, τ_p;

2. the signal is radiated in a specific angular direction by the transmitting antenna, following a given radiation pattern of the antenna, in order to retrieve information of targets located along a specific direction;

3. part of the signal is backscattered (typically a little fraction of the emitted signal) and such echo is received by the receiving antenna;

4. the received signal is processed to retrieve information on the scatterers.

Weather radar operates in specific frequency bands that can penetrate the atmosphere with little or no absorption by atmospheric gases and water vapor.

2.1 RADAR REFLECTIVITY FACTOR

The received power sampled from the echo of distributed targets in the volume centred in r and extended between $r - c\,\tau_p/2$ and $r + c\,\tau_p/2$, where c is the speed of light, is typically expressed in terms of radar reflectivity factor per unit volume, Z:

$$P_r(r) = C_M \frac{Z(r)\,T(0,r)}{r^2} \qquad \text{where } C_M \equiv \frac{\pi^2}{2^6}\frac{P_t\,G_0^2\Omega_{2A}}{\lambda^2}\frac{c\,\tau_p}{2}|K_w|^2 \qquad (2.1)$$

where:

- P_t is the total emitted power

- $P_r(t)$ is the received power from scatterers at time t, corresponding to the sampling volume at distance r from the instrument along the antenna boresight direction;

- r is the range, i.e. the distance, of the scatterers contributing to the echo sampled at time t: $r = \frac{c(t-t_0)}{2}$, where t_0 is the time at which the pulse is transmitted, and t is the time at which the echo is received;
- $T(0,r)$ is the transmittance of the atmosphere (due to gas and hydrometeors) along the path between the radar at range 0 and the sampling volume at range r;
- K_w is the dielectric constant of water at the given wavelengths and at $10°$C;
- G_0 is the antenna gain at the boresight;
- Ω_{2A} is the integral of the antenna radiation pattern along the 2π solid angle.

Z depends on the physical properties of the scatterer volume:

$$Z = \frac{\lambda^4}{\pi^5 |K_w|^2} \int_0^\infty \sigma_b(D) N(D) dD \tag{2.2}$$

where $N(D)$ is the Particle Size Distribution (PSD), which characterize how the particles are distributed with the size in the given volume, and $\sigma_b(D)$ is the backscattering cross-section of the individual particle of size D. σ_b does not only depend on the size but also on the shape and other physical properties of the particle, such as the temperature and the phase.

The minimum single-pulse detectable reflectivity of the instrument (Z_{min}), also known as single-pulse sensitivity, can be computed by substituting Eq. 2.2 in Eq. 2.1 and by assuming that the power output for the receiver is equal to the noise power ($P_r \equiv P_{noise}$). This shows that the larger is λ, the larger is Z_{min}. Typically, multiple pulses are integrated in order to reduce the noise component and improve the overall sensitivity of the measurement. As a reference, the CloudSat W-band radar sensitivity after integration is around -30 dBZ, while for the GPM Ka-band radar it is around +13 dBZ.

The transmitted signal and the echo are subject to the attenuation due to atmospheric gases and scatterers in the medium along the two-way propagation path, $A = e^{-2\tau}$, where τ is the optical depth of the medium along the one-way path. This is expressed in Eq. 2.1 through the term $T(0,r)$.

2.2 THE DOPPLER VELOCITY

Doppler radars have the capability to retrieve the radial velocity of scatterers in the sampling volume along the LoS of the antenna. The target volume consists of a distribution of hydrometeor particles, where each of them has a different radial velocity. The mean reflectivity weighted velocity of the ensemble is

$$v_D = \frac{\int_0^\infty v(D)\sigma_b(D)N(D)dD}{\int_0^\infty \sigma_b(D)N(D)dD} \tag{2.3}$$

and the variance is

$$s_D^2 = \frac{\int_0^\infty (v(D) - v_D)^2 \, \sigma_b(D)N(D)dD}{\int_0^\infty \sigma_b(D)N(D)dD} \tag{2.4}$$

Therefore, the resulting backscattered signal corresponds to a spectrum of Doppler velocities. Such signal is a complex voltage that can be represented in terms of in-phase (I) and quadrature (Q) components. From these, estimators algorithm are used to

retrieve the phase shift between the echo of one pulse and the echo of the successive one (Zrnic, 1975; Doviak and Zrnić, 1993; Battaglia et al., 2025), and the spectral width. The mean Doppler velocity is then retrieved by the phase shift, $\Delta\phi$, as:

$$v_D = -\frac{\lambda}{4\pi\, T_s}\Delta\phi \tag{2.5}$$

where λ is the wavelength of the transmit pulse, and T_s is the pulse repetition interval that indicates the time elapsed between the transmission of two successive pulses.

2.3 AMBIGUITIES

The maximum unambiguous range is dictated by the pulse repetition interval, T_s, and is $r_a = cT_s/2$.

Also, given a set of sampled phases, it is not possible to relate them to one unique Doppler frequency: any of the frequencies $\frac{\Delta\gamma}{2\pi T_s} + \frac{n}{T_s}$, where n is an integer number, and $-\pi < \Delta\gamma \leq \pi$, could be a correct Doppler shift. Thus, there is an unambiguous velocity range whose boundaries are dictated by $v_s = \pm\lambda/\left(4T_s\right)$, with $v_N = \lambda/\left(2T_s\right)$ called the Nyquist velocity. The Nyquist velocity can be increased by increasing T_s. However, this would also decrease the unambiguous range, limiting the possibility of increasing the Nyquist. A technique called Polarization Diversity Pulse Pair (PDPP) Battaglia et al. (2013) has been developed to partially overcome this limitation.

2.4 CRITICAL ASPECTS OF SPACE-BORNE RADARS

The derivation of geophysical products from radar measurements is a complex task and is further complicated by phenomenon that are intrinsic to the concept of space-borne radar. In fact, radar measurements from low Earth orbit satellites are challenging (Tanelli et al., 2002; Battaglia et al., 2020; Kollias et al., 2022) due to the large spacecraft velocity (typically, in low Earth Orbit, it is of the order of 7.6 km s^{-1}), the large altitude and the platform motion.

Satellite Doppler fading Large spacecraft velocity, in combination with a finite antenna beamwidth, causes "satellite Doppler fading", i.e. a broadening of the Doppler spectrum, which is a synonym of a decreased medium correlation time (Kobayashi et al., 2002). This generally increases the uncertainties in the Doppler estimates performed with radar pulse pair estimators (Doviak and Zrnić, 1993). In order to mitigate this issue, techniques based on polarization diversity (Battaglia et al., 2013; Wolde et al., 2019) and Displaced Phase Center Antenna (Durden et al., 2007; Tanelli et al., 2016; Kollias et al., 2022) concepts have been proposed. The first technique is employed in WIVERN.

Pointing knowledge The Doppler velocity retrieved by space-borne radar depends on the relative velocity between the hydrmeteor and the satellite. Therefore, it is the results of the combination of two components: 1) the LoS velocity of the atmospheric targets ($v_{D,atm}$), and 2) the projection of the satellite velocity (v_{SC}) along the LoS. 2) is subtracted to the measured Doppler velocity to retrieve 1). Uncertainty in the knowledge of the pointing, even of few tens of μradians, can lead to very large errors in the retrieval of the velocity of the targets due to the very large platform velocity (Scarsi et al., 2024). This issue is discussed in Chapter 3 (Scarsi et al., 2024) for the WIVERN

conically scanning Doppler radar. Four methods are proposed to characterize its mis-pointing and correct for the induced error in Doppler velocity.

Large footprint and MS effects As the instrument is moving in a Low Earth Orbit (LEO), tenths of degrees of beamwidth translates in km scale footprints. The dimension of the radar's footprint is not only related to the spatial resolution of its measurements. A large footprint, enhances the "satellite Doppler fading", Non Uniform Beam Filling (NUBF), and MS effects further complicating the retrievals of the geophysical quantities. MS effects, which are discussed in Chapter 5, are enhanced by the presence of large high reflective ice particles (i.e. hail and graupel) that are typically generated in convective storms.

NUBF As the Doppler velocity is reflectivity weighted, inhomogeneity in reflectivity (i.e. water content, particle shape and distribution) within the radar footprint can significantly alter the shape, average value and width of the Doppler spectrum (Tanelli et al., 2002). The average Doppler velocity will be then biased towards velocity values of the brightest scatterers. NUBF effects are strong in space-borne Doppler radars due to the large sampling volume as the likelihood of encountering inhomogeneous systems are larger. The larger is the footprint, more likely is to come across NUBF.

Aliasing When the geophysical velocity we want to measure is larger than the Nyquist velocity, the measured Doppler velocity is "folded" and "wrapped around" $\pm\, v_N/2$. This phenomenon called aliasing further complicating the retrievals where the geophysical velocity happens to be larger in magnitude than the Nyquist, i.e. typically occurs in convective systems.

Sampling capabilities Although space-borne radars provide the best coverage of measurements, days can pass between an overpass over the same location. This translates in many years of measurements needed to build a climatology with acceptable uncertainties. WIVERN tries to overcome this problem with its conically scanning radar, which, thanks to its 800 swath width is expected to collect 70 times more samples than a fixed near nadir looking radar. An assessment of the sampling capabilities of WIVERN is done in Chapter 4, with a focus on the sampling of snow precipitation in the polar regions, which is of primary importance for the estimation of the ice-sheets mass balance.

Simulation of Level-1 products The simulation of Level-1 (L1) products, e.g. the radar reflectivity and Doppler velocity, serves as a numerical rehearsal of the radar measurements expected from orbit. This process plays a crucial role in the design and development phases of space-borne atmospheric radar missions, as it enables the assessment of instrument performance and data quality prior to hardware realization. Several key motivations underpin the need for such simulations:

- **Mission feasibility and requirements definition**: L1 product simulations allow to evaluate different instrument configurations under realistic atmospheric conditions. Through these simulations, it becomes possible to quantify key performances. This information is vital for defining system requirements and ensuring that the proposed instrument design can achieve the desired scientific objectives.

- **Development and testing of retrieval algorithms**: before launch, it is essential to develop and validate the algorithms responsible for transforming raw radar data (Level 0) into calibrated reflectivity and Doppler measurements (Level 1). Simulated L1 datasets provide a realistic and controlled environment for testing these algorithms. They enable verification of calibration procedures, assessment of error propagation, and development of higher-level (Level 2) retrieval algorithms used to derive geophysical quantities such as rainfall rate, cloud microphysical properties, and atmospheric winds from the radar measurements.
- **End-to-end mission performance evaluation**: L1 simulations also support comprehensive end-to-end mission performance studies. By modeling the entire signal pathway, from orbit geometry and radar signal propagation, through atmospheric scattering and detection, to onboard and ground-based processing, it is possible to identify potential performance limitations and sources of bias. These include effects such as MS, surface clutter, and Doppler aliasing, which can significantly impact data quality if not properly accounted for in mission design.
- **Observation scenario assessment**: L1 simulations are necessary to evaluate the observability of different atmospheric structures. By simulating a variety of meteorological conditions (e.g., thin cirrus, light rain, deep convection), it is possible to determine which phenomena the radar will be capable of detecting. Such analyses also facilitate comparisons between alternative mission configurations, ensuring that the final mission architecture maximizes scientific return.

REFERENCES

Battaglia, A., Tanelli, S., and Kollias, P.: Polarization Diversity for Millimeter Spaceborne Doppler Radars: An Answer for Observing Deep Convection?, Journal of Atmospheric and Oceanic Technology, 30, 2768–2787, https://doi.org/10.1175/JTECH-D-13-00085.1, 2013.

Battaglia, A., Kollias, P., Dhillon, R., Roy, R., Tanelli, S., Lamer, K., Grecu, M., Lebsock, M., Watters, D., Mroz, K., Heymsfield, G., Li, L., and Furukawa, K.: Spaceborne Cloud and Precipitation Radars: Status, Challenges, and Ways Forward, Reviews of Geophysics, 58, e2019RG000 686, https://doi.org/10.1029/2019RG000686, e2019RG000686 10.1029/2019RG000686, 2020.

Battaglia, A., Rizik, A., Sikaneta, I., and Tridon, F.: I and Qs Simulation and Processing Envisaged for Spaceborne Polarization Diversity Doppler Radars, IEEE Transactions on Geoscience and Remote Sensing, 63, 1–14, https://doi.org/10.1109/TGRS.2025.3529672, 2025.

Bringi, V. N. and Chandrasekar, V.: Polarimetric Doppler Weather Radar: Principles and Applications, Cambridge University Press, Cambridge, 2001.

Doviak, R. J. and Zrnić, D. S.: Doppler Radar and Weather Observations, Academic Press, 1993.

Durden, S. L., Siqueira, P. R., and Tanelli, S.: On the Use of Multiantenna Radars for Spaceborne Doppler Precipitation Measurements, IEEE Geosci. Remote Sens. Lett., 4, 181–183, https://doi.org/10.1109/LGRS.2006.887136, 2007.

Fabry, F.: Radar meteorology: Principles and practice, Cambridge University Press, https://doi.org/10.1017/CBO9781107707405, 2015.

Kobayashi, S., Kumagai, H., and Kuroiwa, H.: A Proposal of Pulse-Pair Doppler Operation on a Spaceborne Cloud-Profiling Radar in the W Band, Journal of Atmospheric and Oceanic Technology, 19, 1294 – 1306, https://doi.org/10.1175/1520-0426(2002)019<1294:APOPPD>2.0.CO;2, 2002.

Kollias, P., Battaglia, A., Lamer, K., Treserras, B. P., and Braun, S. A.: Mind the Gap - Part 3: Doppler Velocity Measurements From Space, Frontiers in Remote Sensing, 3, https://doi.org/10.3389/frsen.2022.860284, 2022.

Scarsi, F. E., Battaglia, A., Tridon, F., Martire, P., Dhillon, R., and Illingworth, A.: Mispointing characterization and Doppler velocity correction for the conically scanning WIVERN Doppler radar, Atmospheric Measurement Techniques, 17, 499–514, https://doi.org/10.5194/amt-17-499-2024, 2024.

Tanelli, S., Im, E., Durden, S. L., Facheris, L., and Giuli, D.: The Effects of Nonuniform Beam Filling on Vertical Rainfall Velocity Measurements with a Spaceborne Doppler Radar, Journal of Atmospheric and Oceanic Technology, 19, 1019 – 1034, https://doi.org/10.1175/1520-0426(2002)019<1019:TEONBF>2.0.CO;2, 2002.

Tanelli, S., Durden, S. L., and Johnson, M. P.: Airborne Demonstration of DPCA for Velocity Measurements of Distributed Targets, IEEE Geosci. Remote Sens. Lett., 13, 1415–1419, https://doi.org/10.1109/LGRS.2016.2581174, 2016.

Wolde, M., Battaglia, A., Nguyen, C., Pazmany, A. L., and Illingworth, A.: Implementation of polarization diversity pulse-pair technique using airborne W-band radar, Atmospheric Measurement Techniques, 12, 253–269, https://doi.org/10.5194/amt-12-253-2019, 2019.

Zrnic, D. S.: Simulation of weatherlike Doppler spectra and signal, J. Appl. Meteorol., 14, 619–620, 1975.

Chapter 3

Mispointing characterization and Doppler velocity correction for the conically scanning WIVERN Doppler radar

This chapter is extensively based on the following publication:
Scarsi et al. (2024), *Mispointing characterization and Doppler velocity correction for the conically scanning WIVERN Doppler radar*; https://doi.org/10.5194/amt-17-499-2024

3 MISPOINTING CHARACTERIZATION AND DOPPLER VELOCITY CORRECTION FOR THE CONICALLY SCANNING WIVERN DOPPLER RADAR

In the measurement of the Doppler velocity, the measured velocity is the combination of geophysical velocity and the platform velocity (i.e. the satellite) components along the line of sight. If the satellite velocity is known, the geophysical velocity along the LoS can be retrieved. Uncertainty in the knowledge of the pointing direction, i.e. the line of sight direction, can lead to very large errors in the retrievals of the hydrometeor velocity. For space-borne radars, a very precise and accurate knowledge of the antenna pointing is required to enable the subtraction of the non-geophysical component of the satellite velocity along the line of sight (Tanelli et al., 2004; Battaglia and Kollias, 2014). The different sources of errors involved with a conically scanning Doppler radar with polarization diversity, as adopted for WIVERN, have been thoroughly discussed in Battaglia et al. (2018, 2022) and Rizik et al. (2023). End to end simulations suggest that the WIVERN mission requirements on horizontal-projected line of sight winds, of a total random (systematic) error lower than 3 (0.5) m s^{-1} at an integration distance of 20 km for reflectivities above -15 dBZ, are at reach. Such accuracy is expected to be sufficient to ensure significant impact in operational NWP.

In previous error budget studies, antenna mispointing errors have been considered negligible in the overall error budget (i.e. $\lessapprox 0.3$ m s^{-1} both for bias and random error, e.g. see Fig. 11 in Battaglia et al. (2022)). Phase 0 industry studies suggest that the mispointing Power Spectral Density has indeed larger components than previously expected, particularly for very slow varying components. This is due to a predicted larger uncertainty on the knowledge of the antenna boresight alignment after the launch compared to pre-launch ground measurements. Therefore the different error contributions have been classified and assigned to systematic errors or random errors according to the split frequency of 1.16e-5 Hz (which corresponds to 1 day period). In order to fulfill the mission requirements, when accounting for the other contributions (pulse pair estimator error, non uniform beam filling, wind shear, see Tridon et al. (2023)) the pointing contribution of the random LoS Doppler velocity error budget must be of the order of 0.4-0.6 m s^{-1} whereas the requirement for the systematic contribution has to be smaller than 0.3-0.6 m s^{-1}. At the moment, these latter figures are far from being achieved (of the order of 1.7 and 5.6 m s^{-1} for the two industrial consortia, ESA (2023)).

For the purpose of the mission (i.e. measuring accurate Doppler velocities), it is not paramount to have an accurate and precise pointing, but it is essential to achieve pointing knowledge within tens of microradians. Thus, methodologies to quantify the antenna mispointing are highly desired in the context of the WIVERN mission and in general for scanning atmospheric Doppler radars. In this paper, after introducing the

geometry of observation and the impact of mispointing errors on LoS Doppler velocities (Sect. 3.1), different Doppler velocity correction methods are proposed and reviewed, discussing their potential for reducing the mispointing errors (Sect. 3.2). Conclusions and future work are outlined in Sect. 3.3. The methods described in the paper characterize the antenna mispointing angles and correct the error in the Doppler velocity induced by such mispointing values. These methodologies do not correct the antenna pointing itself.

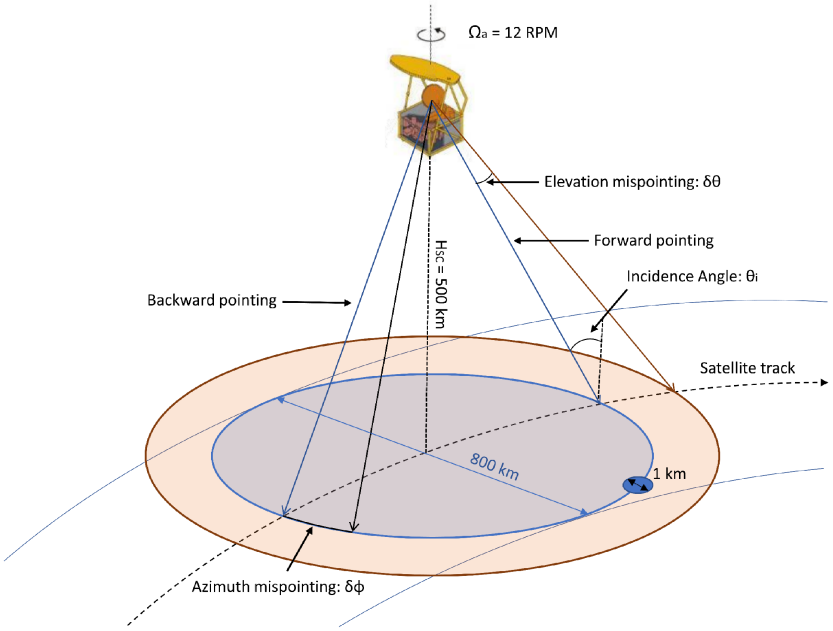

Fig. 3.0.1: *Geometry of observation of the WIVERN conically scanning radar: the antenna boresight, indicated by a thin blue line, is rotating at 12 RPM and pointing at a nominal incidence angle of about 42°. The orange and the black arrows represent an elevation and an azimuthal mispointing in correspondence to the forward and backward pointing configuration, respectively.*

3.1 MISPOINTING ERRORS

Fig. 3.0.1 depicts the geometry of observation of the WIVERN radar, whose specifics are listed in Tab. 1.3.1. Mispointing in the knowledge of the antenna boresight produces error in the estimates of the hydrometeor Doppler velocity, v_D, because the component of the spacecraft velocity, v_{SC}, along the antenna boresight needs to be subtracted from the measured Doppler velocity, v_{mD}: $v_D = v_{mD} - v_{SC}\sin(\theta)\cos(\phi)$, with the last term representing the projection of v_{SC} along the antenna boresight. If the actual pointing of the antenna has a mispointing of $\delta\theta$ in the elevation angle and of $\delta\phi$ in the

azimuthal, then the mispointing error in Doppler velocity δv_{mis} will be:

$$\begin{aligned}
\delta v_{mis} &= [v_{mD} - v_{SC}\sin(\theta)\cos(\phi)] - [v_{mD} - v_{SC}\sin(\theta+\delta\theta)\cos(\phi+\delta\phi)] \\
\frac{\delta v_{mis}}{v_{SC}} &= [\sin(\theta+\delta\theta)\cos(\phi+\delta\phi) - \sin(\theta)\cos(\phi)] = \\
&\quad [(\sin(\theta)+\cos(\theta)\delta\theta)\,(\cos(\phi)-\sin(\phi)\delta\phi) - \sin(\theta)\cos(\phi)] \\
\delta v_{mis} &= v_{SC}\,[-\sin(\theta)\sin(\phi)\delta\phi + \cos(\theta)\cos(\phi)\delta\theta] \qquad (3.1)
\end{aligned}$$

where the azimuthal scanning angle is assumed 0° in the forward direction. Eq. 3.1 implies that the error in the LOS velocity is modulated by the azimuthal scan frequency since $\phi = \Omega_a t + \phi_0$, where $\Omega_a = 1.26$ rad s^{-1} is the antenna angular rotation velocity. Note that a 100 μrad error in azimuth (elevation) produces a maximum error of 0.5 (0.57) m s^{-1} when looking sideways (forward/backward direction). Note that the sideways directions correspond to $\phi = \pm\pi/2$, and the forward and backward directions to $\phi = 0$ and $\phi = \pi$, respectively. Finally, it is important to highlight that in Eq. (3.1) and in the following discussion the antenna rotation axis is assumed vertical; the impact of a scan axis mounting offset is discussed in Sect. 3.A.

3.2 DOPPLER VELOCITY CORRECTION METHODS

Four different methods have been identified that can be used to correct Doppler velocity errors. Methods II and III are applicable both to azimuth and elevation mispointing, method I is applicable only to elevation mispointing and method IV only to azimuthal mispointing; the first two (I and II) are effective on short time scales (of the order of few ms), the latter two (III and IV) on much longer time scales (weeks/months).

3.2.1 Correction method I: altimeter mode technique

Because of its peculiar illumination geometry, pulse shape and the receiver IF filter response (Meneghini and Kozu, 1990), the WIVERN radar will produce a very specific reflectivity shape for flat surfaces in absence of low level clouds and/or precipitation, with a peak corresponding to the surface range along the boresight direction (Battaglia et al. (2017); Illingworth et al. (2020)). Since the position of the spacecraft is extremely well known, any discrepancy δz between the range of the surface from the spacecraft computed along the (Attitude and Orbit Control Subsystem (AOCS) - estimated) boresight direction and the measured range of the surface peak can be attributed to an elevation mispointing, $\delta\theta$, from:

$$\delta\theta = \frac{\delta z}{r_{SC}\ \sin\theta_i} \approx \frac{\delta z\ \cos\theta_i}{\sin\theta_i\ H_{SC}} \qquad (3.2)$$

where r_{SC} is the distance between the surface and the spacecraft along the boresight and H_{SC} is the spacecraft altitude. With the WIVERN specifics (see Tab. 1.3.1), a $\delta z = 10$ m corresponds to about 22.5 μrad. Unfortunately, this method is not viable for tackling the azimuth mispointing, but has the advantage that it depends only on the reflectivity profile, thus it has the same sensitivity in each part of the scan.

In order to understand the uncertainties associated with this method, realistic surface returns as detected by WIVERN have been simulated starting from the expected flat surface return shape derived following Meneghini and Kozu (1990) (Fig. 5 in Illingworth et al. (2020); an example of a surface return is provided in Fig. 3.2.1, black line).

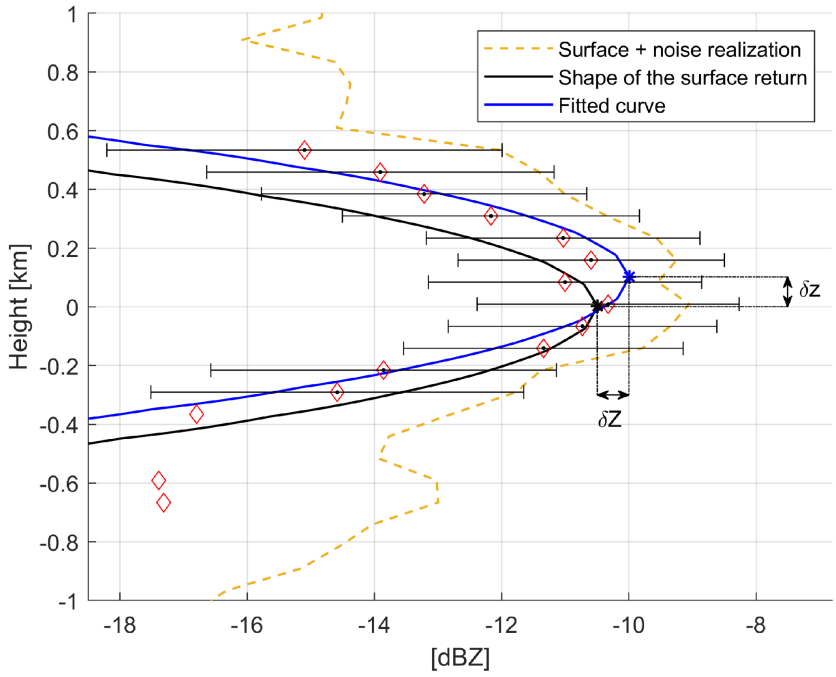

Fig. 3.2.1: *A reflectivity surface profile simulated as observed by the WIVERN radar with the procedure to determine the vertical displacement δz of the peak of the noisy sampled profile with respect to the actual surface peak. The black line represents the ideal shape of the surface return for a 7 dB PNR with its peak highlighted by a black star. The orange dashed line represents a stochastic realization of the same surface return with a -15 dBZ random noise. The red diamonds represent the digitized signal after noise subtraction with the error bars indicating the expected errors in the reflectivity estimates. The black dots insides the red diamonds correspond to the points sampled by the radar that are used for fitting the surface profile. The blue line is the best fitting profile, with the peak highlighted by a blue star. The displacements in height (δz) and in amplitude (δZ) between the black and blue stars are indicative of the uncertainties associated to the clutter characterization.*

The profiles have been scaled in order to produce different PNRs, defined as the ratio between the peak reflectivity of the surface profile and the single pulse sensitivity or reflectivity equivalent noise level of the radar, assumed to be equal to -15 dBZ. For each PNR and each integration length (with 8 independent pulses per km), different stochastic realizations of the signal plus the noise are simulated following the technique proposed by Zrnic (1975). One of such possible realizations is shown as the orange dashed line in Fig.3.2.1. Then the signal is noise subtracted (similarly to the method described in (Kollias et al., 2023)) and sampled at the WIVERN sampling rate (100 m along the range, see Tab. 1.3.1) with random range offsets in order to account for the variability of the digitization process along the orbit (red diamonds in Fig. 3.2.1). A surface detection criterion is introduced. For each profile, only points that are 3 dB above the detection level (red diamonds with black points inside) are considered. If the profile contains at least 10 consecutive points above the detection threshold, it is then used for fitting the surface return shape with two free parameters: the peak height and the peak amplitude. The fit is performed via a least mean square procedure where each point

is weighted by the expected error (error-bars in Fig. 3.2.1) computed according to the SNR (following Eq. 16 in Battaglia et al. (2022)). The best fitting curve (blue line) differs from the actual profile for a shift in height, δz, and a shift in amplitude, δZ. The variability of δz can be statistically retrieved as a function of the PNR by generating a sufficient number of profile realizations with different random noise and different digitalizations of the signal. While, as expected (not shown), the mean value of δz over different digitization and stochastic noise is practically close to 0 m for every PNR and for every integration length, its standard deviation, $\sigma_{\delta z}$, decreases when either the PNR and/or the integration length increase, as shown in Fig. 3.2.2. The shifts in elevation angle $\delta\theta$ corresponding to the shifting in altitude δz of the peak are reported on the y-axis on the right hand side of Fig. 3.2.2. For instance, with a PNR of 10 dB, the surface position is expected to be determined with an error of about 32, 20, 13 and 9 m for integration lengths of 1, 2, 5, 10 km, respectively. These values correspond to an uncertainty in elevation of 75, 47, 39 and 20 μrad. According to Eq. 3.1, the last three solutions guarantee that the velocity error induced by such mispointing will always remain below 0.3 m s^{-1}.

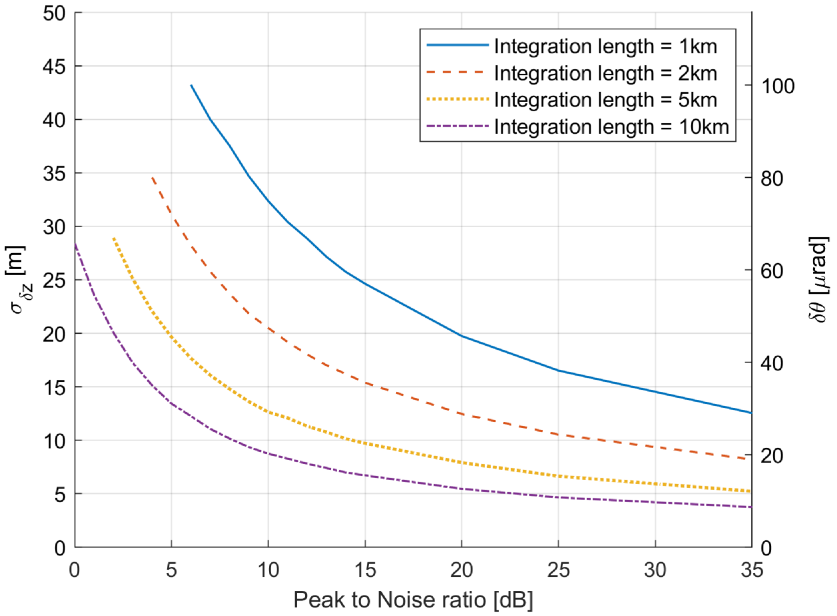

Fig. 3.2.2: *Uncertainty in the elevation mispointing determination by the altimeter mode technique: standard deviations of δz, $\sigma_{\delta z}$ (left axis), and $\delta\theta$ (right axis) as a function of the PNR for different integration lengths, as indicated in the legend. The mean values of δz are negligible for all analyzed PNR and integration lengths (not shown). The curves are drawn only for PNRs high enough that more than 80 % of the profiles satisfy the surface detection criterion. See text for details.*

Statistics of useful surface return

Estimates of the frequency of surfaces exceeding threshold values of PNR have been obtained by exploiting the climatology gathered by the polar-orbiting nadir-pointing

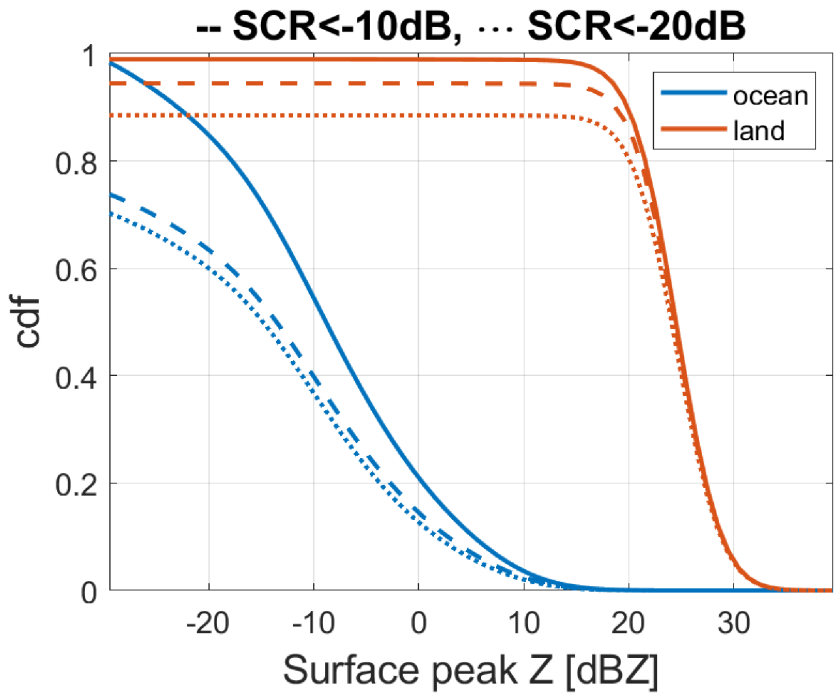

Fig. 3.2.3: *Cumulative distributions of surface reflectivity peaks as expected in WIVERN observations for land (red) and ocean (blue) surfaces. Dashed and dotted lines correspond to rays characterized by decreasing signal to clutter ratios (see the text for more details).*

CloudSat W-band radar and simulating the WIVERN returns at slant incidence angle. The method, proposed by Battaglia et al. (2018) and refined in Tridon et al. (2023), accounts for the additional path integrated attenuation and the reduction in surface normalized backscattering cross sections (Battaglia et al., 2017) when considering the slanted viewing geometry of the WIVERN radar. Fig. 3.2.3 shows the cumulative distribution functions (cdf) of the surface peaks (and equivalently of PNR) for land and ocean surfaces. Since ocean surfaces are far less bright than land surfaces at WIVERN incidence angles, a lower percentage of sea than land surface profiles exceeds any given threshold. For instance, more than 36 % and 99 % of the surface peaks exceed -5 dBZ (i.e. PNR=10 dB) for ocean and land surfaces, respectively. Two factors can actually decrease the number of surface returns effectively useful for the calibration:

1. the presence of low clouds and precipitation that could perturb the shape of the reflectivity and of the Doppler velocity profile (discussed later in Sect. 3.2.2);

2. for land surfaces, the failure of the flat surface assumption.

In order to assess the first issue, we have recomputed the cdf excluding rays where the hydrometeor signal to clutter ratio (SCR) is higher than -20 dB (dotted lines) and -10 dB (dashed lines) in the 750 m closest to the surface. These conditions ensure that the clutter signal is 100 and 10 times stronger than any perturbing signal produced by the hydrometeors. The presence of low clouds will further reduce the number of useful rays for calibration but such reduction is only of 10 % for Signal to Clutter Ratio (SCR)

lower than -10 dB and of 13 % for SCR lower than -20 dB over ocean. Over land, the reduction is even smaller with 5 % and 10 % for SCR lower than -10 dB and -20 dB, respectively.

For estimating the impact of the second issue see the discussion in Sect. 3.2.2.

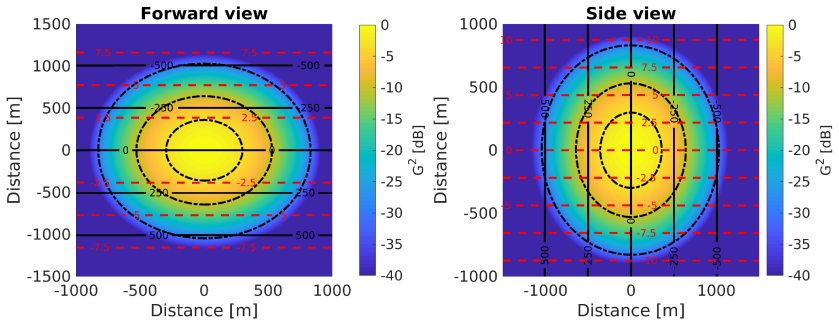

Fig. 3.2.4: *Square of the gain (normalized to 0 dB at boresight) for the WIVERN antenna pattern as derived from a previous study (Lori et al. (2017)) for points within 1500 m from the ground projection of the boresight (used as origin of the coordinate system). Results are reported in correspondence to the forward ($\phi = 0$, left panel) and side ($\phi = 90°$, right panel) view. In both cases the satellite is assumed to move along the y-axis. Contour levels of the satellite velocity along the LoS are plotted as dashed red lines from -10 to 10 m s^{-1} with 2.5 m s^{-1} separation; contour levels of height above the ground are plotted as black lines from -500 to 500 m with 250 m separation. The dotted black lines correspond to -3, -10 and -30 dB of the normalized square gain.*

3.2.2 Correction method II: surface Doppler technique

Flat and still surfaces are characterized by a well-determined Doppler velocity profile. But, while the surface reflectivity profiles are independent on the azimuthal scanning angle, the Doppler velocity profiles are azimuthal dependent. Under the assumption of an homogeneous (i.e. backscattering cross section constant across the footprint) flat and still surface, at side view, the surface Doppler velocity is expected to have 0 m s^{-1} at all height bins, whereas, at other azimuthal angles, positive and negative Doppler velocities are expected above and below the surface with 0 m s^{-1} only in correspondence to the surface height (black line in Fig. 3.2.5). This is the result of the different orientation of the lines of constant Doppler shift induced by v_{SC} (isodops) with respect to the lines with constant range. As demonstrated in Fig. 3.2.4, for the two extreme cases of forward (left panel) and side (right panel) views the isodops are parallel and perpendicular, respectively, to the lines of constant range from the radar.

Like done in Sect. 3.2.1, the Doppler returns as measured by the WIVERN radar are simulated with the noisiness proper to the given PNR and number of independent samples (according to Eq. (16) in Battaglia et al. (2022), diamonds in Fig. 3.2.5). Here, a perfect correlation between the V and the H pulse co-polar signals is assumed consistently with low surface Linear Depolarization Ratio (LDR) values (Wolde et al., 2019). The expected shape (black line) is then fitted through the data that have reflectivites exceeding an SNR of 0 dB via a mean least square technique. The distance of the fitted profile (blue line) from the expected profile at zero height (δv_D) is indicative of

the uncertainty in the Doppler velocity error estimation that can be achieved with this methodology.

Fig. 3.2.6 shows the Doppler velocity uncertainties associated with this method. In this case to reduce the error to values lower than 0.4 m s^{-1} is impractical at short integration lengths ($\leq$ 2km) and requires surface with PNR exceeding 10 and 15 dB for integration lengths of 5 and 10 km, respectively. When comparing the curves at different integration lengths, it can be noted that, approximately, the error drops with the square root of the integration length. Therefore this technique seems very promising for correcting mispointing modulated on time scales longer than the antenna rotational period. Surface returns for full rotations in correspondence to clear sky and flat surfaces can be used to fit the mispointing error provided by the expression (3.1). Because of the numerous number of good calibration points (i.e. "flat" surfaces in clear sky with good PNR) expected to be available in different scans this method will constrain mispointing errors down to less than 0.2 m s^{-1} within few turns.

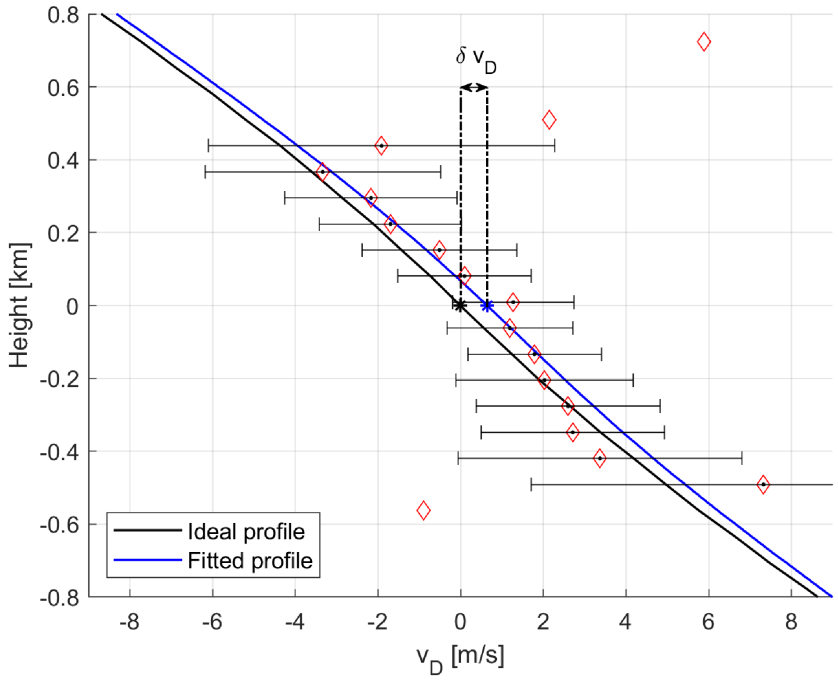

Fig. 3.2.5: *A Doppler velocity profile of the surface simulated for WIVERN observations in the forward direction. The black line represents the ideal Doppler velocity profile without the noise. The red diamonds are the points of the noisy Doppler velocity profile that are oversampled by the radar (one point every 100 m along LoS). The black dots identify the points of the noisy profile with reflectivities above the detection level. Such points are fitted with the shape of the surface return in order to produce the blue line. The Doppler velocities represented by the blue line are the ones retrievable from the radar measurements and they differ from the ideal velocities due to the presence of the noise. δv_D is the velocity shift in correspondence to the surface induced by the noise in the retrieved profile.*

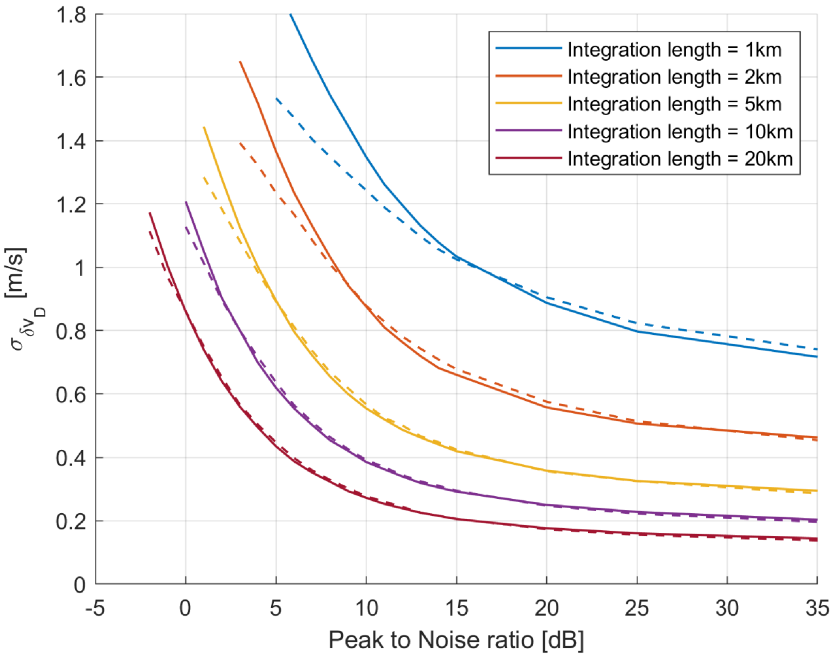

Fig. 3.2.6: *Doppler velocity uncertainty associated with the surface Doppler technique for forward pointing (i.e. azimuthal angle = 0°, solid lines) and side pointing (i.e. azimuthal angle = ±90°, dashed lines) (but similar results are found for any azimuthal angle). The standard deviations of δv_D is plotted as a function of the PNR for different integration lengths as indicated in the legend. The variability of δv_D decreases as thePNR and/or the integration length increase. The mean values of δv_D are negligible for every PNR and every integration length here analysed (not shown). The curves are drawn only for PNRs high enough that more than 80 % of the profiles satisfy the surface detection criterion. See text for details.*

Flat surface approximation

The ASTER global digital elevation model (DEM) (https://asterweb.jpl.nasa.gov/GDEM.asp), with a resolution of $1'' \times 1''$ (i.e. 30.9 m $\times$ 30.9 m at the equator), has been used to examine the validity of the flat surface assumption by evaluating the variability of the elevation in areas comparable to that swept by the WIVERN radar footprint with different integration lengths. Boxes with latitudinal extent of $18''$ and longitudinal extents of $18''$, $36''$, $72''$, $90''$, and $180''$ were considered, which corresponds roughly to from no integration to 5 km integration length. The standard deviations of the elevation, σ_{elev}, within each box were then calculated for the entire global data set. Fig. 3.2.7 shows the variation of the cumulative land fraction with σ_{elev}, for the five box sizes adopted. The respective values of σ_{elev} for increasing box size, given in the form (50^{th} percentile, 70^{th} percentile, 90^{th} percentile), are (7.0 m, 12.0 m, 37.3 m), (8.0 m, 14.4 m, 47.1 m), (9.4 m, 17.9 m, 59.5 m), (10.0 m, 19.2 m, 63.5 m), and (12.0 m, 23.6 m, 74.9 m). It is clear that, for a given percentile, the value of σ_{elev} increases as the box size increases. These findings suggest that roughly half of the land surfaces have a variability in elevation less than 10 m within characteristic WIVERN averaging areas. Such surfaces will likely be useful for the calibration methods I-II (Sects. 3.2.1-3.2.2),

but a dedicated study to properly assess the impact of surface elevation variability is needed.

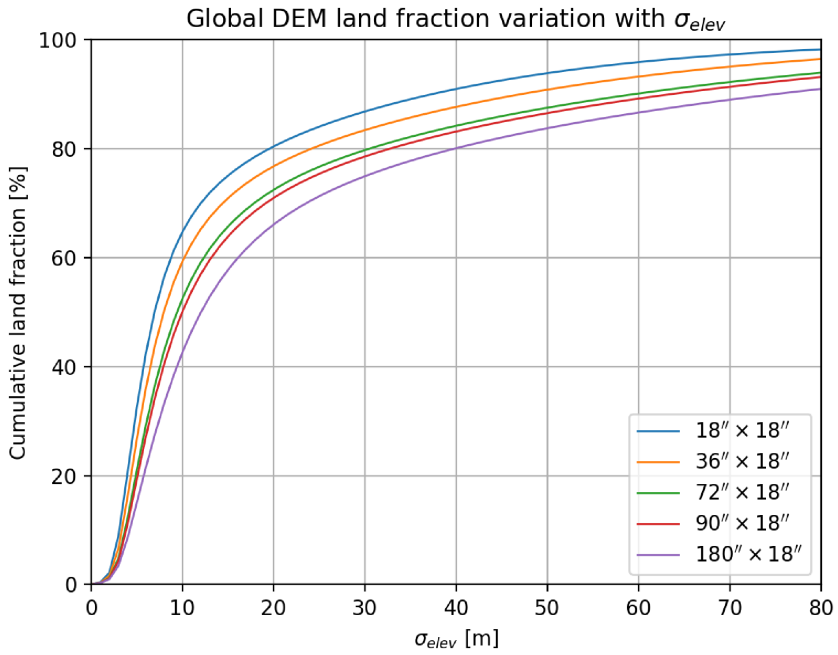

Fig. 3.2.7: *Variation of the cumulative land fraction from the ASTER global DEM with σ_{elev} for different latitude/longitude box sizes. Each coloured line corresponds to a particular longitude × latitude box size (indicated in the legend).*

A final consideration: generally, ocean surfaces will not appear to have zero Doppler velocities but they will have biases of the order of less than 1 m s^{-1}. This is due to the interplay between waves and currents (Chapron et al., 2005; Ardhuin et al., 2019). Here it is assumed that corrections for such effects can be performed based on auxiliary information or that they will average out when considering views from different directions.

3.2.3 Correction method III: active radar calibrator technique

The use of ARC is well established for external calibration of SAR instruments. It has been applied for calibrating the TRMM and GPM radars as well (Masaki et al., 2022).

Here we only consider the use of the ARC in receiver mode with extremely high sampling resolution ($\leq$ 0.1μs). Like in Masaki et al. (2022) we assume the ARC beamwidth of the order of 20°, thus much larger than WIVERN beamwidth. Then, in correspondence of an overpass, if the ARC is pointed toward the satellite, the power received by the ARC at the sampling time t_k, $P_{ARC}(t_k)$, is effectively determined only by the WIVERN Tx antenna pattern. Typically, the signal at the ARC will be detectable for few tenth of milliseconds (see right panels in Fig. 3.2.8). Since the velocity of the spacecraft is very low with respect to the scanning velocity of the radar, its effect on the relative motion of the ARC inside the antenna pattern is negligible. Thus, all the

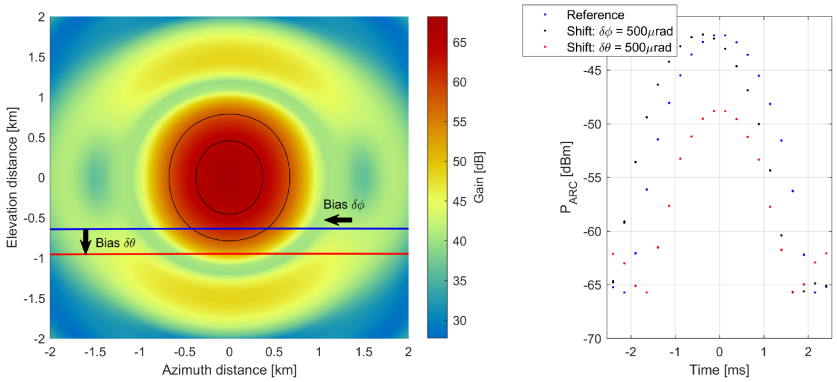

Fig. 3.2.8: *Left panel: example of how the ARC position (expressed in terms of distances at the ground) moves inside the WIVERN antenna pattern when a bias in elevation or in azimuth of 500 μrad is introduced. The satellite is located along the negative y-axis with the antenna pointing forward in the y-direction. The blue line is the position of the ARC for a scanning with a minimum distance between ARC and boresight position of 635 m (reference). The red is the same scan shifted by 500 μrad in elevation bringing the minimum distance between the ARC and the antenna boresight position to 950 m. Black dashed lines correspond to the contour levels of the antenna gain 3 and 10 dB below the maximum gain. Right figure: the ARC received power for the reference (blue) and the scans shifted by 500 μrad in elevation (red) and in azimuth (black). The power received is sampled every 0.1 μs; 3.3μs pulses are transmitted by the radar every 250 μs.*

possible trajectory of the ARC inside the pattern always look like a slightly bent line extended along the azimuth distance (left panel in Fig. 3.2.8).

Note that the radar receiver chain can also be tested by using the radar as an active calibrator (e.g. by sending back to the radar a copy of the signal received by the ARC). With this technique the power received at the WIVERN receiver will depend on the product of the antenna gain in receiving and transmitting mode and thus will have a higher sensitivity than the method discussed next.

The geo-location of the ARC, the position of the spacecraft, the propagation time of the signal and the time at which the space-borne radar send the pulses are assumed to be perfectly known. Uncertainty in the knowledge of those factors affects uncertainty in the mispointing error detection and in the Doppler velocity correction achieved with the ARC technique.

Elevation mispointing

As illustrated in Fig. 3.2.8, an elevation mispointing bias moves the apparent motion of the ARC position inside the WIVERN antenna pattern along the elevation direction (y-axis), e.g. from the blue to the red line. Note that uncertainties in the atmospheric refraction between different models (Mangum and Wallace, 2015) are expected to be of the order of 1 arsec (i.e. lower than 5 μrad) and are therefore neglected in this study. Correspondingly, the actual power measured by the ARC, derived by using Friis formula with an ARC gain of 20 dB, changes because of the difference in the antenna pattern. Such change depends on the specific position of the overpass (e.g. on the minimum distance of the boresight position to the ARC) and on the details of

the antenna pattern. In order to simulate the capability of the ARC measurement to identify and quantify the mispointing, different possible boresight ground tracks have been simulated (like the blue and the red lines in the left panel of Fig. 3.2.8). For each ARC position at a given elevation distance $\bar{\theta}$, the ARC signal is simulated and compared with the returns sampled at different elevation distances $\bar{\theta} + \Delta\theta$ (with a maximum shift $\Delta\theta$ of ± 1000 μrad and sampled every 5 μrad).

The Mean Squared Distance (MSD) of simulated ARC received signals at position $\bar{\theta}$ and $\bar{\theta} + \Delta\theta$ sampled at different time t_k with $k = 1, \ldots, N_t$ is computed as:

$$MSD(\bar{\theta},\, \bar{\theta} + \Delta\theta) = \frac{\sqrt{\sum_{k=1}^{N_t} \left(P_{ARC}^{\bar{\theta}}(t_k) - P_{ARC}^{\bar{\theta}+\Delta\theta}(t_k) \right)^2}}{N_t}, \qquad (3.3)$$

$$\text{with } -1000\,\mu rad \leq \Delta\theta \leq 1000\,\mu rad$$

All power signals below -80 dBm in the summation have been excluded in order to make sure there will be no effective impact from ARC receiver noise. A (0.5) 1 dB noisiness is introduced in the antenna pattern to account for uncertainties in the antenna pattern. 400 different realizations of the antenna pattern are used to compute the MSD in Eq. (3.3) so that a distribution of MSD can be derived for each pair $(\bar{\theta},\, \bar{\theta} + \Delta\theta)$.

The almost symmetric shape of the antenna pattern causes the similarity between two signals sampled at opposite elevation angles with respect to the boresight (i.e. with $\bar{\theta} = \pm\Delta\theta$). Two examples of the 50th (line) and 5-95th percentiles (shading) of the MSD pdfs are shown in Fig. 3.2.9 for $\bar{\theta} = 160$ μrad (left) and $\bar{\theta} = 480$ μrad (right). As expected, the minimum is found in correspondence of a shift between the pairs $\Delta\theta$ equal to 0 μrad but the interplay between the width of the pdf and the prominence of the local minimum introduces uncertainties in the determination of the mispointing.

When considering an overpass close to the ARC (e.g. $\bar{\theta}$ = 160 μrad, left panel), the same MDSs are encountered on a vast interval of $\Delta\theta$, ranging inside the first antenna main lobe in a symmetric way, i.e. with θ between $-\bar{\theta} - \Delta\bar{\theta}$ and $\bar{\theta} + \Delta\bar{\theta}$ with $\Delta\bar{\theta} = 250\mu$rad for this specific example. When considering ARC positions farther away from the boresight, a second local minimum may form in correspondence of $\Delta\theta = -2 \cdot \bar{\theta}$ (e.g., for $\bar{\theta}$ = 480 μrad, the second local minimum is at around $\Delta\theta$ = -960 μrad, right panel).

Left panel of Fig. 3.2.10 shows the uncertainty in the elevation mispointing determination as a function of the elevation distance of the ARC from the WIVERN antenna boresight. It is determined by computing for which elevation mispointing the upper 95th percentile, corresponding to the minimum of the MSD (level identified by the red line in Fig. 3.2.9), exceeds the lower 5th percentile in the adjacent mispointing angles. The black and the red shading represent the result obtained considering an antenna pattern uncertainty of 0.5 dB and 1.0 dB, respectively. Results show that uncertainty are maximized in correspondence to an overpass of the boresight exactly over the ARC.

Given the fact that there will be multiple overpasses per months (see Fig. 3.2.11), it seems realistic to bring this uncertainty down to less than 50 μrad.

Azimuthal mispointing

On the other hand, a mispointing in azimuth does not move the apparent motion of the ARC position inside the WIVERN antenna pattern (Fig. 3.2.8), but only translates the received power at the ARC in time. The transmission time and flight time of the radar pulses ($\sim$ 2.2 ms) are well known; excess path lengths in the atmosphere are

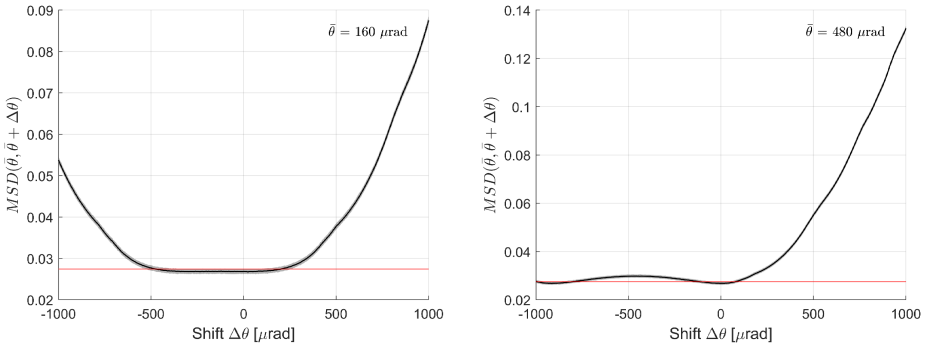

Fig. 3.2.9: *Example of least square distances (the continuous line corresponds to the 50th percentile, while the shading corresponds to the 5th and 95th percentile) for 400 different realizations of the antenna pattern with 1.0 dB of uncertainty as a function of the shift in elevation $\Delta\theta$ for an overpass with antenna boresight passing at $\bar{\theta} = 160$ μrad (left panel) and at $\bar{\theta} = 480$ μrad from the ARC (right panel).*

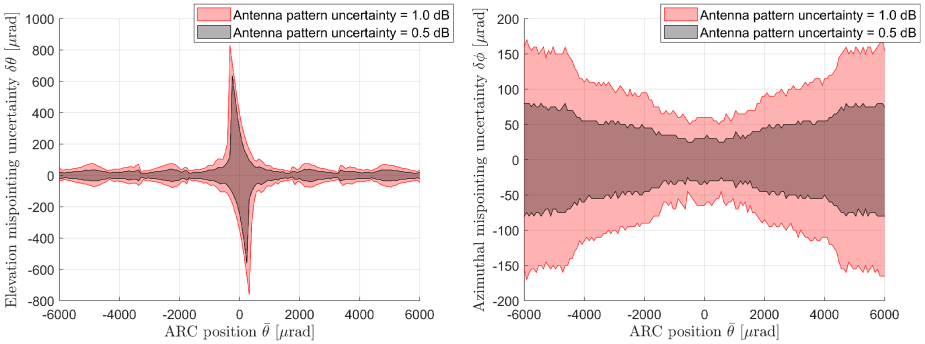

Fig. 3.2.10: *Uncertainty in the elevation (left panel) and azimuthal (right panel) mispointing determination as a function of the minimum ARC elevation distance, $\bar{\theta}$, from the WIVERN antenna boresight. Cases with 0.5 (black) and 1.0 (red) dB uncertainty in the antenna pattern are shown.*

expected to be less than few meters, thus delays are expected to be of the order of less than 0.01 μs, negligible in this context (Mangum and Wallace, 2015). The procedure followed for the elevation mispointing is replicated introducing a shift in azimuth, $\Delta\phi$. In this case

$$MSD(\bar{\theta},\ \Delta\phi) = \frac{\sqrt{\sum_{k=1}^{N_t}\left(P^{\bar{\theta}}_{ARC}(t_k) - P^{\bar{\theta}}_{ARC}(t_k + \Delta\phi/\Omega_a)\right)^2}}{N_t}, \qquad (3.4)$$

$$\text{with } -1000\ \mu rad \leq \Delta\phi \leq 1000\ \mu rad.$$

As before, pdfs of MSD are computed and an estimate of the uncertainty in the azimuthal mispointing is derived based on percentiles. The right panel of Fig. 3.2.10 shows that the closer the overpass is to ARC, the lower is the uncertainty in the azimuthal mispointing determination.

Expected number of useful calibration points as a function of ARC locations

The previous methodology requires the ARC to be positioned in a location within a few km (a few thousand μrad) from the radar boresight location at the ground. To estimate the number of useful calibration points as a function of ARC locations, the WIVERN orbit and boresight positions have been propagated for 50 days. Although the satellite ground track has a repeat cycle of 5 days, the boresight will not trace the same path after this period, thus different regions will be observed within the swath. The simulation rationale consists of selecting a distribution of ARC locations over the region of interest (Fig. 3.2.11a) and counting the number of overpasses within a given footprint. A 1 km spacing in latitude and longitude has been selected to generate the ARCs distribution over the region, whereas a time step of 0.5 ms (equal to 250 m along the scan track) has been selected to guarantee a good sampling of the scan track. The simulation has been repeated considering the footprint corresponding to 1, 3, 5 and 10 times the antenna beamwidth.

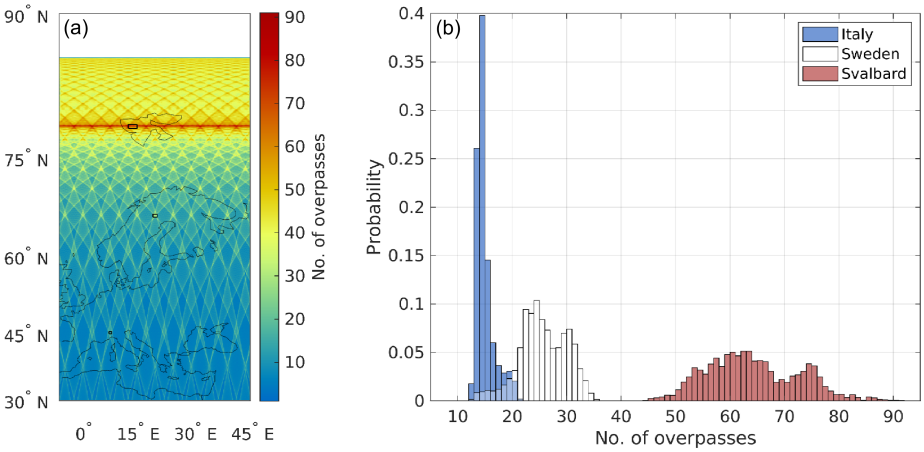

Fig. 3.2.11: *(a) ARCs average number of overpasses within the 10x beamwidth footprint over 10 days. (b) Histogram of the number of overpasses for the selected* $50\times$ *50 km*^{2} *regions (black rectangles in the left figure).*

Fig. 3.2.11 shows the average results for a 10 days period obtained from the 50 days simulation. Panel 3.2.11a displays the number of overpasses over the selected ARCs for a 10x beamwidth footprint. The image shows several hotspots located at specific latitudes and longitudes, while an optimal longitude-independent cluster of hotspots (red line) exists at around 79°of latitude. Since the enhanced number of overpasses at such locations is generated by the intersections occurring at the lower border of the swath, their positions are around 400 km south of the satellite ground track when it reaches its highest latitude. Three 50×50 km^2 regions have been selected around some of the hotspots at latitudes 45°, 66.5°and 78.7°. Panel 3.2.11b shows the histogram of the overpasses within these regions, considering the 10x beamwidth footprint. As expected, a greater number of overpasses occurs when moving towards higher latitudes.

Tab. 3.2.1 summarizes the results when taking different beamwidths. Clearly, when considering the 10x beamwidth footprint (i.e. within roughly 6000 μrad), a sensible number of overpasses (from at least more than 13 at 45°latitude to more than 53 at 78.7°latitude for a 10 days period) is possible over sites whose latitudinal position is

Table 3.2.1: *10th, 50th and 90th percentiles of the overpasses for the three selected regions over 10 days. The results refer to the overpasses within the footprints corresponding to 1, 3, 5 and 10 times the beamwidth.*

	Italy			Sweden			Svalbard		
	10th	50th	90th	10th	50th	90th	10th	50th	90th
1x beamwidth	1	1.4	2	1.4	2.4	3.6	4.6	6.2	8.2
3x beamwidth	3.6	4.4	5.4	5	7.6	10.4	15.2	19	24
5x beamwidth	6.6	7.2	8.6	9	13	16.8	25.9	31.6	39.2
10x beamwidth	13.4	14.4	17.4	20.2	25.2	31.2	53.8	63.2	75.6

properly selected.

3.2.4 Correction method IV: ascending and descending orbit and ECMWF reference technique

During a full rotation, the WIVERN instrument will look at the same LoS for azimuthal angles differing by 180°. In such conditions, Eq. (3.1) predicts that the errors introduced by an azimuthal mispointing will be equal and opposite. But since these are errors on the LoS and the two directions here considered are opposite, it means that the two errors will be identical. Now, for instance, in the part of the orbit closer to the equator, all winds observed at side views (i.e. with $\phi = 90°,\ 270°$ where the impact of the azimuthal mispointing is maximum) roughly correspond to the zonal winds. Then, in presence of an azimuthal mispointing that is changing at frequencies much lower than the orbital frequency (f=1.76×10^{-4}s^{-1}), the ascending and descending orbits will see opposite biases for the zonal winds (but this is true also for winds in any other direction, though the effect will reduce to zero when observing the meridional winds because of the $\sin\phi$ modulation). The advantage of side views is also that at such angle the elevation mispointing is irrelevant (because of the $\cos\phi$ modulation). Therefore, in presence of a mispointing $\delta\phi$, the two pdfs of ascending and descending zonal winds collected at side views will be shifted by $\pm v_{SC}\sin\theta\delta\phi$ (i.e. the relative bias between ascending and descending orbits is about 1 m s^{-1} for $\delta\phi = 100$ μrad).

Statistically, after several orbits the two pdfs are expected to converge to the same pdf under the assumption that the zonal winds at local times differing by 12 h are the same. Is this assumption correct? In this case, any discrepancy between the two pdfs will be a signature of an azimuthal mispointing. But what is the sensitivity of this methodology? i.e. how long is it necessary to average in order to overcome the natural variability and what is the detectable bias for a given time scale?

Alternatively, all HLoS winds can be compared with ECMWF background forecast winds, that have been proved to be unbiased (biases are ≤ 0.3 m s^{-1} in zonal wind and ≤ 0.15 m s^{-1} in meridional winds), have good precision (standard deviations of the order of 2.5 m s^{-1} mostly because of unresolved small scale variability, Rennie (2022)) and have been exploited to correct Aelous wind biases (Weiler et al., 2021). Each WIVERN HLoS wind can be subtracted from the ECMWF reference. If WIVERN quality controlled winds are unbiased, then the distribution of the difference should have zero mean; otherwise, the bias could be estimated with an error which will be equal to $\sigma_{WIVERN-ECMWF}/\sqrt{N_{winds}}$ where $\sigma_{WIVERN-ECMWF}$ is the standard deviation of the distribution of the differences and N_{winds} is the number of independent

winds.

CloudSat-based analysis

To address these questions the dataset produced in Tridon et al. (2023) that combines the CloudSat reflectivity observations and the ECMWF winds has been exploited. Since CloudSat is orbiting in a sun-synchronous polar orbit like the one foreseen for WIVERN, the winds sampled in the ascending and descending orbits have the same statistical variability expected for WIVERN.

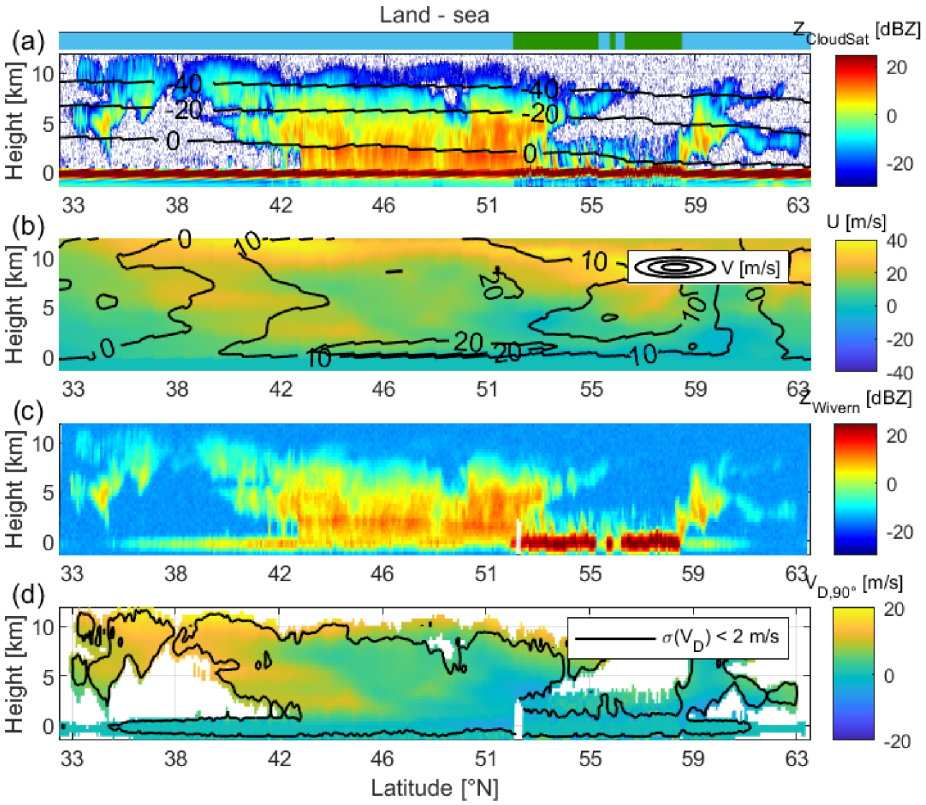

Fig. 3.2.12: *(a) CloudSat reflectivity of a frontal system over East Atlantic and British Isles, and ECMWF temperature contours. (b) Corresponding zonal (colors) and meridional (contours) ECMWF winds. (c) Simulated WIVERN reflectivity at 10 km resolution. (d) Simulated side-view WIVERN Doppler velocity at 10 km resolution with a contour showing areas with an accuracy associated to the radar estimator better than 2 m* s^{-1}.

Figure 3.2.12 shows an example of simulation of WIVERN measurements from a portion of CloudSat orbit through a North-Eastern Atlantic widespread low which brought a significant amount of precipitation and high winds over Ireland on the 19^{th} February 2007. The CloudSat reflectivity curtain (panel 3.2.12a) is combined with the corresponding ECMWF wind reanalysis (panel 3.2.12b) to simulate the slant reflectivity (panel 3.2.12c) and Doppler velocity (panel 3.2.12d) curtains that would be observed by WIVERN at side-view ($\phi = 90°$). Because of the slant incidence angle,

the WIVERN surface reflectivity is much lower than that of CloudSat apart from over land (see land/sea flag at the top of panel a). In panel 3.2.12d, the black contour highlights the areas where the WIVERN Doppler velocity accuracy would be better than 2 m s^{-1}.

Our method follows the following steps:

1. the dataset has been divided in ascending (A) and descending (D) orbits for latitudes between -65° and 65°;

2. histograms of WIVERN LoS winds when looking sideways to the right/left of satellite in A/D orbits (roughly corresponding to zonal winds) have been accumulated at different heights; only winds where clouds are present and produce an SNR larger than -4 dB have been considered; random noise is added to each observation according to the expected error computed from the radar simulator (formula 16 in Battaglia et al. (2022)) for integration lengths of 10 km.

3. ensemble of pdfs of WIVERN "zonal winds" are produced for different integration periods.

4. Jensen-Shannon distances (like in Battaglia et al. (2023)) between ascending and descending pdfs computed in 3 and for A/D pdfs shifted by different wind biases (e.g. ± 2 m s^{-1} corresponding to azimuth biases of 400 μrad).

5. threshold values expressed in terms of integration time or number of measured winds where different bias levels become detectable for 4. are computed (like in Battaglia et al. (2023)).

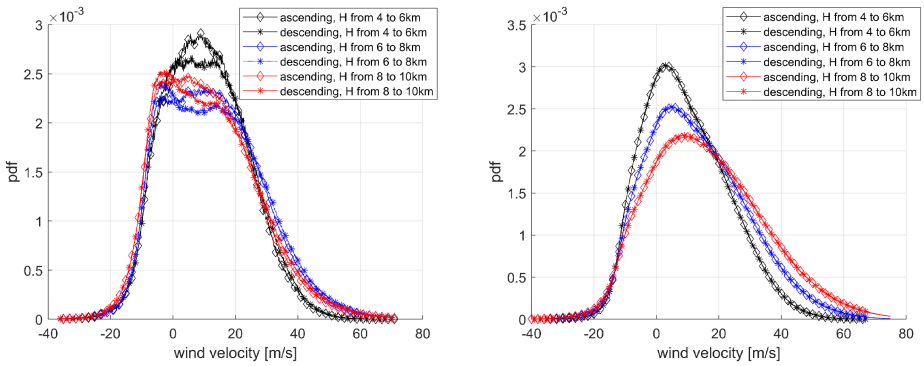

Fig. 3.2.13: *Pdfs of A (diamond marker) and D (star "*" marker) in-cloud horizontal winds retrieved by WIVERN when looking sideways (left panel) and all-sky conditions horizontal winds at WIVERN side view (right panel). In the left panel, only points characterized by a Doppler velocity accuracy better than 4 m s^{-1} are considered. The histograms have been generated with points sampled at latitudes within $\pm 65°$ and at different altitude intervals, as indicated in the legend. The pdfs have been generated with 270 (in-cloud winds) and 365 (all-sky winds) days of data.*

Pdfs of in-cloud horizontal winds retrieved by WIVERN when looking sideways are shown in the left panel of Fig. 3.2.13 for A/D orbits (diamond/star markers) and for different height ranges as indicated in the legend. The same plot is repeated on the right

hand side considering all-sky condition winds. In the latter condition, A and D wind distributions looks pretty much identical. However, when considering only in-cloud winds, the two distributions take different shapes, suggesting the existence of a diurnal cycle (A and D winds are sampled twelve hours apart) affecting in-cloud winds. This result makes the option of identifying azimuthal mispointing only by using WIVERN ascending and descending measurements challenging because the pdfs of A/D in-cloud winds are intrinsically different and therefore large biases in the winds (typically of the order of 1 m s^{-1}, i.e. $\phi \approx 200\mu$rad) are needed to see a neat separation between the two pdfs for accumulation times of at least 10-15 days (not shown).

On the other hand, when considering the ECMWF as a reference, Fig. 3.2.14 demonstrates that the histogram of the differences for the side winds has a standard deviation of the order of 3.66 m s^{-1} with an average of about 80,000 winds per day. In this case, only WIVERN's wind measurements characterized by a SNR higher than 0 dB have been taken into account. Because of this large amount of winds, this demonstrates that the error on the estimate of the azimuthal bias will become negligible ($\leq$ 0.2m s^{-1}) already after few minutes. The real limit becomes in this case the assumption that the reference ECMWF winds are unbiased. The validity of such assumption applies on global averages over few days with an upper limit for the bias of circa 0.3 m s^{-1}. Note that the same reasoning can be applied to the forward/backward line of sight winds and therefore to the elevation biases.

3.3 SUMMARY AND CONCLUSIONS

Different methodologies for correcting mispointing errors in conically scanning Doppler velocity measurements (with focus at the WIVERN configuration, currently under study as one of the Earth Explorer 11 candidate missions) have been discussed. Results show that:

- The use of radar in "altimeter" mode is very robust for identifying elevation mispointing on very short time scales (few ms). Depending on the surface peak strength and the integration length, different levels of correction can be achieved; e.g. with a 10 dB peak to noise ratio less than 20 μrad (50 μrad) can be achieved at 10 km (2 km) integration length. This value corresponds to velocity errors smaller than 0.12 m s^{-1} (0.28 m s^{-1}). The methodology is limited by the flat surface assumption and by the absence of low atmospheric targets that may contaminate the surface signal. Proper screening to identify these situations must be performed before hand.

- The surface Doppler velocity profile can be used for correcting both elevation and azimuthal mispointing but with generally worse performances than the previous method. With a 10 dB surface peak to noise ratio errors of 0.4 m s^{-1} (0.9 m s^{-1}) can be achieved at 10 km (2 km) integration length. The method is likely to produce accurate pointing corrections when making use of the clear sky, high peak to noise ratio flat surfaces encountered across several antenna rotations. Limitations similar to the previous method apply in this instance; additionally, for ocean surfaces, the potential bias introduced to the Doppler velocity by waves and currents must be accounted for.

- The use of an ARC is effective in identifying slowly changing mispointing errors (biases) larger than about 50 μrad when considering multiple overpasses over week-long periods with the error mainly driven by the knowledge of the details

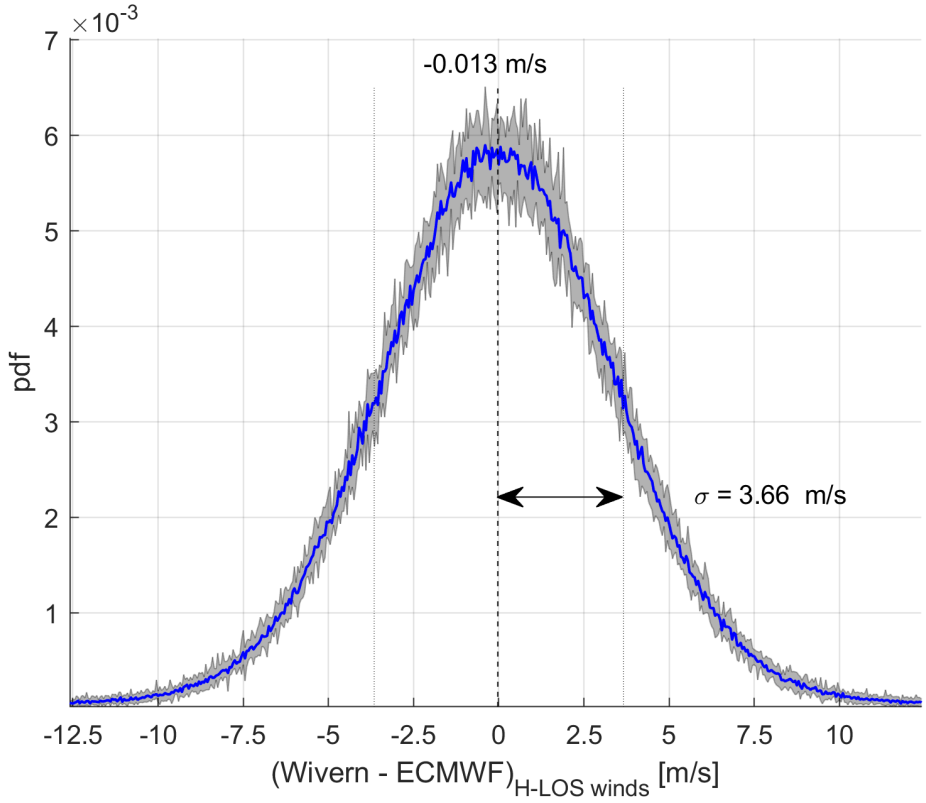

Fig. 3.2.14: *Pdf of the difference between the winds retrieved by WIVERN (LoS) at side view and the ECMWF winds. The pdf have been generated with 801,474 points, all with an SNR larger than 0 dB, collected during a period of 10 days (blue line). The envelope of the one day pdfs collected in each of those 10 days is also shown (gray shading).*

of the antenna pattern. The location of the ARC can be optimally chosen based on the orbit details, with the goal of maximizing the number of overpasses.

- Winds measured by WIVERN in ascending and descending orbits can be used to detect azimuthal biases but only for large biases (of the order of 200 μrad) on time scale longer than 10 days. On the other hand, because of the huge number of WIVERN winds measurements collected every day, the comparison of the Level 2 WIVERN HLoS wind to a state-of-the-art data assimilation system and forecast model like provided by ECMWF via the so-called O-B (observation - background) technique is extremely effective in determining biases. The method is practically only limited by time and spatial scales at which the reference model can be considered unbiased.

Future work should address the impact of the instrument footprint variability of the surface σ_0 (e.g. due to differential attenuation or by surface height variability) for methodology 1 and 2. The impact of waves and currents on the Doppler velocity measurements should also be established at this high frequency and at slant incidence angles.

3.A EFFECT OF A SCAN-AXIS MOUNTING OFFSET

In general, the effect of a scan-axis mounting offset can be considered as well. Let A_{roll}, A_{pitch}, A_{yaw} be the roll, pitch and yaw angles, respectively, which characterize the scan-axis mounting offset. We can assume that these angles are constant in time. The offset will generate a bias in the elevation and azimuthal angles with respect to the case where no offset is present; the mispointing in elevation and azimuthal will be time-dependent with harmonics of the antenna angular velocity, Ω_a, according to:

$$\Delta\theta(t) = -A_{roll}\sin(\Omega_a\, t) + A_{pitch}\cos(\Omega_a\, t) \tag{3.5}$$

$$\Delta\phi(t) = -\frac{\cos(\Omega_a\, t)}{\tan(\theta)}A_{roll} - \frac{\sin(\Omega_a\, t)}{\tan(\theta)}A_{pitch} + A_{yaw} \tag{3.6}$$

The offset angles can be derived as following.

- Since offset in roll and pitch induce Ω_a-harmonic mispointing in elevation, A_{roll} and A_{pitch} can be identified with method #1. The bias in altitude of the surface position, δz, can be averaged over a period long enough in order to cancel out the mispointing in elevation induced by the antenna (effective at higher frequencies). Then, A_{roll} and A_{pitch} can be retrieved from Eq. (3.2) by looking at the δz at forward/backward and side views for A_{roll} and A_{pitch}, respectively.

- A_{yaw} can be handled as a constant azimuthal mispointing, and thus its effect on the Doppler velocity can be corrected adopting method #2.

The assumption that the scan-axis mounting offset is constant is usually valid for errors in the original mounting or by misalignments generated by post-launch conditions. Finally, note that Eqs. (3.5-3.6) allows to convert a generic perturbation in roll, pitch and yaw of the platform (e.g. inherent to the spacecraft attitude control) into a mispointing in the antenna azimuth and elevation.

REFERENCES

Ardhuin, F., Brandt, P., Gaultier, L., Donlon, C., Battaglia, A., Boy, F., Casal, T., Chapron, B., Collard, F., Cravatte, S., Delouis, J.-M., DeWitte, E., Dibarboure, G., Engen, G., Johnsen, H., Lique, C., PacoLopez-Dekker, Maes, C., Martin, A., Mari, L., Menemenlis, D., Nouguier, F., Peureux, C., Rampal, P., Ressler, G., Rio, M.-H., Rommen, B., Shutler, J. D., Suess, M., Tsamados, M., Ubelmann, C., van Sebille, E., van der Vorst, M., and Stammer, D.: SKIM, a candidate satellite mission exploring global ocean currents and waves, Frontiers, 2019.

Battaglia, A. and Kollias, P.: Using ice clouds for mitigating the EarthCARE Doppler radar mispointing, IEEE Transactions on Geoscience and Remote Sensing, 53, 2079–2085, doi: 10.1109/TGRS.2014.2353219, 2014.

Battaglia, A., Wolde, M., D'Adderio, L. P., Nguyen, C., Fois, F., Illingworth, A., and Midthassel, R.: Characterization of Surface Radar Cross Sections at W-Band at Moderate Incidence Angles, IEEE Transactions on Geoscience and Remote Sensing, 55, 3846–3859, 10.1109/TGRS.2017.2682423, 2017.

Battaglia, A., Dhillon, R., and Illingworth, A.: Doppler W-band polarization diversity space-borne radar simulator for wind studies, Atmospheric Measurement Techniques, 11, 5965–5979, https://doi.org/10.5194/amt-11-5965-2018, 2018.

Battaglia, A., Martire, P., Caubet, E., Phalippou, L., Stesina, F., Kollias, P., and Illingworth, A.: Observation error analysis for the WInd VElocity Radar Nephoscope W-band Doppler conically scanning spaceborne radar via end-to-end simulations, Atmospheric Measurement Techniques, 15, 3011–3030, https://doi.org/10.5194/amt-15-3011-2022, 2022.

Battaglia, A., Scarsi, F. E., Mroz, K., and Illingworth, A.: In-orbit cross-calibration of millimeter conically scanning spaceborne radars, Atmospheric Measurement Techniques, 16, 3283–3297, https://doi.org/10.5194/amt-16-3283-2023, 2023.

Chapron, B., Collard, F., and Ardhuin, F.: Direct measurements of ocean surface velocity from space: Interpretation and validation, Journal of Geophysical Research: Oceans, 110, https://doi.org/https://doi.org/10.1029/2004JC002809, 2005.

ESA: WIVERN Report for Assessment, Tech. rep., ESA-EOPSM-WIVE-RP-4375, available at https://eo4society.esa.int/event/earth-explorer-11-user-consultation-meeting/, 2023.

Illingworth, A., Battaglia, A., and Delanoe, J.: WIVERN: An ESA Earth Explorer Concept to Map Global in-Cloud Winds, Precipitation and Cloud Properties, in: 2020 IEEE Radar Conference (RadarConf20), pp. 1–6, https://doi.org/10.1109/RadarConf2043947.2020.9266286, 2020.

Kollias, P., Puidgomènech Treserras, B., Battaglia, A., Borque, P. C., and Tatarevic, A.: Processing reflectivity and Doppler velocity from EarthCARE's cloud-profiling radar: the C-FMR, C-CD and C-APC products, Atmospheric Measurement Techniques, 16, 1901–1914, https://doi.org/10.5194/amt-16-1901-2023, 2023.

Lori, M., Pfeiffer, E. K., Cardoso, C., de Rijk, E., Caubet, E., Battaglia, A., Trenta, D., and van der Vorst, M.: The DORA conical scan antenna, in: 38th ESA Antenna Workshop on Innovative Antenna Systems and Technologies for Future Space Missions 3-6 October 2017, Noordwijk, The Netherlands, 2017.

Mangum, J. G. and Wallace, P.: Atmospheric Refractive Electromagnetic Wave Bending and Propagation Delay, Publications of the Astronomical Society of the Pacific, 127, 74–91, URL http://www.jstor.org/stable/10.1086/679582, 2015.

Masaki, T., Iguchi, T., Kanemaru, K., Furukawa, K., Yoshida, N., Kubota, T., and Oki, R.: Calibration of the Dual-Frequency Precipitation Radar Onboard the Global Precipitation Measurement Core Observatory, IEEE Transactions on Geoscience and Remote Sensing, 60, 1–16, https://doi.org/10.1109/TGRS.2020.3039978, 2022.

Meneghini, R. and Kozu, T.: Spaceborne weather radar, Artech House, 1990.

Rennie, M.: The NWP impact of Aeolus Level-2B winds at ECMWF (v5.0, 10 August 2022), Disc contract technical note, ESA, https://confluence.ecmwf.int/display/AEOL/L2B+team+technical+reports+and+relevant+papers, 2022.

Rizik, A., Battaglia, A., Tridon, F., Scarsi, F. E., Kötsche, A., Kalesse-Los, H., Maahn, M., and Illingworth, A.: Impact of Crosstalk on Reflectivity and Doppler Measurements for the WIVERN Polarization Diversity Doppler Radar, IEEE Transactions on Geoscience and Remote Sensing, 61, 1–14, https://doi.org/10.1109/TGRS.2023.3320287, 2023.

Scarsi, F. E., Battaglia, A., Tridon, F., Martire, P., Dhillon, R., and Illingworth, A.: Mispointing characterization and Doppler velocity correction for the conically scanning WIVERN Doppler radar, Atmospheric Measurement Techniques, 17, 499–514, https://doi.org/10.5194/amt-17-499-2024, 2024.

Tanelli, S., Im, E., Durden, S. L., Facheris, L., Giuli, D., and Smith, E.: Rainfall Doppler velocity measurements from spaceborne radar: overcoming nonuniform beam filling effects, Journal of Atmospheric and Oceanic Technology, 21, 27–44, doi: 10.1175/1520-0426, 2004.

Tridon, F., Battaglia, A., Rizik, A., Scarsi, F. E., and Illingworth, A.: Filling the Gap of Wind Observations Inside Tropical Cyclones, Earth and Space Science, 10, e2023EA003 099, https://doi.org/https://doi.org/10.1029/2023EA003099, e2023EA003099 2023EA003099, 2023.

Weiler, F., Rennie, M., Kanitz, T., Isaksen, L., Checa, E., de Kloe, J., Okunde, N., and Reitebuch, O.: Correction of wind bias for the lidar on board Aeolus using telescope temperatures, Atmospheric Measurement Techniques, 14, 7167–7185, https://doi.org/10.5194/amt-14-7167-2021, 2021.

Wolde, M., Battaglia, A., Nguyen, C., Pazmany, A. L., and Illingworth, A.: Implementation of polarization diversity pulse-pair technique using airborne W-band radar, Atmospheric Measurement Techniques, 12, 253–269, https://doi.org/10.5194/amt-12-253-2019, 2019.

Zrnic, D. S.: Simulation of weatherlike Doppler spectra and signal, J. Appl. Meteorol., 14, 619–620, 1975.

Chapter 4

Improving snowfall sampling in polar regions with the WIVERN conically scanning space-borne W-band radar

This chapter is extensively based on the following publication:
Scarsi et al. (2025), *How to reduce sampling errors in spaceborne cloud radar-based snowfall estimates*; https://doi.org/10.5194/tc-19-4875-2025

4 IMPROVING SNOWFALL SAMPLING IN POLAR REGIONS WITH THE WIVERN CONICALLY SCANNING SPACE-BORNE W-BAND RADAR

The design of the observing geometry and the scanning strategy of a space-borne radar has a strong impact on the measurements and it is dictated by the goals of the mission. A fixed near-nadir looking radar, (e.g. CloudSat and EarthCare CPRs) is a simple system but can only see a vertical cut of an atmospheric system, with a fixed observation geometry. On the other hand, a cross-track scanning geometry (e.g. GPM DPR) or a conically scanning system (e.g. WIVERN), have a much bigger swath and can provide a much higher number of samples. The conically scanning system can reach larger swath and can potentially provide different observing views of the same point. However, introducing a scanning system, whether it is electronic (GPM DPR) or mechanical (WIVERN) increase the overall complication of the system. In particular, a conically scanning radar, like the one of WIVERN, aims at having a larger swath width thanks to the scanning geometry, being able to observe full atmospheric systems and how they interact with the surrounding environment (Tridon et al., 2023). The resulting larger number of collected samples is also expected to reduce the uncertainty in climatologies and can be used to effectively evaluate climate models. For example, left panel in Fig. 4.0.1 shows the radar reflectivity CFAD sampled in a $2.5^\circ \times 2.5^\circ$ latitude-longitude area over the pacific ocean and north-east to Australia. The CFAD is derived from ICON and refers to a period of one month. Central and right-hand panel show the departure of the CFAD sampled by a CloudSat-like near-nadir looking radar and a WIVERN-like conically scanning radar from their respective CFAD of reference. This suggests that the larger number of samples collected by WIVERN reduce the uncertainty in climatologies, and makes them converge in shorter times.

This chapter is an edited version of Scarsi et al. (2025) and evaluates the performance of a WIVERN-like conically scanning radar in the sampling of the polar snowfall. The study can extended to any other geophysical quantity. The assessment of the performance on the snowfall has been chosen as it is a quantity essential for the estimation the ice-sheet mass balance in the polar region. The chapter also estimate the impact of the sampling on the snowfall climatologies at different temporal and spatial scales, and compares the results with the performance of a traditional CloudSat-like nadir looking radar.

In polar regions and mid-latitudes, most precipitation is formed through the ice phase as snowfall (Mülmenstädt et al., 2015). For high latitudes and mountainous regions, it is the dominating form of precipitation at the ground (Field and Heymsfield, 2015). Therefore, snowfall not only removes moisture form the atmosphere but plays a crucial, interlinking role in the climate system. In the cryosphere, snowfall is the only mass source term for glaciers and ice sheets, and thus crucial for their mass balance

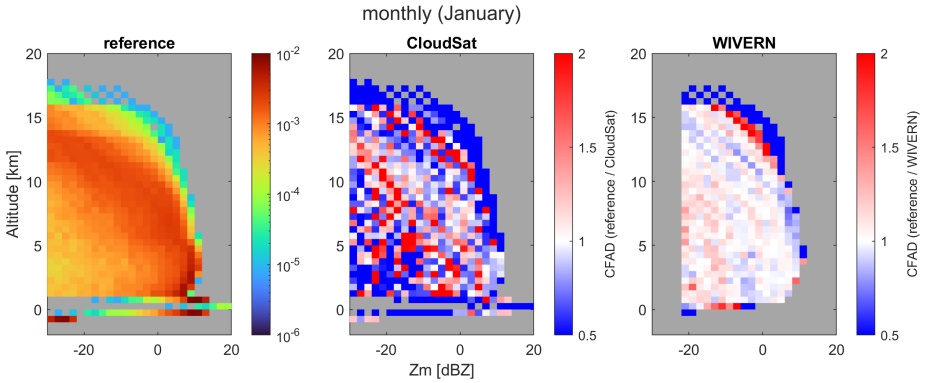

Fig. 4.0.1: *Left-hand side panel: 1-month (January) CFAD computed by ICON model 2.5° × 2.5° latitude-longitude area over the Pacific Ocean as seen by a nadir viewing geometry; it is used as a reference to compute the uncertainty in the CFAD sampled by CloudSat. Central panel: Ratio between the CFAD sampled by CloudSat and the CFAD of reference for a nadir viewing geometry (shown in the left panel).*
Right-hand side panel: Ratio between the CFAD sampled by WIVERN and the CFAD of reference for a 41° incidence angle viewing geometry (not shown).

(Souverijns et al., 2018a). On sea ice, snow forms an insulating layer between sea ice and atmosphere impacting sea ice lifetime (Perovich et al., 2017). On land, snow modifies the surface albedo relevant for the ice albedo feedback (Hall, 2004). Furthermore, snow cover impacts ecology (Slatyer et al., 2022), traffic safety (Strong et al., 2010), recreation (Steiger et al., 2019), and freshwater storage which is also relevant for hydropower generation (Wasti et al., 2022). In a warming climate, precipitation amounts and extreme events, including heavy snowfall, are expected to increase (Quante et al., 2021), but the estimates of the exact magnitudes are affected by large uncertainties (Lopez-Cantu et al., 2020). This is because the exact pathways through which ice particles, liquid water, cloud dynamics, and aerosol particles are interacting during snow formation are not well understood (Morrison et al., 2012; Griesche et al., 2021).

Better observations of the fingerprints of snowfall formation processes at sufficient spatio-temporal resolution are needed to advance our understanding of ice and mixed-phase clouds and precipitation formation processes (Morrison et al., 2020). Traditionally, snowfall is measured with in situ gauges, but high spatial variability (Scipión et al., 2013), poor coverage (Kidd et al., 2017), and wind-related under-catch (Yang et al., 1999) pose significant challenges.

The deficits of in situ snowfall observations requires using remote sensing techniques. Because ground-based remote sensing with weather radar is available only in densely populated areas and few sites are equipped with radars in the polar regions (e.g., Matrosov et al. (2008); Souverijns et al. (2018b); Li et al. (2021); Schoger et al. (2021); Matrosov et al. (2022); Tridon et al. (2022); Alexander et al. (2023)) space-borne remote sensing techniques are the prime method to observe snowfall globally. Passive microwave sensors such as AMSU (Advanced Microwave Sounding Unit) offer good spatial coverage due to their km-scale imaging capabilities, but passive microwave signals are also impacted by surface properties (Chen and Staelin, 2003; Skofronick-Jackson et al., 2004; Skofronick-Jackson and Johnson, 2011) and the presence of supercooled liquid water (Wang et al., 2013; Battaglia and Panegrossi, 2020; Panegrossi et al., 2022) which are difficult to separate from atmospheric scattering con-

tributions by frozen hydrometeors.

Due to their unique profiling capabilities, radar can provide profile properties of hydrometeors and separate scattering by hydrometeors from the surface. Even though the conversion into snowfall rates is associated with uncertainties related to the indirect observation, space-borne radars on low orbit satellites such as CloudSat (Stephens et al., 2002) and EarthCARE (Wehr et al., 2023) provide the best way to observe snowfall globally (Milani and Kidd, 2023). CloudSat snowfall measurements have been successfully evaluated with ground based in situ (Hiley et al., 2011) and ground based radar networks (Smalley et al., 2014; Mroz et al., 2021). The data has been used to produce snowfall climatologies (Liu, 2008; Palerme et al., 2014; Stephens et al., 2018; Bennartz et al., 2019; Kulie et al., 2020) which are most relevant in regions with sparse in situ observations such as Antarctica or Greenland. Further, CloudSat data was used to study seasonal cycles (Kulie and Milani, 2018), evaluate climate models (Palerme et al., 2017), and to study the surface mass balance of ice sheets (Boening et al., 2012; Milani et al., 2018). However, the combination of CloudSat's revisit time of 16 days combined with the 1 km footprint of the observations leads to a sparse spatial sampling, causing noise in snowfall climatologies even when averaging over 10 years (Kulie et al., 2020). Further, it was found that CloudSat's snowfall retrieval has biases for snowfall rates exceeding 1.0 mm h^{-1} (Cao et al., 2014). Due to surface clutter contamination, CloudSat cannot observe snowfall in the blind zone which is up to 1200 m thick and can lead to an underestimation of snowfall rate for shallow events but also to an overestimation of snowfall rate due to sublimation (Maahn et al., 2014).

In this study, we will show the potential of the ESA Earth Explorer 11 candidate mission WIVERN global snowfall monitoring. Different to CloudSat and EarthCare, WIVERN's cloud radar will not measure at nadir but will scan conically at 38° off-nadir angle (for measuring horizontal in-cloud wind) and also features a 94 GHz passive channel. WIVERN will be characterize by a smaller blind zone over ice-free ocean (Coppola et al., 2025) and has the potential for improved snowfall retrievals due to the availability of a passive channel (Battaglia and Panegrossi, 2020). However, over land and sea ice, WIVERN's blind zone is anticipated to be larger than that of CloudSat, potentially limiting its capability to observe shallow snowfall precipitation events. This work will focus on how the conical scanning, with 70 times better coverage than for a nadir pointing instrument such as CloudSat or EarthCARE, improves snowfall estimates. The analysis is based on three main assumptions:

- Blind Zone Effect: The impact of the blind zone is related to the snowfall regime. With shallow snowfall being the most common, significant number of snowfall events occur below CloudSat's blind zone (Shates et al., 2025). While WIVERN's surface snowfall retrieval performance would improve over ice-free oceans compared to CloudSat due to reduced blind zone effects, it would decrease over land and sea ice. The blind zone effect is not accounted for in the current snowfall estimate analysis. However, the resulting impact on estimates are examined in Section 4.3. Coppola et al. (2025) provides a detailed discussion on the hydrometeor detection near the Earth's surface in WIVERN and CloudSat measurements.

- Z-S Relationship Assumption: The Z-S relationship is assumed to be unbiased. In practice, the Z-S is typically application dependent.

- Attenuation is neglected and its contribution is expected to reduce the SNR at very high snowfall rates. Also, it is expected to be larger for WIVERN due to its

slant observation geometry.

WIVERN and the methodology are introduced in Section 4.1, results are presented in Section 4.2, the ground clutter impact on surface snow precipitation is discussed in Section 4.3, and concluding remarks are given in Section 4.4.

4.1 METHODOLOGY

Table 4.1.1: *CloudSat (Stephens et al., 2002) orbit and radar specifics.*

Spacecraft height, H_{SC}	705 km
Spacecraft velocity, v_{SC}	7600 m s^{-1}
Orbit inclination, i	98.2°
Orbit Local Time of the ascending node, LTAN	13:45
Orbit repeat cycle	16 days
Off-nadir pointing angle	0.16°
Swath width at ground	1.4 km
Radar output frequency	94.00 GHz
Radiometer channel	-
Antenna angular velocity, Ω_a	–
Footprint speed	7 km s^{-1}
Minimum detectable reflectivity	-28 dBZ

The basis for this work is the ERA 5 hourly surface snowfall (water equivalent) reanalysis product (Hersbach et al., 2023a, last access: 15 March 2024), as it is considered to have realistic spatio-temporal snow fields (Kouki et al., 2023). The ERA5 snowfall dataset that have been used in the analysis has a spatial resolution of $0.25° \times 0.25°$ and covers a total time span of 20 years from 2001 to 2020. We use it as a benchmark to compare the accumulated snowfall retrieved by WIVERN-like and CloudSat-like radar instruments, both simulated with the same ERA5 dataset. The sampling of the radar footprints have been computed based on the viewing geometries and the satellite orbits (see Tab. 1.3.1 for WIVERN's specs, and Tab. 4.1.1 for CloudSat's specs), which have been propagated in the period of interest according to the orbital parameters. Then, for each time stamp of the selected ERA5 dataset, a mask that indicates whether any given geolocated snowfall dataset $0.25° \times 0.25°$ grid point is sampled by the instrument is generated according to the radar footprints positions at ground. With a conically scanning radar, several passes over the same grid point may occur within minutes, but several passes within an hour is counted as one.

The mask has been applied to the ERA5 snowfall dataset to produce two datasets, with the snowfall simulated as observed by the CloudSat and WIVERN instruments using the following procedure. The hourly ERA5 snowfall, S, is converted to the equivalent radar reflectivity factor z_e according to a mean climatological relationship as proposed by Hiley et al. (2011) through

$$z_e = a_{mean} S^{b_{mean}} \qquad a_{mean} = 21.6, \quad b_{mean} = 1.2 \tag{4.1}$$

with z_e in mm^6 $m-3$. Typically, reflectivity is used in logarithmic units dBZ converted with $Z_e = 10 \times \log_{10} z_e$. The reflectivity below the nominal radar sensitivity (-21 dBZ and -28 dBZ for WIVERN and CloudSat, respectively) is set to 0 mm^6 $m-3$, as below

these thresholds, no snow precipitation is expected to be detected. The Z_e values are converted to snowfall rate by introducing random noise associated with the uncertainty in the $Z_e - S$ relationship. For this, Z, in dBZ, is assumed to be normally distributed. Consequently, S is sampled from a log-normal distribution, whose mean value corresponds to the ERA5 value and whose standard deviations are computed as half the difference $S_{1\sigma} - S_{-1\sigma}$ where $S_{1\sigma}$ and $S_{-1\sigma}$ are assumed equal to:

1. $S_{+1\sigma} = 0.0238\ z_e^{0.909}$;
2. $S_{-1\sigma} = 0.21\ z_e^{0.769}$.

which are the inverse formulas of $z_e = 61.2\ S^{1.1}$ and $z_e = 7.6\ S^{1.3}$, respectively, proposed by Hiley et al. (2011) as lower and upper boundaries for the uncertainty in the $Z_e - S$ relationship. This represents a worst-case estimate of the uncertainty caused by the $Z_e - S$ relationship, as we assume it varies randomly from grid box to grid box, whereas in reality it may be spatially correlated. Here, we neglect errors related to the fact that S is not observed at the surface, but at an higher altitude due to the surface clutter (1200 m for CloudSat, Maahn et al., 2014). Also note that, typically, Z-S relationships cannot be unbiased for every regime, application and context. For instance, Hiley's distributions are derived for specific regimes (e.g., no riming). Therefore, outside those regimes, (e.g., in presence of riming, presence of supercooled particles, presence of other particles shapes) other sources of uncertainty might exist.

Fig. 4.1.1 shows an example case of geo-located ERA5 snowfall rate (January 2, 2020 18:00 UTC) in comparison to the corresponding simulated WIVERN and CloudSat retrievals. Despite its sparse sampling within its 800 km swath, the WIVERN footprint samples all 0.25° grid points within the swath, with an obvious benefit compared with the CloudSat nadir observations.

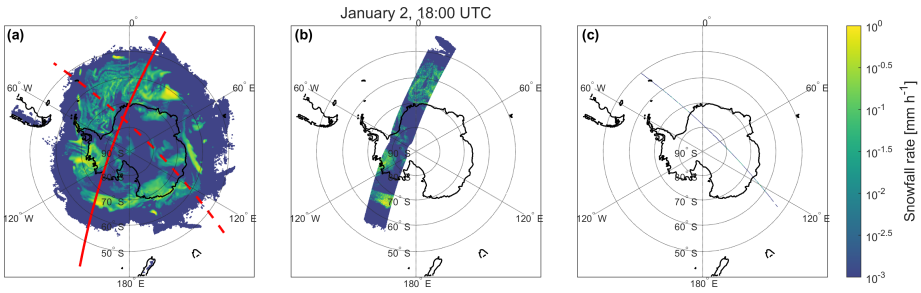

Fig. 4.1.1: *Example of a geo-located WIVERN and CloudSat snowfall rate retrieval obtained at a given hour. Panel (a) shows the geo-located ERA5 accumulated snowfall rate at January 2, 2020 at 18:00 UTC, with the satellites' ground-track of WIVERN and CloudSat ground-track outlined with the solid and dashed red lines, respectively. Panels (b) and (c) depict what would be the corresponding snowfall rate retrieval of WIVERN and CloudSat, respectively. Uncertainty due to application of the $Z_e - S$ relationship has been included.*

Finally, the snowfall retrieved in each $0.25° \times 0.25°$ grid-box is aggregated at different time scales (e.g., a month, a year). The results can then be further aggregated over coarser spatial domains.

The simulated snowfall retrievals from the satellites are compared with the ERA5 reference dataset to assess the reliability of the WIVERN (S_{WIV}) and CloudSat (S_{CS}) data for estimating snowfall accumulation at different spatial and temporal scales.

For each investigated spatial and temporal resolution, time series data is accumulated for a total of 20 years. From the three time series of S_{ERA5}, S_{WIV} and S_{CS}, the bias ($AB_{WIV/CS}$) the root mean square error ($RMSE_{WIV/CS}$) and their normalized counterparts ($NAB_{WIV/CS}$, $NRMSE_{WIV/CS}$) are estimated with

$$AB_{WIV/CS} = \frac{1}{N}\sum_{i=1}^{N}\left|S_{WIV/CS}[i] - S_{ERA5}[i]\right| \tag{4.2}$$

$$NAB_{WIV/CS} = \sum_{i=1}^{N}\left(\left|S_{WIV/CS}[i] - S_{ERA5}[i]\right| / \sum_{i=1}^{N} S_{ERA5}[i]\right. \tag{4.3}$$

$$RMSE_{WIV/CS} = \sqrt{\frac{1}{N}\sum_{i=1}^{N}\left(S_{WIV/CS}[i] - S_{ERA5}[i]\right)^2} \tag{4.4}$$

$$NRMSE_{WIV/CS} = \sqrt{\frac{\sum_{i=1}^{N}\left(S_{WIV/CS}[i] - S_{ERA5}[i]\right)^2}{\sum_{i=1}^{N}\left(S_{ERA5}[i]\right)^2}}. \tag{4.5}$$

The differences between the simulated fields and the ERA5 reference is mainly driven by three factors: the radar sensitivity leading to the omission of low-reflectivity events, the uncertainties in the $Z_e - S$ relationship and the instrument sampling (i.e., the fact that at any location S is sampled intermittently according to the revisit time). The latter contribution can be further decomposed into the contribution associated with the diurnal cycle of the orbit (i.e. the fact that at any given location the satellite passes only at certain times of the day) and to the sparseness of the measurements on different days.

To study the impact of potential blind zone effects, which are neglected in the following when using ERA5 surface snowfall, we also use height resolved ERA5 snow water content in section 4.3.

4.2 RESULTS

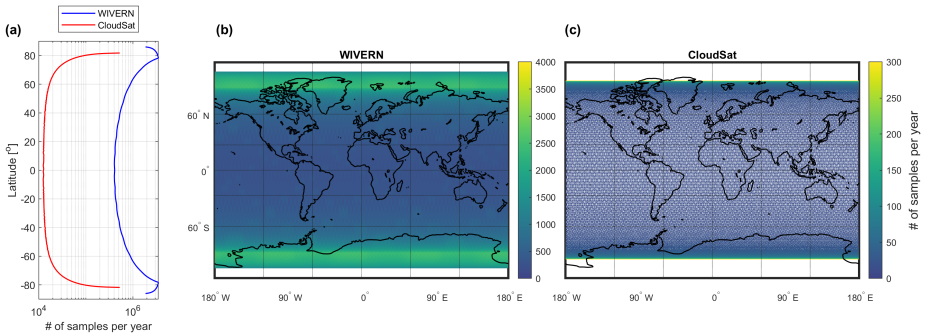

Fig. 4.2.1: *Number of annual samples collected by WIVERN (b) and CloudSat (c) per* $0.25^\circ \times 0.25^\circ$ *grid box. Note different color scales for the two panels. Zonal overpasses averaged over* 0.25° *wide latitude bands are shown in panel (a).*

The number of annual samples collected by WIVERN and CloudSat shown in Fig. 4.2.1 clearly demonstrates the advantage of the WIVERN sampling with an average of 6.696×10^8 total number of samples per year compared to 1.45×10^7 for CloudSat. While WIVERN produces global coverage with a resolution of 0.25° resolution for absolute latitudes below 86°, CloudSat has gaps (white spots in the right panel of Fig. 4.2.1) due to its periodic orbit and its viewing geometry. The WIVERN reduction of the blind region near the Poles up to 86° latitudes means a coverage of 95% of the Antarctic continent, which is a significant improvement in comparison to CloudSat's coverage of only 75% of the continent. And, different to CloudSat, WIVERN can cover Greenland and the Southern Ocean completely.

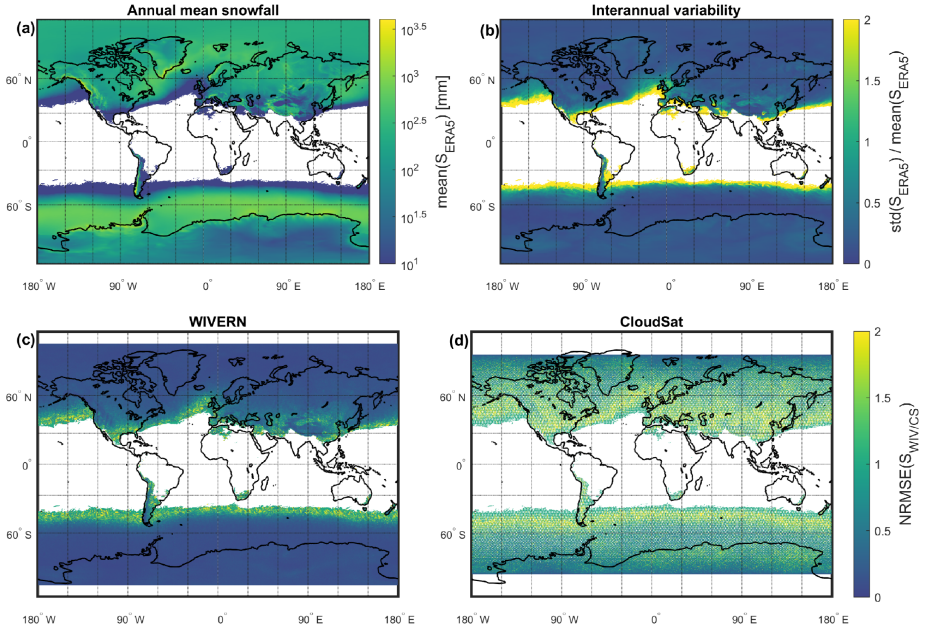

Fig. 4.2.2: *Panel (a) shows the mean annual accumulated snowfall according to ERA5 from 2001 to 2020. Panel (b) shows the normalized standard deviation, hence the inter-annual variability of the snowfall. The corresponding normalized root mean squared error on the 1-year accumulated snowfall sampled by WIVERN and CloudSat is also shown in panels (c) and (d), respectively.*

We set the estimated CloudSat and WIVERN errors in perspective to the mean snowfall rate. Fig. 4.2.2 shows the mean annual accumulated snowfall according to the ERA5 dataset in panel (a) and the normalized inter-annual variability of such snowfall in panel (b). The figure also depicts the NRMSE of the WIVERN (panel (c)) and CloudSat (panel (d)) annual accumulations. For WIVERN, the NRMSE is lower than 0.5 for most regions, with higher values in regions where the snowfall is rare so that the number of samples is low (i.e. in lower latitudes). The NRMSE tends to decrease when moving toward the poles due to the improved sampling (Fig. 4.2.1) and less intermittent snowfall observations. For CloudSat, the NRMSE is almost everywhere above 0.5, rising to much higher values in regions where the snowfall is very rare, due to the strong intermittency of the phenomenon and the poor sampling. The NRMSE constantly decreases as the satellite approaches the polar regions due to the higher number

of samples collected by the satellite and the high sensitivity of the CloudSat CPR. Furthermore, the nadir-looking viewing geometry of CloudSat CPR together with the repetition of the satellite's ground-track, generates gaps in the sampling of increased size as they get closer to the equator (see panel (d) in Fig. 4.2.2 or panel (c) in Fig. 4.2.1).

4.2.1 Errors on snowfall accumulation at different spatial and temporal scales

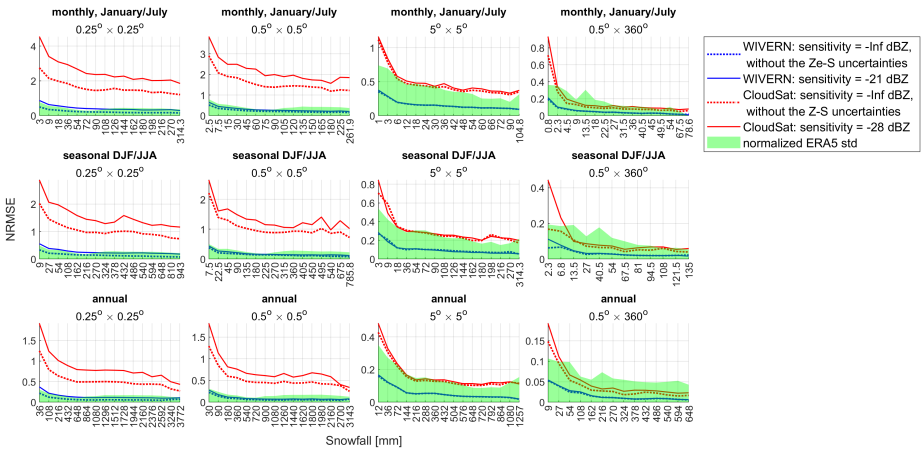

Fig. 4.2.3: *NRMSE for WIVERN (blue lines) and CloudSat (red lines) as a function of different snowfall accumulation classes and for different $lat \times lon$ grid box sizes and the zonal mean. The classes indicates the accumulated snowfall in the specified period and averaged in the specified spatial resolution domain. The NRMSE considering only the sampling contribution (dashed lines) and all sources of error (solid lines) are shown with different line styles. The monthly, seasonal and annual time scales are shown in the top, middle and bottom row, respectively. The snowfall classes are defined as snowfall intervals; e.g., for the annual timescale, the first bin corresponds to snowfall accumulations between 36 and 108 mm and the last bin to values $\geq$ 3772 mm. Results for the monthly (seasonal) case are shown when considering data of January (DJF) in the Northern Hemisphere, and July (JJA) in the Southern Hemisphere. The normalized climatological variability of ERA5 snowfall is defined as the normalized standard deviation and is indicated by the green shaded area.*

In order to answer the question of how the error varies when the temporal scale of accumulation is changed, the analysis has been conducted examining the estimated annual, seasonal and monthly accumulated snowfall. Similarly, for spatial scales, global snowfall has been aggregated into grids with lat$\times$lon box sizes of 0.25°$\times$0.25°, 0.5°$\times$0.5°, 1°$\times$1°, 5.0°$\times$5.0° and 10.0°$\times$10.0°. Zonal averages with a latitude resolution of 0.5° have been studied to observe the zonal mean behavior of the error as well.

Across the entire 20-year dataset, and for each temporal and spatial scale, grid points are grouped into classes based on the snowfall accumulation at the given timescale, averaged within a given spatial scale size pixel. For each class, the ERA5 mean snowfall, its standard deviation, and the NRMSE of WIVERN and CloudSat snowfall (relative to ERA5) are computed. Additionally, the climatological variability—defined

as the class standard deviation normalized by the class mean—is also used to benchmark results.

Figure 4.2.3 illustrates the NRMSE of WIVERN (blue lines) and CloudSat (red lines) as a function of snowfall accumulation for different temporal and spatial scales. The NRMSE is presented both with and without applying a sensitivity threshold and Z-S uncertainties. Trends indicate that uncertainty decreases as snowfall accumulation increases. This is because regions with low snowfall accumulations typically experience infrequent snowfall events, which are more likely to be missed, especially by CloudSat due to its coarser sampling resolution.

Averaging over larger spatial domains (left vs. right figure columns) and longer temporal scales (upper vs. lower figure rows) reduces the NRMSE. Furthermore, Z-S uncertainties diminish when averaging over broader spatial domains, leading to a rapid convergence of the total NRMSE toward the NRMSE value expected only from sampling errors.

These trends behave according to the central limit theorem: the probability density function (PDF) being sampled by the two instruments is the ERA5 hourly snowfall product, for each pixel. Each sampling process results in RMSE convergence following the relationship RMSE $\propto \frac{\text{std}(S)}{\sqrt{n}}$, where n represents the number of samples collected by the instrument (n_1 for WIVERN and n_2 for CloudSat, with $n_1 > n_2$). As the temporal and spatial scales increase, n grows, and the RMSE converges. WIVERN experiences faster convergence than CloudSat due to its larger number of collected samples.

At the annual, seasonal and monthly scales, the CloudSat NRMSE for zonal snow is lower than the climatological variability (with exceptions at very low snowfall rates). However, when looking at CloudSat $5^\circ \times 5^\circ$, the error exceeds the variability and is comparable to the WIVERN error at a much finer scale ($0.25^\circ \times 0.25^\circ$).

If the climatological variability is used as a threshold for acceptable measurement uncertainty, then CloudSat annual accumulations can only be used at the annual zonal domains. Vice versa, WIVERN produces errors lower than the natural variability at domains of at least $0.5^\circ \times 0.5^\circ$. WIVERN $0.25^\circ \times 0.25^\circ$ can still be useful but only for annual, seasonal and monthly accumulations larger than 864 mm, 270 mm and 108 mm, respectively.

As highlighted by Roberts et al. (2018), it is important to have precipitation datasets with spatial resolution better than 100 km poleward of 50°; the WIVERN mission could significantly contribute to such goal by providing snowfall rates at spatial scales better than 0.5°.

Impact of sampling error

The sampling error associated with the intermittent sampling of the snowfall (Fig. 4.2.3) is typically the dominant source of error; it decreases if the number of samples increases e.g., when coarsening the spatial and/or the temporal scale and/or if the snowfall becomes less intermittent (e.g., typically for higher accumulations). As the WIVERN sampling is much better than that of CloudSat, its sampling error is always lower than that of CloudSat (by at least a factor of two).

WIVERN and CloudSat orbits are both sun-synchronous, with a mean LTAN of 06:00 AM and 01:45 PM, respectively. This means that for any given point on the Earth's surface, the spacecraft will always pass over that point at the same local time. The local time of the observation is the same as the local time of the satellite overpass. This is also true for WIVERN; however, the large swath width means that the same

point can be observed at different local times, especially at high latitudes (e.g., at 80°S latitude there are on average 6.4 samples per day, see Fig. 4.2.1). Sampling a given site at only a few specific times of the day introduces an error in the snowfall accumulation due to the snowfall diurnal cycle (Watters et al., 2021; Milani and Wood, 2021), which is considered to be part of the sampling error. Since for WIVERN measurements at latitudes above 60°N and 60°S, the maximum revisit time (worst case scenario) is always less than 1 day (Battaglia et al., 2022), WIVERN sampling errors are only induced by the diurnal cycle effect. However, this is not the case for CloudSat CPR sampling which is characterized by an orbit repetition time of 16 days.

WIVERN's sampling errors are always smaller than the climatological variability at any spatial and temporal scales. Conversely, averaging over domains larger than 5°×5° is required at all timescales to reduce CloudSat sampling errors below the threshold dictated by the natural variability, with the sampling errors on the zonal snowfall being comparable with the WIVERN sampling errors for domains 0.25°×0.25° in size.

Impact of the radar sensitivity

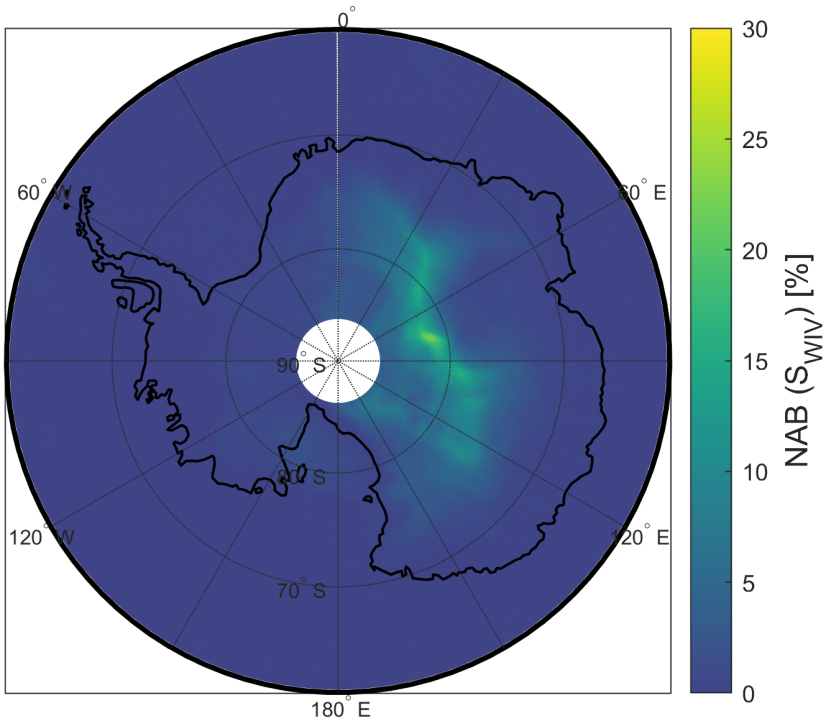

Fig. 4.2.4: *Normalized absolute bias between S_{WIV} computed with sensitivity = -21 dBZ, and S_{WIV} computed without the error induced by the sensitivity, normalized by the latter.*

The effect of the sensitivity emerges at locations where the snowfall rates generate reflectivities below the sensitivity of the radar. When adopting the $Z_e - S$ relationship of Eq. (4.1) the minimum detectable snowfall rate is 7.9×10^{-3} and 1.6×10^{-3} mm s^{-1} for WIVERN and CloudSat, respectively. Due to WIVERN's worse sensitivity, this effect is more pronounced than for CloudSat, and is only really significant only for

specific regions where snow rates below the detection threshold contribute significantly to the total accumulation. In particular, the error of the WIVERN accumulated snowfall in the region of the Antarctic desert comprised between $0°$ and $150°E$ is strongly affected by this source of error, as it can be seen in Fig. 4.2.2 and Fig. 4.2.4. Other regions such as central Greenland and western China are affected as well. However, globally, or when looking at the snowfall zonal behavior depicted in Fig. 4.2.5, or at points clustered based on similar snowfall values as outlined in Fig. 4.2.3, this effect appears to be negligible.

Impact of uncertainties in $Z_e - S$ relationship

Snowfall retrievals, especially those based on a single frequency, are limited by various uncertainties such as the characterization of the snowflake size distribution and the modelling of the backscattering properties of the ice crystals (Hiley et al., 2011; Kneifel et al., 2020; Tridon et al., 2019). At large snowfall rates, non-Rayleigh effects at the 94 GHz band cause further problems in the estimation of the snowfall rate. Uncertainties associated with the retrieval of S from Z_e are considered in this study as described in section 4.1, but it is important to note that the estimate of the $Z_e - S$ is assumed to be unbiased.

Fig. 4.2.3 shows the contributions of the sampling error, the $Z_e - S$ uncertainty and the sensitivity to the total error. As the latter contribution is negligible, the difference between the sampling error and the total error highlights the importance of the $Z_e - S$ uncertainties in the snowfall retrieval. For both WIVERN and CloudSat, the total NRMSE almost doubles compared to when considering only the effect of sampling at finer spatial scales, such as for the grid box size of $0.25° \times 0.25°$. Instead, when averaging the snowfall on larger areas, e.g., increasing the size of the grid boxes, the impact of the $Z_e - S$ is strongly mitigated, as expected from the assumption of the $Z_e - S$ estimate being unbiased. For WIVERN, thanks to the high number of collected samples, the contribution of the $Z_e - S$ uncertainty becomes negligible starting from $1.0° \times 1.0°$ spatial scale (not shown).

4.2.2 Errors on zonal snowfall: from annual to monthly scales

For global precipitation studies, zonal precipitation estimates are of particular interest for the observation of the Earth's climate, the detection of climate change and to evaluate and constrain historical and future climate simulations (Hagemann et al., 2006; Hegerl et al., 2015; Egli et al., 2022).

The zonal mean snowfall, where the latitude resolution is $0.5°$, is shown in Fig. 4.2.5. WIVERN and CloudSat can capture the zonal climatological mean of the reference at the monthly, seasonal and annual timescales, with the second being a bit more noisy than the first. CloudSat RMSE is within the standard deviation of ERA5 only for annual means. At the monthly and seasonal scales, CloudSat exceeds the standard deviation of ERA5 in the Northern Hemisphere during the warm season between $60°N$-$65°N$ and $25°N$-$40°N$, and during the cold season between $25°N$-$60°N$ and $25°S$-$60°S$. CloudSat exceeds the inter-annual climatological variability only at latitudes between $25°N$-$45°N$ and $25°S$-$45°S$. Instead, WIVERN RMSE remains within the climatological variability at the three timescales.

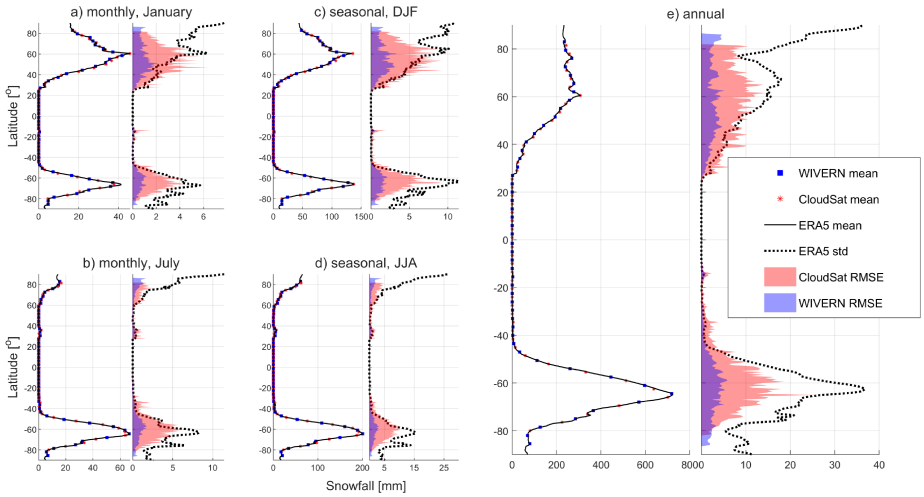

Fig. 4.2.5: *The figure shows the zonal mean snowfall at the monthly (January in panel a, and July in panel b), seasonal (DJF in panel c, and JJA in panel d) and annual (in panel e) timescales. The ERA5, WIVERN and CloudSat mean value are depicted with a solid black line, blue markers and red markers, respectively. The inter-annual variability of the zonal mean (i.e. ERA5 standard deviation) is shown by the black dashed line. The shaded areas outline the RMSE of WIVERN and CloudSat.*

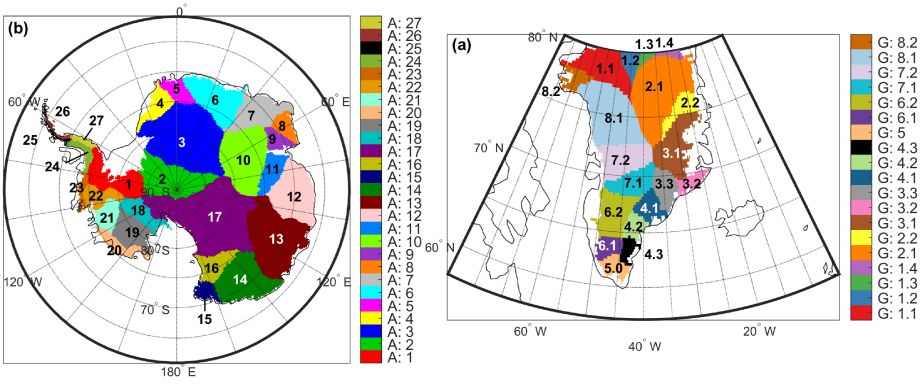

Fig. 4.2.6: *Division of Greenland and Antarctica into sub-regions based on the basins, according to Zwally et al. (2012).*

4.2.3 Regional estimation of accumulated snowfall

Estimation of snowfall in polar regions is of primary importance for quantifying the ice sheet mass balance and monitoring potential ice loss. Typically, estimates at annual and greater scales are useful to understand the ice sheet response to multi-year climate modes (e.g., El Niño), ice flow changes due to long term melting or thickening, the impact of ice sheet melting on the sea level rise and the inter-annual variability of the ice sheet mass balance. On the other hand, estimates at daily to seasonal time scales are useful to understand the seasonal variability, the grounding line migrations

and short-term oceanic or atmospheric forcing. Therefore, an analysis to quantify the regional effects of CloudSat and WIVERN sampling has been carried out in regions of Antarctica and Greenland defined by their drainage systems in Zwally et al. (2012). In Zwally et al. (2012), each basin is assigned an ID number and the subdivision is shown in Fig. 4.2.6. Antarctic regions of particular interests are the following:

- the Amundsen Sea sector, which consists of basins ranging from 20 to 22: it is characterized by the strongest ice mass loss on the continent, as described in Yang et al. (2023).
- the Antarctic Peninsula, which consists of basins ranging from 24 to 27, has experienced a rapid warming in recent years.

Such regions are also characterized by a large snowfall accumulations.
For Greenland, when considering the loss of ice sheet mass, the conditions are less variable over the area (Mouginot et al., 2019) and the regions of interests correspond to the basins 3.3, 4.1, 4.2, 4.3 and 5.0, which are the ones affected by the highest snowfall precipitation (see Fig. 4.2.2).

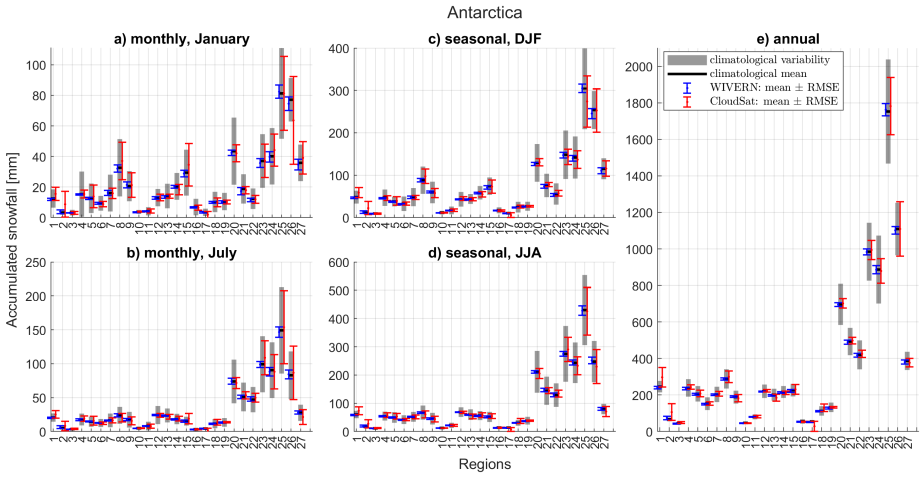

Fig. 4.2.7: *For each of the Antarctic regions (x-axis), the ERA5 mean snowfall accumulation (black line) and the climatological variability (grey shaded area) is shown. The mean accumulated snowfall ± RMSE sampled by WIVERN and CloudSat is shown with blue and red error bars, respectively. The result is shown for the monthly (panels a and b), seasonal (panels c and d) and annual (panel e) time scales. Results at the first two timescales are shown for January, July, DJF and JJA to highlight the different behavior between the two seasons.*

In order to provide useful measurements for estimating the total snowfall accumulation in a certain region, the RMSE must be significantly lower than the climatological variability of the region. As shown in Fig. 4.2.7, when trying to estimate the total snowfall in the regions of Antarctica, WIVERN can provide very useful benchmarks at all time scales, as their RMSE is low compared to the climatological variability of the regions, with the WIVERN's RMSE being systematically lower than the RMSE of CloudSat. Also CloudSat's RMSE falls above the variability in regions 1, 2, 17 and 26 at seasonal and annual timescales, and 1, 2, 17, 26 and 27 at monthly scales. Their

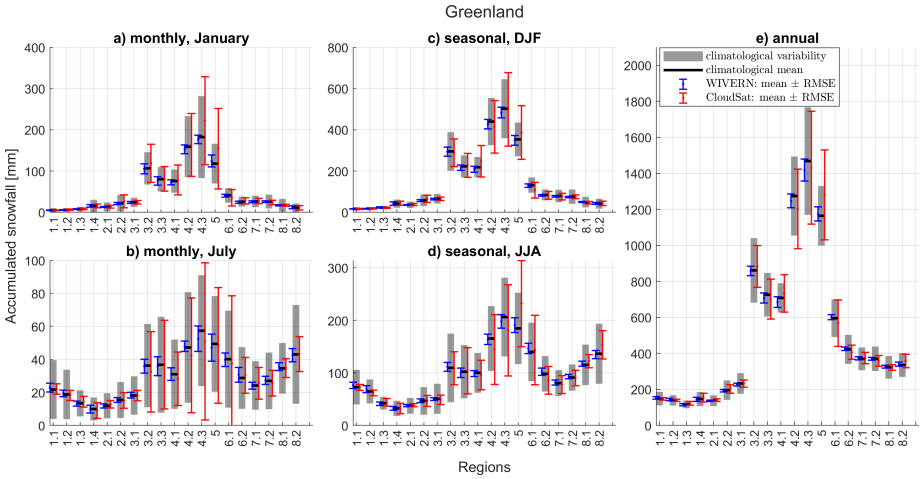

Fig. 4.2.8: *For each of the Greenland regions (x-axis), the ERA5 mean snowfall accumulation (black line) and the climatological variability (grey shaded area) is shown. The mean accumulated snowfall ± RMSE sampled by WIVERN and CloudSat is shown with blue and red error bars, respectively. The result is shown for the monthly (panels a and b), seasonal (panels c and d) and annual (panel e) time scales. Results at the first two timescales are shown for January, July, DJF and JJA to highlight the different behavior between the two seasons.*

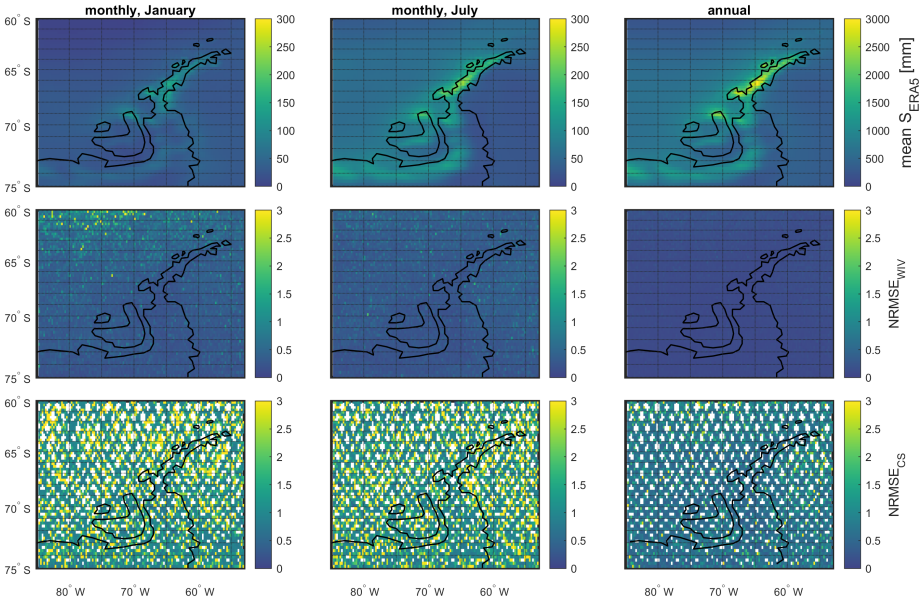

Fig. 4.2.9: *The top row shows the mean monthly and annual snowfall on the Antarctic Peninsula according to ERA5 on a lat-lon grid with box sizes of 0.25° ×0.25°. The middle and bottom rows show the corresponding NRMSE of WIVERN and CloudSat, respectively.*

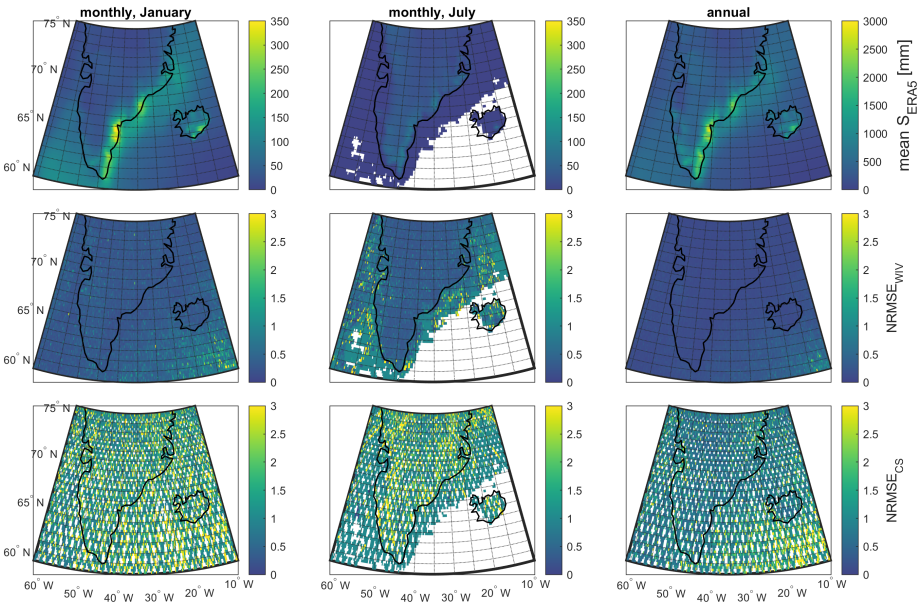

Fig. 4.2.10: *The top row shows the mean monthly and annual snowfall on Greenland and Iceland according to ERA5 on a lat-lon grid with box sizes of $0.25^\circ \times 0.25^\circ$. The middle and bottom rows show the corresponding NRMSE of WIVERN and CloudSat, respectively. Note that, in July, the snowfall on the points above the ocean is very low and is characterized by very weak or very rare snowfall events, which cause the NRMSE being $\sim$1 for WIVERN and CloudSat.*

estimates are thus both enough precise and accurate to provide useful insights for short and long-term frequency effects on the ice sheets, with some exceptions for CloudSat.

In the regions of Greenland, as shown in Fig.:4.2.8, CloudSat's sampling results in a very large RMSE, strongly exceeding ERA5 variability in some regions: 3,3, 4.1, 4.2, 4.3, 5.0 and 6.1 on all time scales and 3.2, 3,3, 4.1, 4.2, 4.3, 5.0 and 6.1 on the monthly scale. Instead, WIVERN can tackle short frequency effects affecting all the regions.

Overall, WIVERN produces a significantly lower RMSE than CloudSat (lower by at least a factor of 2), indicating that WIVERN might provide more robust estimates of regional snowfall variability.

Biases in the mean snowfall are introduced by the sampling, indicating an overestimation or underestimation of the snowfall, and are larger in Greenland than in Antarctica. Overall, WIVERN produces smaller biases than CloudSat, with some exceptions (e.g., region G:4.3 at the annual scale) related to the sensitivity. The number of samples collected by both satellites is higher in Antarctica than in Greenland (see Fig. 4.2.1), causing the RMSE and the bias to be larger in the latter.

WIVERN better capture the local variability within each region, e.g., the snowfall hotspots in the Antarctica Peninsula and along the southern east coast of Greenland are captured by WIVERN at the monthly to seasonal timescale, but not by CloudSat, as shown in Fig. 4.2.9 and Fig. 4.2.10 for the Antarctic Peninsula and Greenland, respectively.

4.3 INFLUENCE OF THE GROUND CLUTTER ON THE DETECTION OF THE SURFACE SNOWFALL PRECIPITATION

For space-borne radar observations, precipitation at the surface may be biased by ground clutter, with some very shallow events completely missed. Given the strong reduction of the normalised surface backscatter cross-section over the ocean at oblique angles of incidence (Battaglia et al., 2017; Wolde et al., 2019), WIVERN is expected to reduce the blind layer over ocean surfaces compared to nadir-looking radars (Meneghini and Kozu, 1990; Coppola et al., 2025). For sea ice and land surfaces, the importance of the clutter increases. The ERA5 vertical resolved snow water content profiles (Hersbach et al., 2023b, last seen: 12 April 2025) can be used in synergy with the CloudSat and WIVERN ground clutter height retrieved in Coppola et al. (2025) to determine the impact of the clutter on snowfall estimates. The ground clutter height, defined as the height of the SCR equal to 5 dB, depends on the surface type and the hydrometeor effective reflectivity at the surface, $Z_{e,surf}^{hydro}$. Therefore, this analysis is conducted for three different types of surface where snowfall is likely to occur: i.e. ice-free ocean, sea ice, and land assuming the attenuation caused by snowfall precipitation is negligible. WIVERN ground clutter height is lower over ice-free ocean and higher over land and sea ice than the clutter height of CloudSat (Coppola et al., 2025). Over land and sea-ice σ_0 at WIVERN incidence angle is assumed to be 5 dB lower than the one measured at nadir like for CloudSat.

The following procedure is implemented for each of the types of surface of interest:

1. Radar reflectivity profiles are computed from the Snow Water Content (SWC) profiles given by ERA5 using the Z-Ice Water Content (IWC) relationship for the 94 GHz in Liu and Illingworth (2000).

2. The ERA 5 sea ice edge product (Aaboe et al., 2023, last seen: 12 April 2025) has been used to determine if a given profile is located over land, sea ice or ice free ocean.

3. For each snow Z-profile, the ground clutter height (of WIVERN and CloudSat) is retrieved based on the reflectivity at the surface, $Z_{e,surf}^{hydro}$, as the median value of the histogram of the ground clutter height for that given $Z_{e,surf}^{hydro}$ shown in Coppola et al. (2025).

4. Z at the ground clutter height, $Z_{e,@\ \text{SCR=5dB}}^{hydro}$ is then retrieved, and statistics on the $Z_{e,surf}^{hydro} - Z_{e,@\ \text{SCR=5dB}}^{hydro}$ histogram is computed.

Mean and standard deviation of $Z_{e,surf}^{hydro} - Z_{e,@\ \text{SCR=5dB}}^{hydro}$ are shown in Fig. 4.3.1. The variability of $Z_{e,surf}^{hydro} - Z_{e,@\ \text{SCR=5dB}}^{hydro}$ is very small for both WIVERN and CloudSat, with WIVERN showing slightly better standard deviation results than CloudSat over ice-free oceans, while the opposite occurs over land and sea ice. CloudSat exhibits slightly lower biases compared to WIVERN, including ice-free ocean regions, despite WIVERN's ability to observe closer to the surface. This could be attributed to compensating effects of sublimation and shallow precipitation which cancel out at 1200 m better than at at 600 m (see also Maahn et al., 2014).

This analysis has some limitations: the resolution of the ERA5 data is 0.25° in latitude and longitude and may be too coarse to capture the vertical variability of the snow profiles. Also, the vertical resolution near the surface is only of ∼190 m. Together with known problems of ERA5 to represent the atmospheric boundary layer (Sinclair et al.,

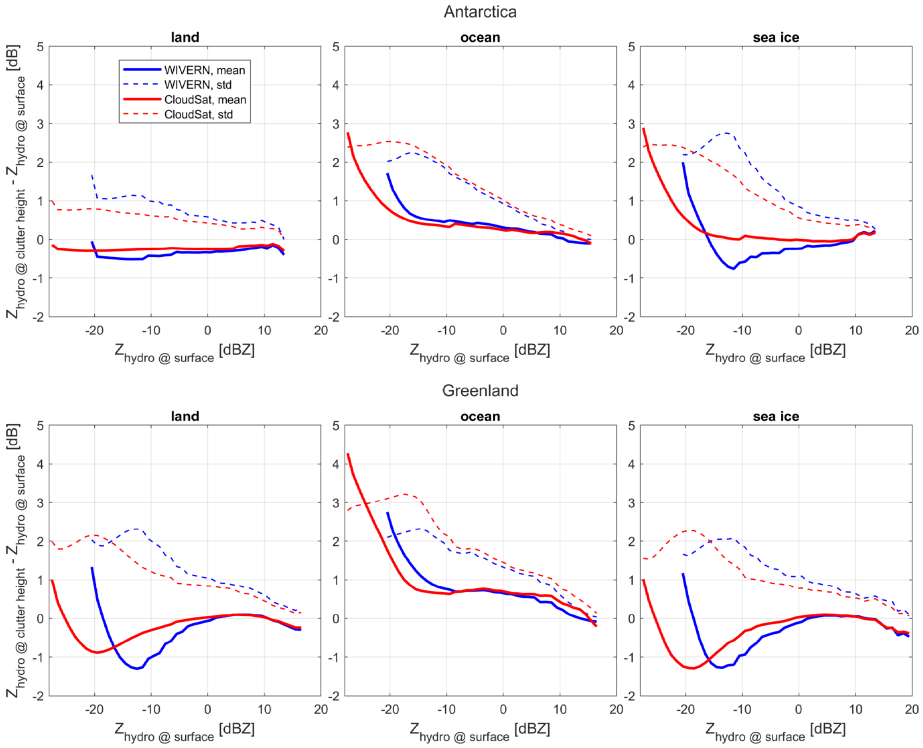

Fig. 4.3.1: *Mean (solid lines) and standard deviation (dashed lines) values of* $Z_{e,surf}^{hydro} - Z_{e,@\ SCR=5dB}^{hydro}$ *as a function of* $Z_{e,surf}^{hydro}$*, for WIVERN (blue) and CloudSat (red) for two different regions (top: Antarctica; bottom: Greenland) and three different surface types (left:land; centre: ice-free ocean; right:sea ice).*

2022), this could limit the validity of this analysis. To our knowledge, however, there is no alternative data product available that can characterize the vertical profile of cloud properties reliably all the way to the surface.

4.4 Summary and conclusions

Space-borne cloud radars are essential tools for observing snowfall globally (Stephens et al., 2018; Battaglia et al., 2020). Snowfall measurements are relevant for providing estimates of the snowfall accumulation, and thus for a wide range of applications: from regional water cycle budgets to quantification of the mass balance changes of the ice sheet, the ice shelves and the glaciers. However, the reliability of such products can be severely compromised by the intermittent and sparse sampling of snowfall carried out by the radar, with the number of samples collected in a given region in a given a time frame depending on the satellite orbit and on the radar scan geometry. For example, the WIVERN conically scanning radar (currently in Phase A of ESA's Earth Explorer programme) collects an order of magnitude more samples than a CloudSat or EarthCARE-like fixed near-nadir radar, which also has gaps in coverage due to the narrow swath.

The ERA5 hourly snowfall dataset has been used as a reference to simulate 20 years of snowfall accumulation as would have been sampled by a 94 GHz radar with WIVERN and CloudSat sampling geometry. Such accumulations are compared with the reference to assess the spatial and temporal scales at which these sensors become useful tools for estimating seasonal and/or regional accumulated snowfall. The error introduced by the two radars can be decomposed into the sampling error directly related to the intermittent sampling of the phenomenon, the error due to the uncertainty in the $Z_e - S$ relationship (assumed to be unbiased) and the error introduced by the minimum detectability threshold of the radar. Each contribution to the error has also been analyzed separately. To provide useful measurements, the error should be lower than the climatological variability, which is set to be the threshold of acceptable errors. The results show that:

1. For WIVERN and CloudSat, the sampling error is the main cause of uncertainty. It decreases as the temporal and spatial scale increase, with the error of WIVERN always being at least twice as small as the error of CloudSat (Fig. 4.2.3).

2. The radar sensitivity error is higher for WIVERN than for CloudSat (-21 vs. -28 dBZ) but the error is generally negligible, except for WIVERN in the regions where the snowfall events are weak and occur very frequently in time (e.g., in the centre of Antarctica, Fig. 4.2.4). As it is only relevant in correspondence of marginal snowy areas, its effect is globally insignificant for snowfall accumulation.

3. The error due to the $Z_e - S$ uncertainty is strongly mitigated when averaging spatially and temporally, as expected from the assumption of it being unbiased. For WIVERN, the large number of samples collected makes the error negligible starting from the $1.0^\circ \times 1.0^\circ$ spatial scale with excellent results already at the monthly scale.
   Overall, total errors produced by WIVERN are below the ERA5 climatological variability at the $0.5^\circ \times 0.5^\circ$ spatial scales already at the monthly scale. Conversely, CloudSat needs to be averaged at annual zonal scales to produce reliable estimates (Fig 4.2.3).

4. In the context of assessing total accumulation in various regions of Antarctica and Greenland (Fig. 4.2.7 and 4.2.8), WIVERN can provide reliable estimates already at the monthly scale. Instead, CloudSat offers less precise estimates, with RMSE exceeding the variability in some of the regions. Furthermore, when examining the local variability within these regions, CloudSat estimates are highly imprecise (Fig. 4.2.9 and Fig. 4.2.10).

5. Based on ERA5 reanalysis profiles, surface blind zone generates small bias in the reflectivity lower than 2 dB for Z>-20 dBZ (i.e. for snowfall that are important for mass accumulation) (Fig. 4.3.1). CloudSat has slightly lower biases than WIVERN over land, sea ice and ice-free ocean surfaces. Standard deviation is also lower except over ocean.

In conclusion, CloudSat is suitable for estimating snowfall accumulation over large areas and longer time scales (e.g., annual zonal), but its poor sampling capabilities limit the possibility to derive annual or monthly precipitation over domain smaller than zonal scales. The recently launched EarthCARE radar will face very similar sampling issues. On the other hand, a conically scanning wide swath radar, such as the one

proposed by the WIVERN team, could represent a unique observing system due to its improved sampling capabilities, contributing to the snowfall accumulation estimates over domains smaller than $0.5^\circ \times 0.5^\circ$ already at the monthly timescale.

Finally, the WIVERN radar will have a low Noise Equivalent Delta Temperature radiometer mode and will provide (noisy) estimates of polarimetric variables such as differential reflectivity and differential phase shifts (Battaglia et al., 2025). This could further improve the estimation of snowfall rates, e.g. by identifying the presence of rimed snow and supercooled droplets (Maherndl et al., 2025).

REFERENCES

Aaboe, S., Down, E., Sørensen, A., Lavergne, T., and Eastwood, S.: Sea-ice type climate data record 1978-present, v3.0. Copernicus Climate Change Service (C3S) Climate Data Store (CDS), https://doi.org/10.24381/cds.29c46d83, 2023.

Alexander, S. P., Protat, A., Berne, A., and Ackermann, L.: Radar-Derived Snowfall Microphysical Properties at Davis, Antarctica, J. Geophys. Res. Atm., 128, e2022JD038 389, https://doi.org/https://doi.org/10.1029/2022JD038389, e2022JD038389 2022JD038389, 2023.

Battaglia, A. and Panegrossi, G.: What Can We Learn from the CloudSat Radiometric Mode Observations of Snowfall over the Ice-Free Ocean?, Radio Sci., 12, https://doi.org/10.3390/rs12203285, 2020.

Battaglia, A., Wolde, M., D'Adderio, L. P., Nguyen, C., Fois, F., Illingworth, A., and Midthassel, R.: Characterization of Surface Radar Cross Sections at W-Band at Moderate Incidence Angles, IEEE Transactions on Geoscience and Remote Sensing, 55, 3846–3859, 10.1109/TGRS.2017.2682423, 2017.

Battaglia, A., Kollias, P., Dhillon, R., Roy, R., Tanelli, S., Lamer, K., Grecu, M., Lebsock, M., Watters, D., Mroz, K., Heymsfield, G., Li, L., and Furukawa, K.: Spaceborne Cloud and Precipitation Radars: Status, Challenges, and Ways Forward, Reviews of Geophysics, 58, e2019RG000 686, https://doi.org/10.1029/2019RG000686, e2019RG000686 10.1029/2019RG000686, 2020.

Battaglia, A., Martire, P., Caubet, E., Phalippou, L., Stesina, F., Kollias, P., and Illingworth, A.: Observation error analysis for the WInd VElocity Radar Nephoscope W-band Doppler conically scanning spaceborne radar via end-to-end simulations, Atmospheric Measurement Techniques, 15, 3011–3030, https://doi.org/10.5194/amt-15-3011-2022, 2022.

Battaglia, A., Rizik, A., Sikaneta, I., and Tridon, F.: I and Qs Simulation and Processing Envisaged for Spaceborne Polarization Diversity Doppler Radars, IEEE Transactions on Geoscience and Remote Sensing, 63, 1–14, https://doi.org/10.1109/TGRS.2025.3529672, 2025.

Bennartz, R., Fell, F., Pettersen, C., Shupe, M. D., and Schuettemeyer, D.: Spatial and temporal variability of snowfall over Greenland from CloudSat observations, Atmospheric Chemistry and Physics, 19, 8101–8121, https://doi.org/10.5194/acp-19-8101-2019, 2019.

Boening, C., Lebsock, M., Landerer, F., and Stephens, G.: Snowfall-driven mass change on the East Antarctic ice sheet, Geophysical Research Letters, 39, https://doi.org/https://doi.org/10.1029/2012GL053316, 2012.

Cao, Q., Hong, Y., Chen, S., Gourley, J., Zhang, J., and Kirstetter, P.-E.: Snowfall Detectability of NASA's CloudSat: The First Cross-Investigation of Its 2C-Snow-Profile Product and National Multi-Sensor Mosaic QPE (NMQ) Snowfall Data, Progress In Electromagnetics Research, 148, 55–61, https://doi.org/10.2528/PIER14030405, 2014.

Chen, F. and Staelin, D.: AIRS/AMSU/HSB precipitation estimates, IEEE Transactions on Geoscience and Remote Sensing, 41, 410–417, https://doi.org/10.1109/TGRS.2002.808322, 2003.

Coppola, M., Battaglia, A., Tridon, F., and Kollias, P.: Improved hydrometeor detection near the Earth's surface by a conically scanning spaceborne W-band radar, EGUsphere, 2025, 1–24, https://doi.org/10.5194/egusphere-2025-416, 2025.

Egli, M., Sippel, S., Pendergrass, A. G., de Vries, I., and Knutti, R.: Reconstruction of Zonal Precipitation From Sparse Historical Observations Using Climate Model Information and Statistical Learning, Geophysical Research Letters, 49, e2022GL099 826, https://doi.org/https://doi.org/10.1029/2022GL099826, e2022GL099826 2022GL099826, 2022.

Field, P. R. and Heymsfield, A. J.: Importance of snow to global precipitation, Geophysical Research Letters, 42, 9512–9520, https://doi.org/10.1002/2015GL065497, 2015.

Griesche, H. J., Ohneiser, K., Seifert, P., Radenz, M., Engelmann, R., and Ansmann, A.: Contrasting ice formation in Arctic clouds: surface-coupled vs. surface-decoupled clouds, Atmospheric Chemistry and Physics, 21, 10 357–10 374, https://doi.org/10.5194/acp-21-10357-2021, 2021.

Hagemann, S., Arpe, K., and Roeckner, E.: Evaluation of the Hydrological Cycle in the ECHAM5 Model, J. Climate, 19, 3810 – 3827, https://doi.org/10.1175/JCLI3831.1, 2006.

Hall, A.: The Role of Surface Albedo Feedback in Climate, Journal of Climate, 17, 1550 – 1568, https://doi.org/10.1175/1520-0442(2004)017<1550:TROSAF>2.0.CO;2, 2004.

Hegerl, G. C., Black, E., Allan, R. P., Ingram, W. J., Polson, D., Trenberth, K. E., Chadwick, R. S., Arkin, P. A., Sarojini, B. B., Becker, A., Dai, A., Durack, P. J., Easterling, D., Fowler, H. J., Kendon, E. J., Huffman, G. J., Liu, C., Marsh, R., New, M., Osborn, T. J., Skliris, N., Stott, P. A., Vidale, P.-L., Wijffels, S. E., Wilcox, L. J., Willett, K. M., and Zhang, X.: Challenges in Quantifying Changes in the Global Water Cycle, Bulletin of the American Meteorological Society, 96, 1097 – 1115, https://doi.org/10.1175/BAMS-D-13-00212.1, 2015.

Hersbach, H., Bell, B., Berrisford, P., Biavati, G., Horányi, A., Muñoz Sabater, J., Nicolas, J., Peubey, C., Radu, R., Rozum, I., Schepers, D., Simmons, A., Soci, C., Dee, D., and Thépaut, J.-N.: https://doi.org/10.24381/cds.adbb2d47, 2023a.

Hersbach, H., Bell, B., Berrisford, P., Biavati, G., Horányi, A., Muñoz Sabater, J., Nicolas, J., Peubey, C., Radu, R., Rozum, I., Schepers, D., Simmons, A., Soci, C., Dee, D., and Thépaut, J.-N.: ERA5 hourly data on pressure levels from 1940 to present. Copernicus Climate Change Service (C3S) Climate Data Store (CDS), https://doi.org/10.24381/cds.bd0915c6, 2023b.

Hiley, M. J., Kulie, M. S., and Bennartz, R.: Uncertainty Analysis for CloudSat Snowfall Retrievals, Journal of Applied Meteorology and Climatology, 50, 399 – 418, https://doi.org/10.1175/2010JAMC2505.1, 2011.

Kidd, C., Becker, A., Huffman, G. J., Muller, C. L., Joe, P., Skofronick-Jackson, G., and Kirschbaum, D. B.: So, How Much of the Earth's Surface Is Covered by Rain Gauges?, Bulletin of the American Meteorological Society, 98, 69 – 78, https://doi.org/10.1175/BAMS-D-14-00283.1, 2017.

Kneifel, S., Leinonen, J., Tyynela, J., Ori, D., and Battaglia, A.: Satellite precipitation measurement, vol. 1 of *Adv.Global Change Res.*, chap. Scattering of Hydrometeors, Springer, iSBN: 978-3-030-24567-2, 2020.

Kouki, K., Luojus, K., and Riihelä, A.: Evaluation of snow cover properties in ERA5 and ERA5-Land with several satellite-based datasets in the Northern Hemisphere in spring 1982–2018, The Cryosphere, 17, 5007–5026, https://doi.org/10.5194/tc-17-5007-2023, 2023.

Kulie, M. S. and Milani, L.: Seasonal variability of shallow cumuliform snowfall: A CloudSat perspective, Quarterly Journal of the Royal Meteorological Society, 144, 329–343, https://doi.org/10.1002/qj.3222, 2018.

Kulie, M. S., Milani, L., Wood, N. B., and L'Ecuyer, T. S.: Global Snowfall Detection and Measurement, pp. 699–716, Springer International Publishing, Cham, https://doi.org/10.1007/978-3-030-35798-6_12, 2020.

Li, H., Möhler, O., Petäjä, T., and Moisseev, D.: Two-year statistics of columnar-ice production in stratiform clouds over Hyytiälä, Finland: environmental conditions and the relevance to secondary ice production, Atmos. Chem. Phys., 21, 14 671–14 686, https://doi.org/10.5194/acp-21-14671-2021, 2021.

Liu, C.-L. and Illingworth, A. J.: Toward More Accurate Retrievals of Ice Water Content from Radar Measurements of Clouds, Journal of Applied Meteorology, 39, 1130 – 1146, https://doi.org/10.1175/1520-0450(2000)039<1130:TMAROI>2.0.CO;2, 2000.

Liu, G.: Deriving snow cloud characteristics from CloudSat observations, Journal of Geophysical Research: Atmospheres, 113, https://doi.org/https://doi.org/10.1029/2007JD009766, 2008.

Lopez-Cantu, T., Prein, A. F., and Samaras, C.: Uncertainties in Future U.S. Extreme Precipitation From Downscaled Climate Projections, Geophysical Research Letters, 47, e2019GL086 797, https://doi.org/10.1029/2019GL086797, e2019GL086797 10.1029/2019GL086797, 2020.

Maahn, M., Burgard, C., Crewell, S., Gorodetskaya, I. V., Kneifel, S., Lhermitte, S., Van Tricht, K., and van Lipzig, N. P. M.: How does the spaceborne radar blind zone affect derived surface snowfall statistics in polar regions?, Journal of Geophysical Research: Atmospheres, 119, 13,604–13,620, https://doi.org/10.1002/2014JD022079, 2014.

Maherndl, N., Battaglia, A., Kötsche, A., and Maahn, M.: Riming-Dependent Snowfall Rate and Ice Water Content Retrievals for W-band Cloud Radar, EGUsphere, pp. 1–27, https://doi.org/10/g89qh6, 2025.

Matrosov, S., Shupe, M., and Djalalova, I.: Snowfall Retrievals Using Millimeter-Wavelength Cloud Radars, Journal of Applied Meteorology and Climatology, 47, 769–777, doi: http://dx.doi.org/10.1175/2007JAMC1768.1, 2008.

Matrosov, S. Y., Shupe, M. D., and Uttal, T.: High temporal resolution estimates of Arctic snowfall rates emphasizing gauge and radar-based retrievals from the MOSAiC expedition, Elementa: Science of the Anthropocene, 10, 00 101, https://doi.org/10.1525/elementa.2021.00101, 2022.

Meneghini, R. and Kozu, T.: Spaceborne weather radar, Artech House, 1990.

Milani, L. and Kidd, C.: The State of Precipitation Measurements at Mid-to-High Latitudes, Atmosphere, 14, https://doi.org/10.3390/atmos14111677, 2023.

Milani, L. and Wood, N. B.: Biases in CloudSat Falling Snow Estimates Resulting from Daylight-Only Operations, Remote Sensing, 13, https://doi.org/10.3390/rs13112041, 2021.

Milani, L., Kulie, M. S., Casella, D., Dietrich, S., L'Ecuyer, T. S., Panegrossi, G., Porcù, F., Sanò, P., and Wood, N. B.: CloudSat snowfall estimates over Antarctica and the Southern Ocean: An assessment of independent retrieval methodologies and multi-year snowfall analysis, Atmospheric Research, 213, 121–135, https://doi.org/https://doi.org/10.1016/j.atmosres.2018.05.015, 2018.

Morrison, H., de Boer, G., Feingold, G., Harrington, J., Shupe, M. D., and Sulia, K.: Resilience of persistent Arctic mixed-phase clouds, Nature Geoscience, 5, 11–17, https://doi.org/doi.org/10.1038/ngeo1332, 2012.

Morrison, H., van Lier-Walqui, M., Fridlind, A. M., Grabowski, W. W., Harrington, J. Y., Hoose, C., Korolev, A., Kumjian, M. R., Milbrandt, J. A., Pawlowska, H., Posselt, D. J., Prat, O. P., Reimel, K. J., Shima, S.-I., van Diedenhoven, B., and Xue, L.: Confronting the Challenge of Modeling Cloud and Precipitation Microphysics, Journal of Advances in Modeling Earth Systems, 12, e2019MS001 689, https://doi.org/https://doi.org/10.1029/2019MS001689, e2019MS001689 2019MS001689, 2020.

Mouginot, J., Rignot, E., Bjørk, A. A., van den Broeke, M., Millan, R., Morlighem, M., Noël, B., Scheuchl, B., and Wood, M.: Forty-six years of Greenland Ice Sheet mass balance from 1972 to 2018, Proceedings of the National Academy of Sciences, 116, 9239–9244, https://doi.org/10.1073/pnas.1904242116, 2019.

Mroz, K., Montopoli, M., Battaglia, A., Panegrossi, G., Kirstetter, P., and Baldini, L.: Cross Validation of Active and Passive Microwave Snowfall Products over the Continental United States, Journal of Hydrometeorology, 22, 1297 – 1315, https://doi.org/10.1175/JHM-D-20-0222.1, 2021.

Mülmenstädt, J., Sourdeval, O., Delanoë, J., and Quaas, J.: Frequency of occurrence of rain from liquid-, mixed-, and ice-phase clouds derived from A-Train satellite retrievals, Geophysical Research Letters, 42, 6502–6509, https://doi.org/10.1002/2015GL064604, 2015.

Palerme, C., Kay, J. E., Genthon, C., L'Ecuyer, T., Wood, N. B., and Claud, C.: How much snow falls on the Antarctic ice sheet?, The Cryosphere, 8, 1577–1587, https://doi.org/10.5194/tc-8-1577-2014, 2014.

Palerme, C., Genthon, C., Claud, C., Kay, J. E., Wood, N. B., and L'Ecuyer, T.: Evaluation of current and projected Antarctic precipitation in CMIP5 models, Climate Dynamics, 48, 225–239, https://doi.org/10.1007/s00382-016-3071-1, 2017.

Panegrossi, G., Casella, D., Sanò, P., Camplani, A., and Battaglia, A.: Chapter 12 - Recent advances and challenges in satellite-based snowfall detection and estimation, in: Precipitation Science, edited by Michaelides, S., pp. 333–376, Elsevier, https://doi.org/https://doi.org/10.1016/B978-0-12-822973-6.00015-9, 2022.

Perovich, D., Polashenski, C., Arntsen, A., and Stwertka, C.: Anatomy of a late spring snowfall on sea ice, Geophysical Research Letters, 44, 2802–2809, https://doi.org/10.1002/2016GL071470, 2017.

Quante, L., Willner, S. N., Middelanis, R., and Levermann, A.: Regions of intensification of extreme snowfall under future warming, Scientific Reports, 11, https://doi.org/doi.org/10.1038/s41598-021-95979-4, 2021.

Roberts, M. J., Vidale, P. L., Senior, C., Hewitt, H. T., Bates, C., Berthou, S., Chang, P., Christensen, H. M., Danilov, S., Demory, M.-E., Griffies, S. M., Haarsma, R., Jung, T., Martin, G., Minobe, S., Ringler, T., Satoh, M., Schiemann, R., Scoccimarro, E., Stephens, G., and Wehner, M. F.: The Benefits of Global High Resolution for Climate Simulation: Process Understanding and the Enabling of Stakeholder Decisions at the Regional Scale, Bulletin of the American Meteorological Society, 99, 2341 – 2359, https://doi.org/10.1175/BAMS-D-15-00320.1, 2018.

Scarsi, F. E., Battaglia, A., Maahn, M., and Lhermitte, S.: How to reduce sampling errors in spaceborne cloud radar-based snowfall estimates, The Cryosphere, 19, 4875–4892, https://doi.org/10.5194/tc-19-4875-2025, 2025.

Schoger, S. Y., Moisseev, D., von Lerber, A., Crewell, S., and Ebell, K.: Snowfall-Rate Retrieval for K- and W-Band Radar Measurements Designed in Hyytiälä, Finland, and Tested at Ny-Ålesund, Svalbard, Norway, Journal of Applied Meteorology and Climatology, 60, 273 – 289, https://doi.org/10.1175/JAMC-D-20-0095.1, 2021.

Scipión, D. E., Mott, R., Lehning, M., Schneebeli, M., and Berne, A.: Seasonal small-scale spatial variability in alpine snowfall and snow accumulation, Water Resources Research, 49, 1446–1457, https://doi.org/https://doi.org/10.1002/wrcr.20135, 2013.

Shates, J. A., Pettersen, C., L'Ecuyer, T. S., and Kulie, M. S.: KAZR-CloudSat Analysis of Snowing Profiles at the North Slope of Alaska: Implications of the Satellite Radar Blind Zone, Journal of Geophysical Research: Atmospheres, 130, e2024JD042 700, https://doi.org/10.1029/2024JD042700, e2024JD042700 2024JD042700, 2025.

Sinclair, V. A., Ritvanen, J., Urbancic, G., Erner, I., Batrak, Y., Moisseev, D., and Kurppa, M.: Boundary-layer height and surface stability at Hyytiälä, Finland, in ERA5 and observations, Atmospheric Measurement Techniques, 15, 3075–3103, https://doi.org/10.5194/amt-15-3075-2022, 2022.

Skofronick-Jackson, G. and Johnson, B. T.: Surface and atmospheric contributions to passive microwave brightness temperatures for falling snow events, Journal of Geophysical Research: Atmospheres, 116, https://doi.org/https://doi.org/10.1029/2010JD014438, 2011.

Skofronick-Jackson, G., Kim, M.-J., Weinman, J., and Chang, D.-E.: A physical model to determine snowfall over land by microwave radiometry, IEEE Transactions on Geoscience and Remote Sensing, 42, 1047–1058, https://doi.org/10.1109/TGRS.2004.825585, 2004.

Slatyer, R. A., Umbers, K. D. L., and Arnold, P. A.: Ecological responses to variation in seasonal snow cover, Conservation Biology, 36, e13 727, https://doi.org/10.1111/cobi.13727, 2022.

Smalley, M., L'Ecuyer, T., Lebsock, M., and Haynes, J.: A Comparison of Precipitation Occurrence from the NCEP Stage IV QPE Product and the CloudSat Cloud Profiling Radar, Journal of Hydrometeorology, 15, 444 – 458, https://doi.org/10.1175/JHM-D-13-048.1, 2014.

Souverijns, N., Gossart, A., Gorodetskaya, I. V., Lhermitte, S., Mangold, A., Laffineur, Q., Delcloo, A., and van Lipzig, N. P. M.: How does the ice sheet surface mass balance relate to snowfall? Insights from a ground-based precipitation radar in East Antarctica, The Cryosphere, 12, 1987–2003, https://doi.org/10.5194/tc-12-1987-2018, 2018a.

Souverijns, N., Gossart, A., Lhermitte, S., Gorodetskaya, I. V., Grazioli, J., Berne, A., Duran-Alarcon, C., Boudevillain, B., Genthon, C., Scarchilli, C., and van Lipzig, N. P. M.: Evaluation of the CloudSat surface snowfall product over Antarctica using ground-based precipitation radars, The Cryosphere, 12, 3775–3789, https://doi.org/10.5194/tc-12-3775-2018, 2018b.

Steiger, R., Scott, D., Abegg, B., Pons, M., and Aall, C.: A critical review of climate change risk for ski tourism, Current Issues in Tourism, 22, 1343–1379, https://doi.org/10.1080/13683500.2017.1410110, 2019.

Stephens, G., Winker, D., Pelon, J., Trepte, C., Vane, D., Yuhas, C., L'Ecuyer, T., and Lebsock, M.: CloudSat and CALIPSO within the A-Train: Ten Years of Actively Observing the Earth System, Bulletin of the American Meteorological Society, 99, 569 – 581, https://doi.org/10.1175/BAMS-D-16-0324.1, 2018.

Stephens, G. L., Vane, D. G., Boain, R. J., Mace, G. G., Sassen, K., Wang, Z., Illingworth, A. J., O'Connor, E. J., Rossow, W. B., Durden, S. L., Miller, S. D., Austin, R. T., Benedetti, A., Mitrescu, C., and Team, C. S.: The CloudSat mission and the A-Train: A new dimension of space-based observations of clouds and precipitation, Bull. Amer. Meteorol. Soc., 83, 1771–1790, https://doi.org/10.1175/BAMS-83-12-1771, 2002.

Strong, C. K., Ye, Z., and Shi, X.: Safety Effects of Winter Weather: The State of Knowledge and Remaining Challenges, Transport Reviews, 30, 677–699, https://doi.org/10.1080/01441640903414470, 2010.

Tridon, F., Battaglia, A., Chase, R. J., Turk, F. J., Leinonen, J., Kneifel, S., Mroz, K., Finlon, J., Bansemer, A., Tanelli, S., Heymsfield, A. J., and Nesbitt, S. W.: The Microphysics of Stratiform Precipitation During OLYMPEX: Compatibility Between Triple-Frequency Radar and Airborne In Situ Observations, J. Geophys. Res. Atm., 124, 8764–8792, https://doi.org/10.1029/2018JD029858, 2019.

Tridon, F., Silber, I., Battaglia, A., Kneifel, S., Fridlind, A., Kalogeras, P., and Dhillon, R.: Highly supercooled riming and unusual triple-frequency radar signatures over McMurdo Station, Antarctica, Atmos. Chem. Phys., 22, 12 467–12 491, https://doi.org/10.5194/acp-22-12467-2022, 2022.

Tridon, F., Battaglia, A., Rizik, A., Scarsi, F. E., and Illingworth, A.: Filling the Gap of Wind Observations Inside Tropical Cyclones, Earth and Space Science, 10, e2023EA003 099, https://doi.org/https://doi.org/10.1029/2023EA003099, e2023EA003099 2023EA003099, 2023.

Wang, Y., Liu, G., Seo, E.-K., and Fu, Y.: Liquid water in snowing clouds: Implications for satellite remote sensing of snowfall, Atmospheric Research, 131, 60–72, https://doi.org/https://doi.org/10.1016/j.atmosres.2012.06.008, perspectives of Precipitation Science - Part I, 2013.

Wasti, A., Ray, P., Wi, S., Folch, C., Ubierna, M., and Karki, P.: Climate change and the hydropower sector: A global review, WIREs Climate Change, 13, e757, https://doi.org/10.1002/wcc.757, 2022.

Watters, D., Battaglia, A., and Allan, R. P.: The Diurnal Cycle of Precipitation according to Multiple Decades of Global Satellite Observations, Three CMIP6 Models, and the ECMWF Reanalysis, J. Climate, 34, 5063 – 5080, https://doi.org/10.1175/JCLI-D-20-0966.1, 2021.

Wehr, T., Kubota, T., Tzeremes, G., Wallace, K., Nakatsuka, H., Ohno, Y., Koopman, R., Rusli, S., Kikuchi, M., Eisinger, M., Tanaka, T., Taga, M., Deghaye, P., Tomita, E., and Bernaerts, D.: The EarthCARE mission – science and system overview, Atmospheric Measurement Techniques, 16, 3581–3608, https://doi.org/10.5194/amt-16-3581-2023, 2023.

Wolde, M., Battaglia, A., Nguyen, C., Pazmany, A. L., and Illingworth, A.: Implementation of polarization diversity pulse-pair technique using airborne W-band radar, Atmospheric Measurement Techniques, 12, 253–269, https://doi.org/10.5194/amt-12-253-2019, 2019.

Yang, D., Elomaa, E., Tuominen, A., Aaltonen, A., Goodison, B., Gunther, T., Golubev, V., Sevruk, B., Madsen, H., and Milkovic, J.: Wind-induced Precipitation Undercatch of the Hellmann Gauges, Hydrology Research, 30, 57–80, https://doi.org/10.2166/nh.1999.0004, 1999.

Yang, T., Liang, Q., Zheng, L., Li, T., Chen, Z., Hui, F., and Cheng, X.: Mass Balance of the Antarctic Ice Sheet in the Early 21st Century, Remote Sensing, 15, https://doi.org/10.3390/rs15061677, 2023.

Zwally, H., Giovinetto, M., Beckley, M., and Saba, J.: Antarctic and Greenland Drainage Systems, URL `https://earth.gsfc.nasa.gov/cryo/data/polar-altimetry/antarctic-and-greenland-drainage-systems`, 2012.

Chapter 5

Simulation of three-dimensional multiple scattering effects in radar reflectivity profiles

This chapter is extensively based on the following publication:
Scarsi, F. E., Battaglia, A., Bukowski, J., Marinescu, P. J., Singh, I., van den Heever, S. C., *A Monte Carlo Framework for Forward Modeling of Three-dimensional Multiple Scattering Effects* (submitted to AGU Journal of Geophysical Research: Atmosphere)

5 SIMULATION OF THREE-DIMENSIONAL MULTIPLE SCATTERING EFFECTS IN RADAR REFLECTIVITY PROFILES

MS effects occur when part of the radiation is scattered several times within the medium before returning to the radar receiver and is contributing significantly to the radar echo. This phenomenon is particularly pronounced in scattering optically thick hydrometeor layers, such as those containing dense ice particles. Convective systems, known to produce large amounts of hail and graupel, frequently meet these conditions (Battaglia et al., 2016a). The impact of MS becomes relevant when the scattering mean free paths become comparable or smaller than the radar footprints. Since the former (latter) typically increases (decreases) with the frequency the effect can be pronounced in the full range of radar frequencies adopted for space-borne radars. Also, the radar footprint is at km-scale for space-borne radars due to their altitude at LEO (typycally between 300 and 750 km), larger than in ground-based radars. Under such circumstances, MS effects can severely alter the radar backscattered signal, complicating the retrieval of geophysical properties, as Single Scattering (SS) assumptions are no longer valid. Moreover, it reduces the correlation between radar pulses, further complicating Doppler velocity retrievals (Battaglia and Tanelli, 2011).

Current retrieval algorithms and fast forward modeling approaches commonly rely on the TDTS approximation based method developed by Hogan and Battaglia (2008). This method also simplifies the medium as one-dimensional, assuming that its properties vary only along the radar's range direction while remaining constant in the orthogonal directions. While computationally efficient, this approximation might introduce errors, particularly in horizontally heterogeneous environments such as convective systems.

MS effects (Battaglia et al., 2010) have been observed in the CloudSat, GPM and EarthCARE reflectivity profiles (Matrosov et al., 2008; Matrosov and Battaglia, 2009; Battaglia et al., 2008a, 2015, 2016b; Galfione et al., 2025) and may potentially affect also the next generation space-borne radars.

Forward modelling is essential not only for the reasons explained in 2.4, but also because an accurate representation of the radar reflectivity is crucial to reducing errors and biases in machine learning-based retrievals. In this context, realistic forward modelling of reflectivity profiles, particularly those affected by multiple scattering, could significantly enhance mission performance. This is especially relevant for INCUS, as convective storms are known to induce strong MS effects and to be characterized by stark spatial variability.

The EarthCARE (Kollias et al., 2018; Wehr et al., 2023) mission is providing 94 GHz radar measurements of vertically resolved profiles of clouds and precipitation, also providing useful information of convective systems (Galfione et al., 2025). Due to

its high frequency, Z- and Doppler velocity profiles are contaminated by MS effects, including second trip echoes and mirror images (Meneghini and Atlas, 1986; Li and Nakamura, 2002; Battaglia and Simmer, 2008; Battaglia, 2021).

Monte Carlo methods have previously been used to evaluate MS effects for both polarized and non-polarized radiation (Marzano et al., 2003; Battaglia and Mantovani, 2005; Battaglia et al., 2006, 2008b). However, these approaches either do not account for the full three-dimensional geometry of atmospheric systems or require significant computational resources.

This paper presents a Monte Carlo method based on importance sampling that incorporates the complete three-dimensional structure of the hydrometeor field to simulate reflectivity profiles with MS contributions. This is used to simulate Z-profiles in the INCUS and EarthCARE orbital and radar configurations. The explicit goal is to evaluate the errors introduced by 1D approximation in quantifying MS enhancements; this is achieved by comparing the reflectivity profiles generated by this method with those produced using the TDTS approximation. Importance sampling (Elvira and Martino, 2021) is used to reduce computational cost. Additionally, the method can simulate surface scattering contributions, which are crucial for accurately modeling mirror images and second-trip echoes phenomena, which are observed and predicted to occur in EarthCARE radar returns (Battaglia, 2021).

5.1 THE RADAR EQUATION IN PRESENCE OF MULTIPLE SCATTERING

Usually, the radar equation relates the radar reflectivity to the single scattering contributions only. However, contributions due to multiple scattering may occur. The antenna radiates a certain power P_t, and the power density flux incident to a volume dV illuminated by the radar antenna in the direction $\hat{\Omega}_t$ is (Tsang et al., 1985; Marzano et al., 2003):

$$F_t(\hat{\Omega}_t, r_i) = \frac{P_t\, G(\hat{\Omega}_t)}{4\pi\, r_i^2} \tag{5.1}$$

The apparent received power, at time t, and therefore due to the range gate at distance $r = c\,t/2$, in presence of MS contributions may be expressed as:

$$\langle P_r(r) \rangle = A_{e0} \int_{4\pi} G_n(\hat{\Omega})\, \langle I_a(r, \hat{\Omega}) \rangle d\Omega \tag{5.2}$$

where A_{e0} ($= \lambda^2 G_0/(4\pi)$) is the maximum antenna equivalent area (G_0 is the antenna gain along the boresight), $G_n(\hat{\Omega}) = G(\hat{\Omega})/G_0$ is the normalized antenna pattern such its maximum value is equal to 1, and $\langle I_a(r, \hat{\Omega})$ is the specific intensity corresponding to radiation that has travelled a path equal to $2r$ (thus an apparent range equal r) undergoing SS and MS events.

The apparent received power is related to the radar reflectivity through the radar equation Eq. 2.1: (Fabry, 2015):

$$P_r(r) = C_M \frac{Z(r)}{r^2} \tag{5.3}$$

where in this case $Z(r)$ is the multiply scattered radar reflectivity factor.

Hereafter, the following notation will be used for the specific intensity I, the power P, and the radar reflectivity Z:

- superscript ^{SS} denotes the contribution given by SS only;
- superscript ^{MS} denotes the contribution given by all the orders of scattering;
- superscript $^{(k)}$ indicates the contribution given by the k^{th} order of scattering. Note that, $^{(1)} \equiv^{SS}$ and $^{MS} \equiv {}^{(1)} + {}^{(\geq 2)}$.

By combining Eq. (5.2) and Eq. (5.3) the radar reflectivity factor due to both SS and MS contributions can be written as:

$$Z_m^{MS}(r) = \left[\frac{\int_{4\pi} G_n(\hat{\Omega})\, I^{MS}(\hat{\Omega}, r)\, r^2 d\Omega}{P_t} \right] \frac{1}{G_0\, \Omega_{2A}} \frac{\lambda^4}{\pi^5 |K_w|^2} \frac{(4\pi)^2}{\Delta r} \tag{5.4}$$

where r is the apparent range.

where $I^{MS}(\hat{\Omega}, r) = I^{(1)}(\hat{\Omega}, r) + I^{(\geq 2)}(\hat{\Omega}, r)$ is the specific intensity due to all the orders of scattering.

For the computation of Z_m^{MS}, the SS ($Z_m^{SS} = Z_m^{(1)}$) and the MS enhancement ($Z_m^{(\geq 2)}$) can be assessed separately. The SS component can be derived analytically (this is the only component which is typically accounted for by radar simulators, e.g. Haynes et al. (2007); Battaglia et al. (2022); Moradi et al. (2025)), while the MS enhancement requires solving the Radiative Transfer Equation (RTE). In this study, we focus solely on the total radiance, disregarding its polarization state, and therefore, solving the scalar form of the RTE suffices for our analysis.

5.2 METHODOLOGY FOR THE SIMULATION OF RADAR REFLECTIVITY PROFILES

The antenna boresight direction is denoted by $\hat{\boldsymbol{U}}_p$, while the spacecraft's position is represented by $\boldsymbol{R}_{SC}$.

5.2.1 Single scattering contribution

Single-scattering radar reflectivity profiles are simulated similarly as in Battaglia et al. (2022). The radiation beam is discretized into n_{θ_b} and n_{ϕ_b} elevation, θ_b, and azimuth angles, ϕ_b, relative to the boresight direction. Each pair of θ_b and ϕ_b, defines a ray, and therefore the beam is discretized into $n_{\theta_b} \times n_{\phi_b}$ rays. The beam, and therefore each ray, is also discretized into n_r range bins. Each beam discretization element is defined by its distance, r, from the radar, and by the direction $\hat{\Omega}(\theta_b, \phi_b)$. The pointing direction of a ray can be specified by the unit vector $\hat{\boldsymbol{U}}_1$ corresponding to that ray.

The radar reflectivity factor due to single-scattering contributions, Z^{SS}, corresponding to a given range gate at a distance from the radar r along the direction $\hat{\boldsymbol{U}}_1$, at position $\boldsymbol{R}_1 = \boldsymbol{R}_{SC} + r\,\hat{\boldsymbol{U}}_1$, is computed analytically as follows.

The contributions given by the atmospheric shell centered in r and in between $r - \delta r/2$ and $r + \delta r/2$ are computed as:

$$Z_{\delta r}^{atm,\,SS}(r) = \frac{\int\int\int_v \left[G_n(\theta,\phi)\right]^2\, Z_e(r)\, e^{-2\tau}\, dV}{\int\int\int_v \left[G_n(\theta,\phi)\right]^2\, dV} \tag{5.5}$$

$$= \frac{\int_0^{2\pi}\int_0^{\pi} \left[G_n(\theta,\phi)\right]^2\, Z_e(r,\theta,\phi)\, e^{-2\tau}\, r^2\, \sin\theta\, d\theta\, d\phi}{\int_0^{2\pi}\int_0^{\pi} \left[G_n(\theta,\phi)\right]^2\, r^2\, \sin\theta\, d\theta\, d\phi} \tag{5.6}$$

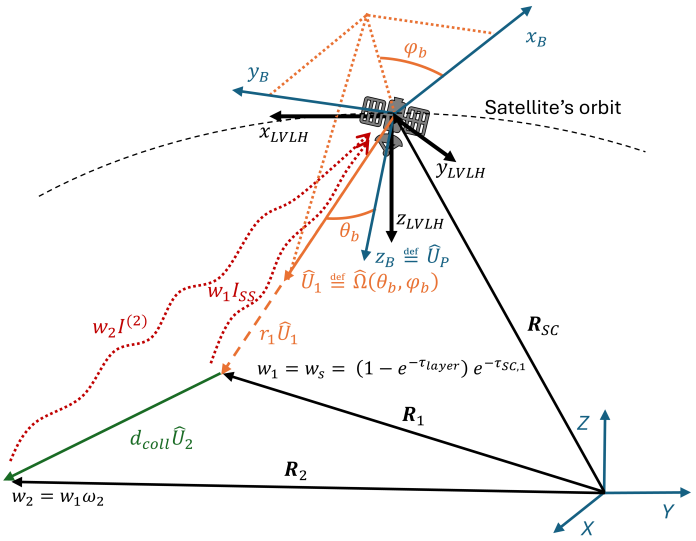

Fig. 5.2.1: *Example of a 2^{nd} order scattering contribution. $(x_B,\, y_B,\, z_B)$ is the body reference frame centred in the radar antenna, with z_B being parallel to the antenna boresight $\hat{\boldsymbol{U}}_P$. $(X,\, Y,\, Z)$ is the topocentric reference frame, and $(x_{LVLH},\, y_{LVLH},\, z_{LVLH})$ is the Local-Vertical Local-Horizontal coordinate system.*

while the contribution given by the surface is

$$Z_{\delta r}^{surf,\,SS}(r) = \frac{\lambda^4}{\pi^5\, |K_w|^2\, \Omega_{2A}}\, \frac{r^2}{\delta r} \int_{\Sigma} \frac{[G_n(\theta,\phi)]^2\, \sigma_0(\theta,\phi)\, e^{-2\tau}}{r^4}\, d\Sigma' \tag{5.7}$$

where:

- τ is the optical thickness of the atmosphere between the radar and the beam discretization element, centred at r;
- $\int\int\int_v dV = \delta r \int_\Omega r^2\, d\Omega' = \delta r \int_0^{2\pi} \int_0^{\pi} r^2\, \sin\theta\, d\theta\, d\phi$;
- $\Omega_{2A} = \int_{4\pi} \left[G_n(\hat{\Omega})\right]^2 d\Omega = \int_0^{2\pi} \int_0^{\pi} [G_n(\theta,\phi)]^2\, \sin\theta\, d\theta\, d\phi$;
- σ_0 is the normalized radar cross-section (NRCS) of the surface;
- Σ is a surface obtained by the intersection of the Earth's surface and the spherical shell of radii $r - \delta r/2$ and $r + \delta r/2$.

The total reflectivity signal due to single scattering is thus obtained summing the atmospheric and surface contributions:

$$Z_{\delta r}^{SS}(r) = Z_{\delta r}^{atm,\,SS}(r) + Z_{\delta r}^{surf,\,SS}(r) \tag{5.8}$$

and then by performing a convolution with the radar response function:

$$Z_m^{SS}(r) = (\omega_{PTR}^2 * Z_{\delta r}^{SS})(r) \tag{5.9}$$

where ω_{PTR} represents the point target response that accounts for the transmitted pulse shape and the receiver response.

5.2.2 Multiple scattering reflectivity with the time-dependent two-streams approximation

The algorithm of Hogan and Battaglia (2008) is used for computing the radar reflectivity in presence of multiple scattering with TDTS approximation, $Z_m^{MS,\,TDTS}$. To take into account for inhomogeneity of the scattering medium within the antenna beam, $Z_{\delta r}^{MS,TDTS}(r,\theta,\phi)$ is computed along each of the rays in which the beam has been discretized. The contribution given by each ray is then antenna weighted averaged, as done for the single-scattering reflectivity in Eq. 5.5. The convolution with the PTR is performed as done in Eq. 5.9 to obtain $Z_m^{MS,\,TDTS}(r)$.

5.2.3 Multiple scattering contributions with three-dimensional effects

To compute the Z_m^{MS} we need to estimate the term contained in the square brackets of Eq. 5.4. That term is estimated via an importance sampling based Monte Carlo algorithm where common biased techniques (described in App. 5.A, 5.C, 5.B and 5.D) are employed. Reference frames transformations between one and the other that are employed in the simulator are described in App. 5.E.

Distribution of transmitted radiation

A total N_T "photon streams" corresponds to a total transmitted power P_t (or equivalently for a pulse of duration Δt to a transmitted energy $P_t \Delta t$). The transmitted radiation is forced to have the first scattering interaction in different atmospheric spherical shells with mean radius r_i and thickness δr. The number of photons interacting in the spherical shell with mean radius is r_i is $N_P(r_i) = f(r_i) N_T$ where

$$f(r_i) = \frac{\int_{4\pi} G_n(\hat{\Omega}) \left[\exp(-\int_0^{r_i-\delta r} k_{ext}(\hat{\Omega}, r)\, dr)\right] \left[1 - \exp(-\int_{r_i-\delta r/2}^{r_i+\delta r/2} k_s(\hat{\Omega}, r)\, dr)\right]\, d\Omega}{\int_{4\pi} G_n(\hat{\Omega})\, d\Omega} \tag{5.10}$$

k_{ext} and k_s being the extinction and scattering coefficients, respectively. Given a direction $\hat{\Omega}$, the first term in the square brackets represents the probability of radiation in the $\hat{\Omega}$ direction to advance to the boundary of the shell closer to the radar whereas the second term represents the probability of scattering within the shell for the same direction.

The directions in which the N_P photons are emitted by the radar and forced to reach and to single-scatter at range r_i are randomly sampled from a distribution equal to the antenna pattern. Therefore, given Eq. 5.1, each of the simulated photon represents a power density flux of

$$F_t^j = \frac{P_t\, G_0\, \Omega_p}{4\pi\, N_P\, r_i^2} \tag{5.11}$$

where $\Omega_p = \int_{4_\pi} G_n(\hat{\Omega}) d\Omega$ Furthermore, if the antenna has a Gaussian pattern, the direction of emission can be sampled analytically as shown in App 5.C.

Contribution of the j^{th} radiation stream

The photons, after being single-scattered in the shell centred at a range r_i, are traced to compute the contributions of their successive scattering to the total received power.

The j^{th} (out of N_P) radiation stream interacts for the first time with the atmosphere at position $\boldsymbol{R}_1$ given by:

$$\boldsymbol{R}_1 = \boldsymbol{R}_{SC} + r_1 \hat{\boldsymbol{U}}_1 \tag{5.12}$$

where $\boldsymbol{R}_{SC}$ is the position vector of the spacecraft, $\hat{\boldsymbol{U}}_1$ coincides with the direction along which the photon stream has been transmitted, and

$$r_1 = r_i - \frac{ln\,(1 - q(1 - e^{-\tau_{layer}}))}{k_{ext,layer}} - \frac{\delta r}{2}$$

where the term $\tau_{layer} = \int_{r_1-\delta r/2}^{r_1+\delta r/2} k_{ext}(r)dr$ represents the optical depth of an atmospheric layer centred at r_i with thickness δr, $k_{ext,layer}$ is the extinction coefficient in the layer assumed to be constant inside the layer itself, and q is a random number between 0 and 1 drawn from a uniform distribution. The radiation stream interacts in the layer according to the optical depth of the layer itself.

As the photon stream is forced to single-scatter in the volume whose centre is at position $\boldsymbol{R}_i = r_i\hat{U}_1$, its contributions to the total received power must be weighted based on the probability of it reaching the layer and scattering in it (App. 5.A), which is

$$w^{j,\,1} = e^{-\tau_{\boldsymbol{R}_{SC},\,\boldsymbol{R}_i}}\,(1 - e^{-\tau_{layer}})\,\omega_1 \tag{5.13}$$

if single scattering occurs in the atmosphere, or

$$w^{j,\,1} = \mathcal{R}_1\, e^{-\tau_{\boldsymbol{R}_{SC},\,\boldsymbol{R}_i}} \tag{5.14}$$

if single-scattering occurs at the Earth surface. In the equations above, $\tau_{\boldsymbol{R}_{SC},\,\boldsymbol{R}_i}$ is the optical depth along the path covered by the photon stream to reach $\boldsymbol{R}_i$ from $\boldsymbol{R}_{SC}$, ω_1 is the single-scattering albedo of this atmospheric layer and $\mathcal{R}_1$ is the mean of the surface reflectance at the two orthogonal polarizations given by the Fresnel equation; they indicate the probability of the radiation stream to be scattered rather than absorbed.

In the following, the vector $\boldsymbol{R}_k$ denotes the position of the k^{th} collision point. The unit vector $\hat{\boldsymbol{U}}_k$ represents the photon's trajectory direction just before the k^{th} scattering event. Consequently, it defines both the scattering direction resulting from the $(k-1)^{\text{th}}$ collision and the incident direction for the k^{th} collision.
Then, the procedure follows, starting with $k = 2$:

1. The angles of scattering due to the $(k-1)^{\text{th}}$ scattering event are sampled according to App. 5.B. These angles define $\hat{\boldsymbol{U}}_k$.

2. The distance to collision along the direction $\hat{\boldsymbol{U}}_k$ is computed according to App. 5.D so that $\boldsymbol{R}_k = \boldsymbol{R}_{k-1} + d_{coll}\,\hat{\boldsymbol{U}}_k$ is the collision point of the k^{th} scattering event. If the radiation stream is upwelling, biasing techniques are used to make it interact with the atmosphere before it reaches the Top Of the Atmosphere (TOA).

3. As the photon stream interacts in $\hat{R}_k$, it can be absorbed or scattered, with the latter being forced via importance sampling. Since the fraction of radiation that is scattered is equal to the single scattering albedo, the weight associated to the radiation stream is updated according to App. 5.A:

   $$w^{j,\,k} = w^{j,\,k-1}\,\omega_k$$

   where ω_k is the single scattering albedo at point $\boldsymbol{R}_k$.

4. The contribution to the received power given by the k^{th} atmospheric scattering of the j^{th} radiation packet returning with direction $\hat{\Omega}^{j,\,k}$ at the receiver is computed with Eq. 5.2 which, since the estimation is performed using a Monte-Carlo, becomes:

$$\Delta P^{j,\,k}(r) = \frac{\lambda^2\, G_0}{4\pi}\, w^{j,\,k}\, F_t^j\, G_n(\hat{\Omega}^{j,\,k})\, p(\Theta)\, e^{-\tau_{\boldsymbol{R}_k,\boldsymbol{R}_{SC}}} \tag{5.15}$$

where

- $\hat{\Omega}^{j,\,k} = \dfrac{\boldsymbol{R}_{SC} - \boldsymbol{R}_k}{\|\boldsymbol{R}_{SC} - \boldsymbol{R}_k\|}$;
- $\Theta = arccos\dfrac{\hat{\boldsymbol{U}}_k \cdot (\boldsymbol{R}_{SC} - \boldsymbol{R}_k)}{\|\boldsymbol{R}_{SC} - \boldsymbol{R}_k\|}$ is the angle between the incident radiation beam direction and the direction to the receiver;
- $\tau_{\boldsymbol{k},\boldsymbol{SC}}$ is the optical depth along the path between $\boldsymbol{R}_k$ and $\boldsymbol{R}_{SC}$;
- r is the apparent range of the k^{th} order of the scattering and is computed as half of the path traveled by the photon, from its transmission by the antenna back to the receiver;
- p_Θ is the normalized phase function of the medium at point $\boldsymbol{R}_k$, described in Sect. 5.2.3.

Instead, if the k^{th} scattering occurs with the surface, the photons stream is scattered in a 2π solid angle centred in the direction normal to the surface. The weight of the photon is updated accordingly to the surface reflectance, similarly as it has done for the atmosphere with its albedo: $w^{j,\,k} = w^{j,\,k-1}\, \mathcal{R}_k$, where $\mathcal{R}_k$ is the mean of the reflectances of the surface for the two linear orthogonal polarization state of the reflected light. Eq. 5.15 becomes:

$$\Delta P^{j,\,k}_{surf}(r) = \frac{\lambda^2\, G_0}{4\pi}\, w^{j,\,k}\, F_t^j\, G_n(\hat{\Omega}^{j,\,k})\, BRDF(\hat{\Omega}^{j,\,k-1}, \hat{\Omega}^{j,\,k})\, e^{-\tau_{\boldsymbol{R}_k,\boldsymbol{R}_{SC}}} \tag{5.16}$$

where $BRDF(\hat{\Omega}^{j,\,k-1}, \hat{\Omega}^{j,\,k})$ is the Bidirectional Reflectance Distribution Function of the surface at point of scattering and is described in Sect. 5.2.3. The direction of scattering is sampled as described in App. 5.B.

5. The process is repeated from point 1, until the desired order of scattering is reached, or when $w < w_{min}$, where w_{min} is the minimum weight that is assumed to give a non-negligible contribution to the total received power.

Phase function of atmospheric targets

The phase function of a particle ensemble has been approximated with the Henyey-Greenstein equation thanks to the asymmetry parameter g:

$$p(\theta_s) = \frac{1 - g^2}{4\pi(1 + g^2 - 2g\cos\theta_s)^{1.5}} \tag{5.17}$$

The phase function is normalized to have its integral in the 4π solid angle equal to 1:

$$P_{int} = \int_0^{2\pi} d\phi_s \int_0^{\pi} p(\theta_s)\sin\theta_s d\theta = 2\pi \int_0^{\pi} p(\theta_s)\sin\theta_s d\theta_s = 1 \tag{5.18}$$

where θ_s is the elevation scattering angle and ϕ_s is the azimuthal scattering angle, both referring to the incident direction.

Bidirectional Reflectance Distribution Function

The BRDF defines how radiation is reflected off a surface.

The BRDF is a function of the directions of incoming and outgoing radiation ($\hat{\Omega}_i$ and $\hat{\Omega}_s$, respectively), and it represents the ratio between the reflected radiance exiting along $\hat{\Omega}_s$ to the irradiance incident on the surface from direction $\hat{\Omega}_i$.

Hereafter, land surfaces are assumed to be Lambertian. Hence, they reflect light with a cosine angular distribution, meaning that the measured reflected radiance is not dependent on the observing direction. Lambertian surfaces have thus an isotropic BRDF, which is equal to

$$BRDF(\hat{\Omega}_i, \hat{\Omega}_s) = 1/\pi \tag{5.19}$$

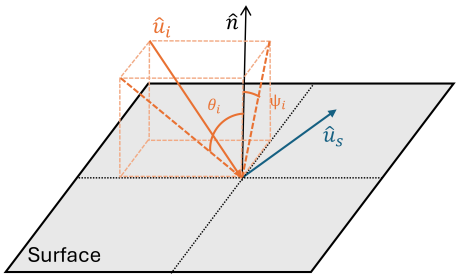

Fig. 5.2.2: *Schematics illustrating a surface collision's incidence angles. $\hat{\mathbf{u}}_i$ and $\hat{\mathbf{u}}_s$ are the incident (also defined by θ_i and ψ_i) and scattering directions, respectively. $\hat{\mathbf{n}}$ is the surface's normal unit vector.*

Sea surfaces are assumed to have a Gaussian distributed BRDF:

$$BRDF(\theta_i, \psi_i, \theta, \psi, \sigma_{BRDF}) = \frac{1}{2\pi\sigma^2_{BRDF}} \exp\left[-\frac{(\theta+\theta_i)^2 + (\psi+\psi_i)^2}{2\sigma^2_{BRDF}}\right] \tag{5.20}$$

where the angles θ_i and ψ_i define the incident direction (see Fig.5.2.2) and are calculated w.r.t. the surface normal, $\hat{\boldsymbol{n}}$. The direction of the main lobe of the BRDF can be derived as $\hat{\boldsymbol{u}}_0 - 2\hat{\boldsymbol{n}}(\hat{\boldsymbol{n}} \cdot \hat{\boldsymbol{u}}_0)$, with $\hat{\boldsymbol{u}}_0$ being the incident direction. σ_{BRDF} is the standard deviation of the distribution and is set arbitrarily to 0.1 rad, but further studies on how the surface scatters radiation have to be done to better characterize this value. Note that the maximum of the BRDF occurs at $[\theta = -\theta_i, \psi = -\psi_i]$, i.e. when the scattering direction coincides with the specular direction to the incident one. The BRDF is normalized such that, for a given incident direction, $\int_{2\pi} BRDF(\theta_i, \phi_i, \Omega)\, d\Omega = 1$, where the integral is performed across the solid angle Ω subtending the hemisphere that is orthogonal to the surface of reflection.

Total received power due to MS

The total contribution to the received power, received with apparent range r, due to multiple scattering , $P^{(\geq 2)}(r)$, is given by

$$P^{(\geq 2)}(r) = \sum_{j=1}^{N_T} \sum_{k=2}^{\infty} \Delta P^{j,\,k}(r) \tag{5.21}$$

The total radar reflectivity factor due to SS and MS contributions, $Z_{\delta r}^{MS}(r)$, at apparent range r, is thus given by:

$$Z_{\delta r}^{MS}(r) = \frac{P^{(\geq 2)}}{P_t} \frac{(4\pi)^3 \lambda^2}{G_0^2 \pi^5 |K^2|} \frac{r^2}{\delta r} \frac{1}{\Omega_{2A}} \tag{5.22}$$

5.3 RESULTS

Reflectivity profiles are simulated with radar and observation geometry configurations similar to those of INCUS (Haddad and Sy, 2024) for the Ka-band, and EarthCARE for the W-band (see Tab 5.3.1). Surfaces are assumed to be flat. For simplicity, the radar boresight is assumed to be pointed at nadir (i.e. $\hat{\boldsymbol{U}}_p = (0, 0, -1)$), also for INCUS, which instead employs a pushbroom 9 km swath observing geometry, with antennas pointing with different alon-track and cross-track elevation angles.

Table 5.3.1: *Parameters used for the simulation of multiply scattered Z-profiles.*

Satellite	**INCUS**	**EarthCARE**
Radar Output Frequency	**Ka-band (35.75 GHz)**	**W-band (94 GHz)**
Mean spherical altitude, H_{SC}	530 km	398 km
Orbit inclination, i	35°	97.05°
Scanning geometry	quasi-nadir pointing	nadir pointing
Antenna pattern	Gaussian	Gaussian
Antenna beamwidth, θ_{3dB}	0.35°	0.09°
Footprint size	3.2 km	0.76 km
Vertical resolution	240 m	500 m
Range sampling	60 m	100 m
Integration length	1 km	0.5 km
Sensitivity (after pulses integration)	12 dBZ	-36 dBZ
Point Target Response (PTR)	Hamming window with 0.2 taper	EarthCARE PTR

Hereafter, the measured radar reflectivity will be denoted with:

- Z_m^{SS} when simulated under the single-scattering assumption;
- Z_m^{MS} when simulated comprising multiple scattering effects, computed using the Monte Carlo approach that implements the 3D geometry of the scattering medium;
- $Z_m^{MS,\,TDTS} = Z_m^{SS} + \Delta Z_m^{MS,\,TDTS}$ when multiple scattering effects are computed using the TDTS approximation.

The Regional Atmospheric Modelling System (RAMS) ((Cotton et al., 2003)) provides simulations of vertical profiles of thermodynamic variables, hydrometeor mixing ratios and number concentrations for various types of storms. Those are used to compute the scattering properties in each of the voxels of the simulations, and they are employed to simulate Z-profiles. Simulations cover a wide range of convective storms:

1. Initial stages of a deep intense and isolated MCS over Argentina;
2. Terrain-forced deep and organized convection over the RELAMPAGO observatory, in Argentina;

3. Organized deep linear convection over Australia, associated with monsoon;

4. Deep, scattered convection over Congo, including congestus, deep, shallow, and isolated updrafts.

5.3.1 Case study: terrain-forced convection in Argentina

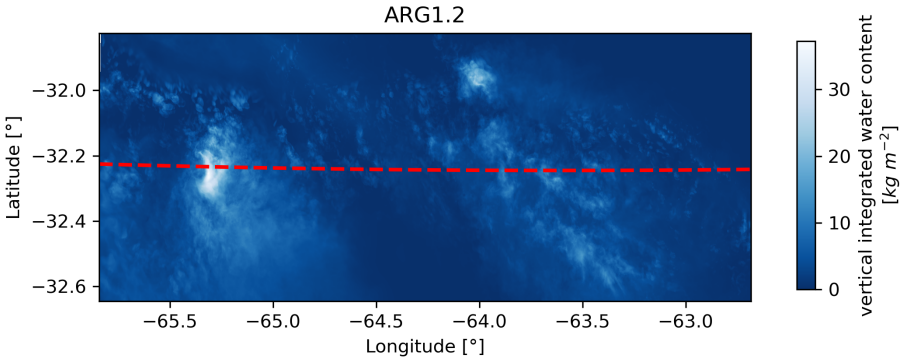

Fig. 5.3.1: *Vertically integrated water content of the Argentina systems. The satellite's groundtrack is represented by the red dashed line.*

One of the simulated cases is an overpass near two deep convective cells developing in Argentina (satellites grountrack is shown by the dashed red line in Fig. 5.3.1). The storm is very strong and is characterized by updrafts and downdrafts with vertical velocities greater than 20 m s^{-1}, which generates a large amount of hailstones and graupel particles.

A curtain plot of the reflectivity sampled in correspondence with the satellites groundtrack is shown in Fig. 5.3.2. In correspondence to the main two cores (at an along-track distance of $\sim$ 55 km and 160 km), the single-scattering reflectivity falls below the radar sensitivity already at 5 km below the cloud top for both the frequencies, and MS onset is located within less than 5 km below the cloud top. The MS tails may result in second trip echoes for both frequencies. For EarthCARE, the tails are still much greater ($\sim$ -15 dBZ) than the sensitivity at 15 km below the surface. The TDTS approximation underestimates and overestimates (Panels d), depending on the case, the radar reflectivity factor, especially in the tails and below the surface range where the TDTS technique does not account for surface MS contributions, but already at apparent ranges above the surface. This effect is more pronounced in EarthCARE than in INCUS where differences can exceed 5 dB at shorter than surface ranges.

Fig. 5.3.3 and Fig. 5.3.4 show the profile sampled by INCUS at $x = 162$ km and the profile sampled by EarthCARE at $x = 210$ km, respectively, both characterized by strong multiple-scattering effects. In the examples, the TDTS approximation gives overestimation of the reflectivity as shown in panel *a*.
Panel *c* shows the contribution of a given number of scatterings (x-axis) to Z, for any given apparent altitude (y-axis). Therefore, it also indicates the order of scattering needed to compute a certain fraction of Z. The solid, dashed and dotted lines denotes the order of scattering that generates the 0.95, 0.89 and 0.5 of the total received power, respectively, (corresponding to a negative bias of 0.22, 0.5 and 3 dB). Even above the

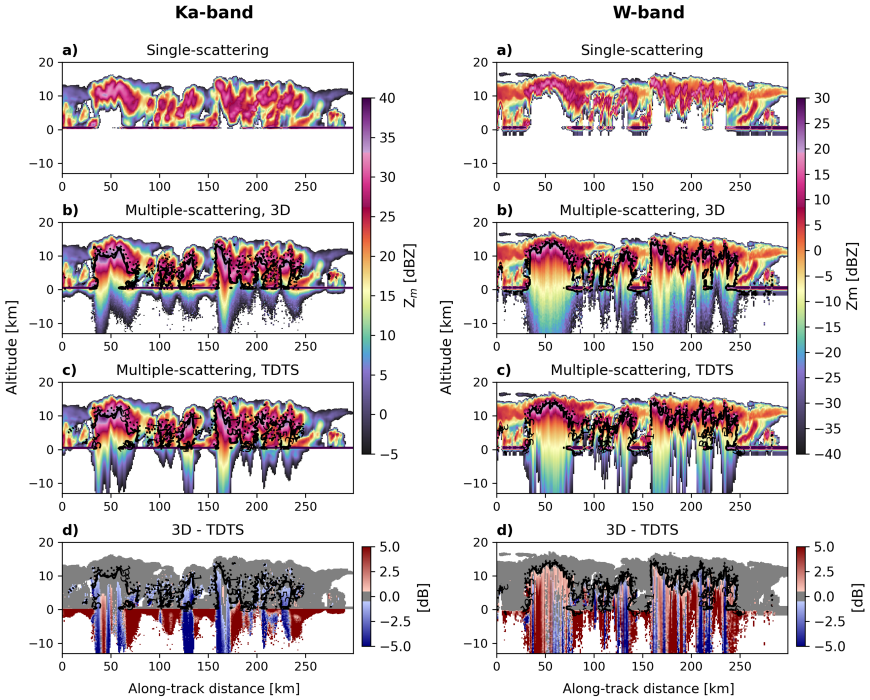

Fig. 5.3.2: *Curtain plot of simulated radar reflectivity as observed by INCUS (left column) and EarthCARE (right column) over the Argentina system. a, b and c panels show the single-scattering reflectivity, the reflectivity considering 3D multiple scattering effects, and reflectivity computed with the TDTS approximation, respectively. Dotted, dashed and solid black lines in panel b, c show the contour of the* 1 *dB,* 3 *dB and* 5 *dB MS enhancements, respectively. Panel d shows the difference between the 3D and TDTS radar reflectivity, with the grey colour indicating a bias between -0.5 and 0.5 dB.*

freezing level, around 20 and 30 orders of scattering are necessary to account for the 95% of the radar reflectivity.
Panel *b* shows how the scattering coefficient is distributed in the region within twice the radar beamwidth at different altitudes. For both cases, the center of the transmitted radiation beam corresponds to the center of the convective core, which is characterized by a scattering coefficient significantly higher than that of the surrounding region (note that the colorbar is in log-scale). When considering a 3-D atmosphere, this will produce a loss of radiation from the sides of the convective core. Instead, when the TDTS approximation is adopted, the surrounding medium is considered as optically thick as the convective core and more radiation is kept inside due to scattering. This leads to an overestimation of the radar reflectivity factor by the TDTS approximation.
Panel *d* shows, for any given apparent altitude (y-axis), how much a given altitude where scattering occurs (x-axis) contributes to the reflectivity. In these examples, most of the radiation is scattered within the upper ice layer and cannot reach the melting layer. This plot might be useful to optimize the importance sampling in Eq. 5.1 and how the photon streams are distributed along the range, i.e. optimizing the choice of f_i (Eq. 5.10). The histograms are normalized for each apparent altitude. The dotted, dashed and solid black lines indicate, for any given apparent altitude, the 0.5, 0.11 and 0.05 percentiles of the distribution, indicating that the 50, 89 and 95 %, of the radiation collected by the instruments originates above the indicated altitude.

The radar reflectivity computed by accounting for three-dimensional multiple-scattering effects ($Z_m^{MS,\,3D}$) can differ, in the tails, by several tens of dB from that obtained using the TDTS approximation ($Z_m^{MS,\,TDTS}$). To assess the relevance of 3-D effects, we use our dataset of simulated reflectivity profile to compare the bias between the the 3-D computation and the TDTS approximation ($Z_m^{MS,\,3D} - Z_m^{MS,\,TDTS}$) for different values of measured reflectivity, $Z_m^{MS,\,3D}$, by using the histograms in Fig. 5.3.5. Only points belonging to convective profiles, defined as profiles having at least one bin where the absolute value of the vertical velocity is $|w| > 2\,\mathrm{ms}^{-1}$, having a MS enhancement greater than 1 dB, and located above the surface form the histograms.

The INCUS configuration is not much affected by the TDTS approximation, with very few points exceeding an absolute error of 1 dB. Instead, the EarthCARE configuration is much more affected by such approximation, with many points exceeding the 2 dB absolute bias. Furthermore, in EarthCARE, the TDTS approximation tends to produce more underestimations than overestimations.

5.4 CONCLUSIONS

In this work a model capable of forward modelling multiple-scattering effects in a three-dimensional, inhomogeneous atmosphere, including multiple scattering involving surface interactions such as bistatic and mirror effects has been developed. The model can be exploited to assess the validity of 1D- approximation. For instance the TDTS approximation may either overestimate or underestimate multiple-scattering effects in reflectivity profiles, depending on the degree of inhomogeneity of the observed scene, as shown in simulations of convective profiles as observed by the INCUS and EarthCARE profiling radars.

Overall, three-dimensional multiple-scattering effects are small compared to the MS enhancement. In regions where the MS enhancement remains low the TDTS one-dimensional approximation generally provides a good representation for the reflectivities. However, in the multiple-scattering tails, three-dimensional effects can become

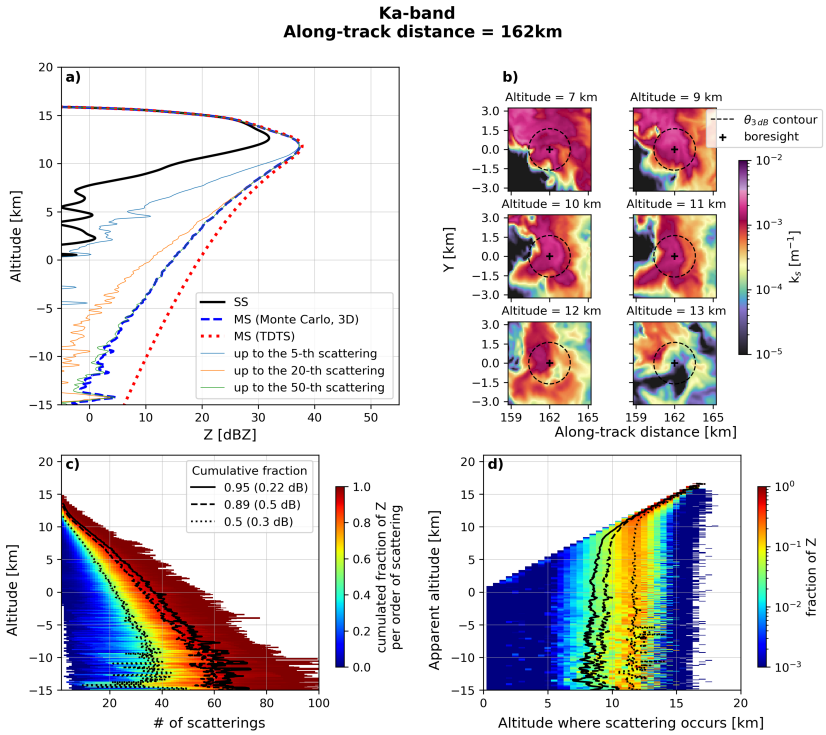

Fig. 5.3.3: *Panel a: example of an INCUS simulated Z-profile sampled in the Argentina system. Single-scattering (solid black line), 3D-multiple scattering (dashed blue line) and TDTS multiple scattering (dotted red line) reflectivities are shown in the plot. Reflectivities due to up the n-th order of scattering are shown in coloured thinner solid lines.*
Panel b: scattering coefficient horizontal field shown at six altitudes in correspondence to the profiles shown on the left. The dashed line represents the θ_{3dB} footprint of the radar.
Panel c: given an n-th order of scattering, the contribution given by the first to the n-th order of scattering is shown by the colorbar, for different altitudes. The solid, dashed and dotted contours indicate how many orders of scattering are needed to achieve 0.95 (0.22 dB), 0.89 (0.5 dB) and 0.5 (3 dB) of the total reflectivity, respectively.
Panel d: shows the fraction of Z given by radiation scattering at a given altitude, shown in x-axis, appearing at an apparent altitude shown in the y-axis. Solid and dashed lines represent the 0.95, 0.89 and 0.5 cumulative fraction from the cloud top. The fraction is normalized for each apparent altitude.

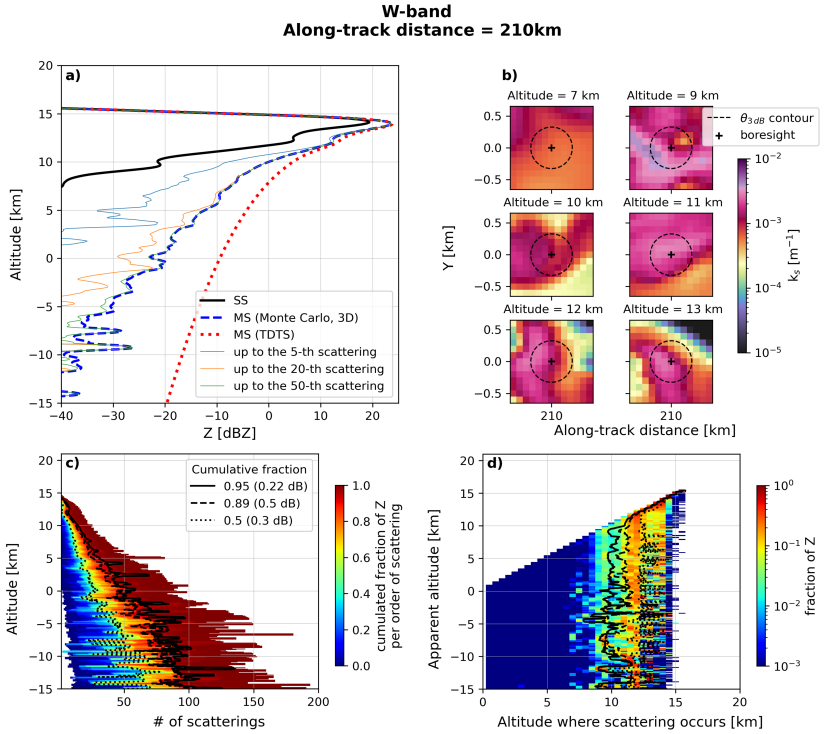

Fig. 5.3.4: *Same as Fig. 5.3.3 for an EarthCARE simulated Z-profile sampled in the Argentina system.*

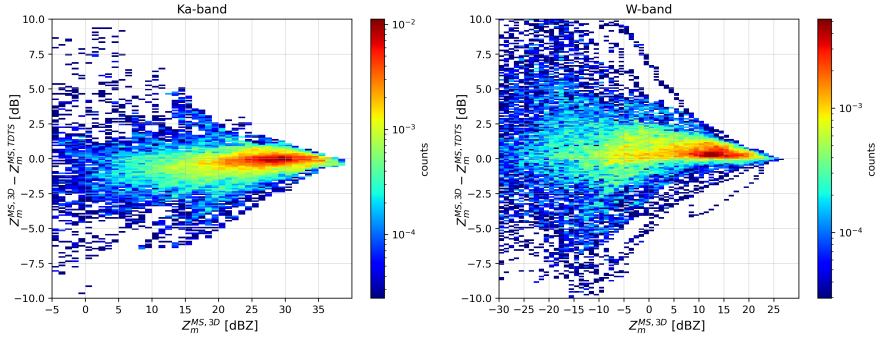

Fig. 5.3.5: *Histograms show the contribution to the measured reflectivity ($Z_m^{MS,3D}$, shown in the x-axis) of the 3-D effects ($Z_m^{MS,3D} - Z_m^{MS,TDTS}$, shown in the y-axis). Ka and W -band are shown on the left and right panels, respectively. Only points above the surface, belonging to convective profiles (defined as profiles having at least one bin with the absolute vertical velocity $|w| > 2\,ms^{-1}$), and with a MS enhancement ($Z_m^{MS,3D}$ - Z_m^{SS}) greater than 1 dB are included in the histogram.*

significant and the TDTS approximation can introduce both positive and negative biases up to several tens of dB.

5.A IMPORTANCE SAMPLING

Monte Carlo methods estimate the expected value of a function $E_p\left[f(\boldsymbol{X})\right] = \int p(\boldsymbol{x}) f(\boldsymbol{x}) d\boldsymbol{x}$ using samples from the probability distribution $p_{\boldsymbol{x}}$. This expectation is approximated as:

$$E_p\left[f(\boldsymbol{X})\right] \approx \frac{1}{N} \sum_{i=1}^{N} p(\boldsymbol{X}_i) f(\boldsymbol{X}_i) \tag{5.23}$$

However, in many cases, we want to sample from specific regions of our interest of the distribution, which are called important regions. To achieve this, we sample from a different distribution $q(\boldsymbol{x})$, which oversamples the important regions (Owen, 2019 (book)). Since this introduces bias, we correct the estimate by weighting each sample according to the ratio of the true and sampled probabilities. The corrected estimate becomes:

$$E_p\left[\frac{p(\boldsymbol{X})}{p_F(\boldsymbol{X})} f(\boldsymbol{X})\right] \approx \frac{1}{N} \sum_{i=1}^{N} \frac{p(\boldsymbol{x}_i)}{p_F(\boldsymbol{x}_i)} f(\boldsymbol{x}_i), \qquad \boldsymbol{x}_i \sim p_F(\boldsymbol{x}) \tag{5.24}$$

Therefore, we can sample $\boldsymbol{x}_i$ from distorted distribution, and correct for the bias by modifying the importance (i.e. weight) of the sample as:

$$w' = \frac{p(\boldsymbol{x})}{p_F(\boldsymbol{x})}\, w \tag{5.25}$$

where $p(\boldsymbol{x})$ is the true probability, $p_F(\boldsymbol{x})$ is the distorted probability.

In the following, q denotes a random number uniformly distributed between 0 and 1: $q \sim Uniform(0, 1)$. Each occurrence of q in the text, or in the formulas, represents a newly sampled random value.

5.B SAMPLING OF THE SCATTERING ANGLES

For atmospheric targets, the scattering angles, illustrated in Fig. 5.B.1, are sampled by a probability distribution defined by the phase function $p(\Theta)$.
The elevation scattering angle can also be derived analytically where, if $g = 0$ (isotropic scattering), θ_s is retrieved as $\theta_s = \arccos\left(2\, q - 1\right)$, otherwise:

$$\theta_s = \arccos \frac{1 + g^2 - \frac{1}{x}}{2\, g} \qquad \text{with } x \equiv \left(\frac{2\, g\, q}{1 - g^2} + \frac{1}{1 + g}\right)^2 \tag{5.26}$$

Being the phase function symmetrical in the azimuthal direction, the azimuthal scattering angle is retrieved as $\phi_s = 2\pi\, q$.

For Lambertian surface collisions, the scattering angles are sampled by an isotropic BRDF for all directions above the surface (i.e. $\phi_s = 2\pi\, q_1$ and $\theta_s = \arccos(\sqrt{q_2})$).
For sea surfaces, the BRDF is modelled as a Gaussian distribution with a standard deviation that depends on the roughness of the surface. As the standard deviation of the BRDF is set to be small (0.1 rad), the scattering direction is forced to be the specular to the incident one, i.e. at the peak of the BRDF.

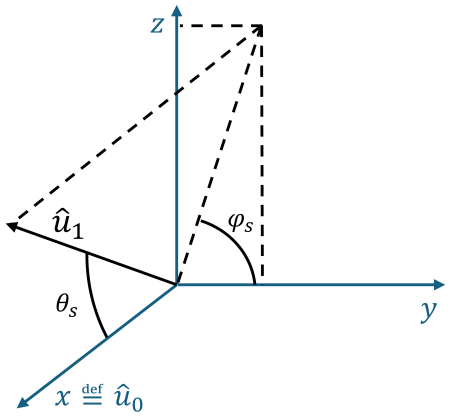

Fig. 5.B.1: *Schematics illustrating the scattering angles and directions in atmospheric collisions. $\hat{\mathbf{u}}_0$ and $\hat{\mathbf{u}}_1$ are the incident and scattering directions, respectively. For collisions with atmospheric targets, θ_s and ϕ_s are the elevation and azimuthal scattering angles, respectively.*

5.C SAMPLING OF THE DIRECTION OF TRANSMITTED RADIATION

The radiation is transmitted by the radar according to the antenna pattern. Therefore, the direction with which a photon stream is transmitted is sampled from a distribution $p_{emit}(\hat{\Omega}_t)$, which is set to correspond to the normalized antenna pattern $G_n(\hat{\Omega}_t)$. If $p_{emit}(\hat{\Omega}_t)$ is set to be different, the importance of the radiation stream must be updated, according to Eq. 5.25, to $w_t^j = \dfrac{G_n(\hat{\Omega}_t^j)}{p_{emit}(\hat{\Omega}_t^j)}$, where the numerator and denominator must be normalized to have the same area.

5.C.1 Transmission in case of Gaussian antenna

In case of a Gaussian antenna of the form:

$$G(\theta) = G_0 \exp\left[-8\log(2)\left(\frac{\theta}{\theta_{3\,dB}}\right)^2\right] \equiv G_0 G_n(\theta) \tag{5.27}$$

where θ is the antenna polar angle, the photons can be emitted at polar and azimuthal angles θ and ϕ generated with two random numbers q_1 and q_2:

$$\theta = \theta_{3\,dB}\sqrt{-\frac{\log(q_1)}{4\log(2)}} \tag{5.28}$$

$$\phi = 2\pi q_2. \tag{5.29}$$

this guarantees that the radiation is emitted with a polar angle probability density function of the form:

$$pdf(\theta) \propto \theta\ \exp\left[-8\log(2)\left(\frac{\theta}{\theta_{3\,dB}}\right)^2\right] \approx \sin\theta \exp\left[-8\log(2)\left(\frac{\theta}{\theta_{3\,dB}}\right)^2\right] \tag{5.30}$$

which is valid when θ is small.

5.D SAMPLING OF THE DISTANCE TO COLLISION

The distance to collision (d_{coll}), i.e., the distance a photon travels from one scattering event to the next collision point, depends on the optical thickness τ of the medium along the propagation direction. As the optical depth increases, the probability of the photon being absorbed or scattered also increases, leading to a shorter mean distance to collision. According to Beer-Lambert law, the optical depth follow an exponential PDF:

$$p(\tau) = e^{-\tau} \qquad \text{where } (0 \leq \tau \leq \infty) \tag{5.31}$$

$$P(\tau) = 1 - e^{-\tau} \tag{5.32}$$

where $P(\tau)$ is the CDF.

The optical depth of the path along the radiation propagation direction from one collision event to the next one is evaluated by the sampling of q:

$$\tau_{coll} = -ln(q) \tag{5.33}$$

The interaction occurs at the point where, along the photon's trajectory, $\tau = \tau_{coll}$. This stochastic sampling ensures that the length of the path of the photon reflects the probabilistic nature of interactions within the medium.

If the radiation is forced to interact within a given path, for instance, to avoid the photon reaching the boundary of the medium (e.g. at the top of the atmosphere), the PDF and CDF can be distorted as follow:

$$p_F(\tau) = \frac{e^{-\tau}}{1 - e^{-\tau_0}} \tag{5.34}$$

$$P_F(\tau) = \frac{1 - e^{-\tau}}{1 - e^{-\tau_0}} \tag{5.35}$$

where τ_0 is the optical depth along the path between the photon position and the medium boundary. Therefore:

$$\tau_{coll} = -ln\left[1 - q\left(1 - e^{-\tau_0}\right)\right] \tag{5.36}$$

and the photon's weight would be updated accordingly: $w' = \left(1 - e^{\tau_0}\right) w$.

5.E COORDINATE SYSTEMS

Right-handed cartesian coordinate systems employed for the simulation of the radar products are:

- **(x_{LVLH}, y_{LVLH}, z_{LVLH})** is the **local-vertical local-horizontal** reference frame centred in the centre of mass of the satellite. y_{LVLH} is parallel to the spacecraft's velocity, and z_{LVLH} is pointing towards the centre of Earth.
- **(x_b, y_b, z_b)** is the **body reference frame** of the antenna. z_b is parallel to the antenna pointing.
- (X, Y, Z) is a **topocentric reference frame** and the reference frame of the atmospheric model simulation. Z is aligned with zenith direction; X and Y are parallel to the Earth's surface ellipsoid.

- *lla*, or Latitude-Longitude-Altitude, reference frame: the first, second and third axes are aligned with the northward, eastward and zenith directions, respectively.
- (x, y, z) is a coordinate system centred in the collision point and here is named **scattering reference frame**; x is parallel to incident radiation beam direction.

Vectors $\boldsymbol{R}$ and unit vectors $\hat{\boldsymbol{U}}$ are expressed in a (*X,Y,Z*) coordinate system. Unit vectors $\hat{\boldsymbol{u}}$ are expressed in the (*x,y,z*) coordinate system.

- $\hat{\boldsymbol{U}}_0$ expressed in the (*x,y,z*) ref frame is thus: $\hat{\boldsymbol{u}}_0 = \{1, 0, 0\}$.
- $\hat{\boldsymbol{u}}_1 = \{\cos\theta_s, \quad \sin\theta_s \cos\phi_s, \quad \sin\theta_s \sin\phi_s\}$.

where θ_s and ϕ_s are the scattering angles (see Fig. 5.B.1).

5.E.1 Coordinate transformations

The Euler rotation matrices along the first, second and third axis are

$$L_1 = \begin{bmatrix} 1 & 0 & 0 \\ 0 & \cos\theta & -\sin\theta \\ 0 & \sin\theta & \cos\theta \end{bmatrix} \tag{5.37}$$

$$L_2 = \begin{bmatrix} \cos\theta & 0 & \sin\theta \\ 0 & 1 & 0 \\ -\sin\theta & 0 & \cos\theta \end{bmatrix} \tag{5.38}$$

$$L_3 = \begin{bmatrix} \cos\theta & -\sin\theta & 0 \\ \sin\theta & \cos\theta & 0 \\ 0 & 0 & 1 \end{bmatrix} \tag{5.39}$$

Transformation from the scattering to the atmospheric modeling simulation frame

Given $\hat{\boldsymbol{u}}$ expressed in the scattering frame, it can be represented in the (X, Y, Z) frame as

$$\hat{\boldsymbol{U}} = \left(L_2(\beta) L_3(\alpha)\right)^T \hat{\boldsymbol{u}} \tag{5.40}$$

where:

- $\hat{\boldsymbol{U}}$ is expressed in (X, Y, Z);
- α and β are the angles that define the orientation of the (x,y,z) axes in (X, Y, Z) (see Fig. 5.E.1), and are:

$$\begin{aligned} \beta &= \arcsin \hat{U}_0^z \\ \alpha &= \arccos\left(\frac{\hat{U}_0^x}{\cos\beta}\right) \end{aligned} \tag{5.41}$$

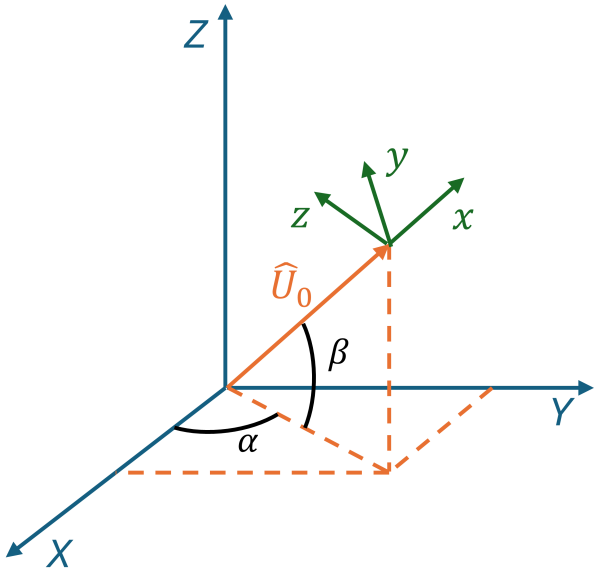

Fig. 5.E.1: *(X, Y, Z) and (x, y, z) coordinate systems. α and β represents the rotation angles that characterize the rotation between the two frames. $\hat{\mathbf{U}}_0$ is the direction of the incident radiation, expressed in the (X, Y, Z) reference frame; it is parallel to x.*

REFERENCES

Battaglia, A.: Impact of second-trip echoes for space-borne high-pulse-repetition-frequency nadir-looking W-band cloud radars, Atmospheric Measurement Techniques, 14, 7809–7820, https://doi.org/10.5194/amt-14-7809-2021, 2021.

Battaglia, A. and Mantovani, S.: Forward Monte Carlo computations of fully polarized microwave radiation in non-isotropic media, Journal of Quantitative Spectroscopy and Radiative Transfer, 95, 285–308, https://doi.org/https://doi.org/10.1016/j.jqsrt.2004.12.002, 2005.

Battaglia, A. and Simmer, C.: How Does Multiple Scattering Affect the Spaceborne W-Band Radar Measurements at Ranges Close to and Crossing the Sea-Surface Range?, IEEE Transactions on Geoscience and Remote Sensing, 46, 1644–1651, https://doi.org/10.1109/TGRS.2008.916085, 2008.

Battaglia, A. and Tanelli, S.: DOMUS: DOppler MUltiple-Scattering Simulator, IEEE Transactions on Geoscience and Remote Sensing, 49, 442–450, https://doi.org/10.1109/TGRS.2010.2052818, 2011.

Battaglia, A., Ajewole, M. O., and Simmer, C.: Evaluation of Radar Multiple-Scattering Effects from a GPM Perspective. Part I: Model Description and Validation, Journal of Applied Meteorology and Climatology, 45, 1634 – 1647, https://doi.org/10.1175/JAM2424.1, 2006.

Battaglia, A., Haynes, J. M., L'Ecuyer, T., and Simmer, C.: Identifying multiple-scattering-affected profiles in CloudSat observations over the oceans, Journal of

Geophysical Research: Atmospheres, 113, https://doi.org/https://doi.org/10.1029/2008JD009960, 2008a.

Battaglia, A., Kobayashi, S., Tanelli, S., Simmer, C., and Im, E.: Multiple Scattering Effects in Pulsed Radar Systems: An Intercomparison Study, Journal of Atmospheric and Oceanic Technology, 25, 1556 – 1567, https://doi.org/10.1175/2008JTECHA1023.1, 2008b.

Battaglia, A., Tanelli, S., Kobayashi, S., Zrnic, D., Hogan, R. J., and Simmer, C.: Multiple-scattering in radar systems: A review, Journal of Quantitative Spectroscopy and Radiative Transfer, 111, 917–947, https://doi.org/https://doi.org/10.1016/j.jqsrt.2009.11.024, 2010.

Battaglia, A., Tanelli, S., Mroz, K., and Tridon, F.: Multiple scattering in observations of the GPM dual-frequency precipitation radar: Evidence and impact on retrievals, Journal of Geophysical Research: Atmospheres, 120, 4090–4101, https://doi.org/https://doi.org/10.1002/2014JD022866, 2015.

Battaglia, A., Mroz, K., Lang, T., Tridon, F., Tanelli, S., Tian, L., and Heymsfield, G. M.: Using a multiwavelength suite of microwave instruments to investigate the microphysical structure of deep convective cores, J. Geophys. Res. Atm., 121, 9356–9381, https://doi.org/10.1002/2016JD025269, 2016a.

Battaglia, A., Mroz, K., Tanelli, S., Tridon, F., and Kirstetter, P.-E.: Multiple-Scattering-Induced "Ghost Echoes" in GPM DPR Observations of a Tornadic Supercell, Journal of Applied Meteorology and Climatology, 55, 1653 – 1666, https://doi.org/10.1175/JAMC-D-15-0136.1, 2016b.

Battaglia, A., Martire, P., Caubet, E., Phalippou, L., Stesina, F., Kollias, P., and Illingworth, A.: Observation error analysis for the WInd VElocity Radar Nephoscope W-band Doppler conically scanning spaceborne radar via end-to-end simulations, Atmospheric Measurement Techniques, 15, 3011–3030, https://doi.org/10.5194/amt-15-3011-2022, 2022.

Cotton, W. R., Pielke, R. A., Walko, R. L., Liston, G. E., Tremback, C. J., Jiang, H., McAnelly, R. L., Harrington, J. Y., Nicholls, M. E., Carrio, G. G., and McFadden, J. P.: RAMS 2001: Current status and future directions, Meteorology and Atmospheric Physics, 82, 5–29, https://doi.org/10.1007/s00703-001-0584-9, 2003.

Elvira, V. and Martino, L.: Advances in Importance Sampling, pp. 1–14, John Wiley & Sons, Ltd, https://doi.org/https://doi.org/10.1002/9781118445112.stat08284, 2021.

Fabry, F.: Radar meteorology: Principles and practice, Cambridge University Press, https://doi.org/10.1017/CBO9781107707405, 2015.

Galfione, A., Battaglia, A., Puigdomènech Treserras, B., and Kollias, P.: First insights into deep convection by the Doppler velocity measurements of the EarthCARE's Cloud Profiling Radar, EGUsphere, 2025, 1–25, https://doi.org/10.5194/egusphere-2025-1914, 2025.

Haddad, Z. S. and Sy, O. O.: From RainCube to INCUS: Using Miniaturized Microwave Instruments to Analyze the Dynamics of Tropical Convection, IEEE Journal of Microwaves, 4, 858–870, https://doi.org/10.1109/JMW.2024.3438126, 2024.

Haynes, J. M., Marchand, R. T., Luo, Z., Bodas-Salcedo, A., and Stephens, G. L.: A Multipurpose Radar Simulation Package: QuickBeam, Bulletin of the American Meteorological Society, 88, 1723 – 1728, https://doi.org/10.1175/BAMS-88-11-1723, 2007.

Hogan, R. J. and Battaglia, A.: Fast Lidar and Radar Multiple-Scattering Models. Part II: Wide-Angle Scattering Using the Time-Dependent Two-Stream Approximation, Journal of the Atmospheric Sciences, 65, 3636 – 3651, https://doi.org/10.1175/2008JAS2643.1, 2008.

Kollias, P., Battaglia, A., Tatarevic, A., Lamer, K., Tridon, F., and Pfitzenmaier, L.: The EarthCARE cloud profiling radar (CPR) doppler measurements in deep convection: challenges, post-processing, and science applications, in: Remote Sensing of the Atmosphere, Clouds, and Precipitation VII, edited by Im, E. and Yang, S., vol. 10776, p. 107760R, International Society for Optics and Photonics, SPIE, https://doi.org/10.1117/12.2324321, 2018.

Li, J. and Nakamura, K.: Characteristics of the Mirror Image of Precipitation Observed by the TRMM Precipitation Radar, Journal of Atmospheric and Oceanic Technology, 19, 145 – 158, https://doi.org/10.1175/1520-0426(2002)019<0145:COTMIO>2.0.CO;2, 2002.

Marzano, F. S., Roberti, L., Di Michele, S., Mugnai, A., and Tassa, A.: Modeling of apparent radar reflectivity due to convective clouds at attenuating wavelengths, Radio Science, 38, 2–1–2–16, https://doi.org/https://doi.org/10.1029/2002RS002613, 2003.

Matrosov, S. Y. and Battaglia, A.: Influence of multiple scattering on CloudSat measurements in snow: A model study, Geophysical Research Letters, 36, https://doi.org/https://doi.org/10.1029/2009GL038704, 2009.

Matrosov, S. Y., Battaglia, A., and Rodriguez, P.: Effects of Multiple Scattering on Attenuation-Based Retrievals of Stratiform Rainfall from CloudSat, Journal of Atmospheric and Oceanic Technology, 25, 2199 – 2208, https://doi.org/10.1175/2008JTECHA1095.1, 2008.

Meneghini, R. and Atlas, D.: Simultaneous Ocean Cross Section and Rainfall Measurements from Space with a Nadir-Looking Radar, Journal of Atmospheric and Oceanic Technology, 3, 400 – 413, https://doi.org/10.1175/1520-0426(1986)003<0400:SOCSAR>2.0.CO;2, 1986.

Moradi, I., Kalluri, S., and Zhu, Y.: Forward Modeling of Spaceborne Active Radar Observations, EGUsphere, 2025, 1–19, https://doi.org/10.5194/egusphere-2025-4372, 2025.

Tsang, L., Kong, J. A., and Shin, R. T.: Theory of microwave remote sensing, URL https://api.semanticscholar.org/CorpusID:129329319, 1985.

Wehr, T., Kubota, T., Tzeremes, G., Wallace, K., Nakatsuka, H., Ohno, Y., Koopman, R., Rusli, S., Kikuchi, M., Eisinger, M., Tanaka, T., Taga, M., Deghaye, P., Tomita, E., and Bernaerts, D.: The EarthCARE mission – science and system overview, Atmospheric Measurement Techniques, 16, 3581–3608, https://doi.org/10.5194/amt-16-3581-2023, 2023.

Chapter 6

Summary and conclusions

6 SUMMARY AND CONCLUSIONS

WIVERN and INCUS will be two of the next generations of space-borne radars that aims at filling some of the gaps in the GOS and provide insights on systems dynamics and structure. This thesis analyzed some of the critical aspects and challenges associated with space-borne radar measurements in the context of the WIVERN and INCUS missions.

Four methodologies have been proposed to characterize and correct the Doppler velocity error induced by mispointing in the conically scanning WIVERN radar. They effectively support the idea that the WIVERN requirements regarding the Doppler velocity are met with regard to mispointing uncertainty.

The sampling capabilities of the WIVERN conically scanning observation systems have been quantified for snowfall precipitations at the poles and compared to the capabilities of a CloudSat-like near nadir pointing radar. WIVERN snowfall measurements are characterized by an uncertainty below the climatological variability when they are averaged at the monthly scale and at $0.5^\circ \times 0.5^\circ$ latitude-longitude spatial scale. Instead, CloudSat measurements need to be averaged at annual scales zonally to produce the same uncertainties. When considering whole Antarctic and Greenland basins, both WIVERN and CloudSat provides reliable estimates at monthly scales, but the uncertainties in WIVERN's are significantly lower. However, CloudSat benefits from a thinner surface blind zone. Overall, the sampling strategy of WIVERN brings significant improvements in reducing the climatological uncertainty.

Regarding INCUS, the thesis is more focused on the forward modelling side, and a Monte Carlo based method to simulate MS effects that accounts for the three- dimensionality of the atmosphere has been proposed and described in Chapter 5. Simulations of reflectivity profiles in deep convective systems have been generated as observed by INCUS and by EarthCARE. A comparison between the TDTS approximation and the three dimensional MS contaminated profiles has been performed to assess whether the 1-D approximation can be considered valid even in highly heterogeneous environments such as convective systems. Results show that there is a bias, larger in EarthCARE than in INCUS, between the two, which becomes significant in the MS tails. Such bias becomes small when compared to the MS induced enhancement of the radar reflectivity and therefore the TDTS approximation can be applied with confidence in conditions when the multiple scattering enhancement is not overwhelming.

As future research, the forward model could be extended, as envisaged for WIVERN, to simulate both Doppler radar signals in presence of MS and brightness temperatures. For Doppler radars, this would involve the generation of Doppler spectra, following approaches such as in Battaglia and Tanelli (2011), but including full three-dimensional effects. The simulated spectra could then be used to produce synthetic $I\&Q$ signals, consistent with the methodology described in Schutgens (2008).

For passive radiometers, the model could be expanded to simulate brightness temperatures, instead of relying on the Eddington approximation, providing a more consistent framework for passive forward modeling.
Future studies could also focus on the design of de-aliasing algorithms for Doppler velocities that are important to correctly interpret high-speed motions and to prevent errors caused by velocity folding in the radar measurements. Also, it will be important to investigate how both active and passive forward modelling and observations are influenced by assumptions in microphysical properties, such as particle size distributions, density and shapes, as well as by different scattering models at Ka and W-bands. These investigations will help quantify the uncertainties introduced by model choices and provide insight into the robustness of the forward simulations and microphysical retrievals. Furthermore, understanding these sensitivities will be crucial for assessing how they propagate into retrievals and for ensuring the accuracy and reliability of measurement products for the WIVERN mission.

REFERENCES

Battaglia, A. and Tanelli, S.: DOMUS: DOppler MUltiple-Scattering Simulator, IEEE Transactions on Geoscience and Remote Sensing, 49, 442–450, https://doi.org/10.1109/TGRS.2010.2052818, 2011.

Schutgens, N. A. J.: Simulating Range Oversampled Doppler Radar Profiles of Inhomogeneous Targets, Journal of Atmospheric and Oceanic Technology, 25, 1514 – 1528, https://doi.org/10.1175/2007JTECHA1026.1, 2008.